FLUIDIZED BED DRYING OF PHARMACEUTICAL MATERIALS: BATCH AND CONTINUOUS MANUFACTURING

By

HAO CHEN

A dissertation submitted to the

School of Graduate Studies

Rutgers, The State University of New Jersey

In partial fulfillment of the requirements

For the degree of

Doctor of Philosophy

Graduate Program in Chemical and Biochemical Engineering

Written under the direction of

Benjamin J. Glasser

And approved by

_____

_____

_____

_____

New Brunswick, New Jersey

May 2019

ABSTRACT OF THE DISSERTATION

Fluidized Bed Drying of Pharmaceutical Materials: Batch and Continuous Manufacturing

By HAO CHEN

Dissertation Director:

Benjamin J. Glasser

Drying processes are common in the chemical, pharmaceutical and food industries. It is one of the traditional methods that removes moisture or solvents to provide stable products and/or semi-finished products. It is also known that the drying process is energy intensive. It has been reported that an average of 12 % of all energy consumed in the world is used for drying, and the cost of drying could reach up to 60 % - 70 % of total cost of investments. Therefore, the optimal operation of the drying process is sought to meet the requirements for cost-effective manufacturing.

In the pharmaceutical industry, the particulate ingredients are often granulated to improve their flowability and uniformity. A fluidized bed gas-solid drying is usually followed to remove the moisture that is introduced during the granulation. Before a new formulation is launched into commercial size units, it is prevalent to do lab-scale tests to understand its characteristics. Although a number of studies have been done on fluidized bed scale-up, practical scale-up rules for fluidized bed drying still remain unclear. This work will start with understanding several important operational parameters for fluidized beds. Then, a

practical scaling rule will be introduced to predict the drying behavior of a pharmaceutical excipient in large scale units based on lab-scale results.

Another part of the work will be to try and use the knowledge gained from the batch mode fluidized bed dryers to predict the behavior of a continuous mode fluidized bed dryer. Several pharmaceutical manufacturers are moving towards continuous manufacturing due to its potential to improve agility, flexibility, and robustness.The fluidized bed unit operation can be easily implemented as a continuous process for drying. One of the most important tools to characterize a continuous unit is the residence time distribution (RTD). It describes the probability distribution of the material staying in the unit. The RTD will be investigated in this work via a tracer study. With the RTD model for flow in the continuous fluidized bed and drying kinetic models constructed with data from lab-scale experiments, we will develop an approach to predict the final moisture content of the product. The final moisture content variations caused by changes in the operating condition or changes in the feed material will also be evaluated.

Acknowledgment

This dissertation is accomplished by years of endeavors at Rutgers University. I would not have been able to finish this work without the guidance, support, patience, and love from my advisors, colleagues, friends, and families. I would like to thank my advisor Benjamin Glasser for his guidance. Dr. Glasser has given me advice on all aspects of my professional development – how to think critically and solve problems creatively as an engineer, how to guide my own students as a mentor, and how to collaborate with colleagues and give a public speech as a team leader. I wish to express my gratitude to Dr. Glasser for his patient guidance, for his thorough review of my manuscripts and for his encouragement and support when I face challenges.

I would like to thank Dr. Fernando Muzzio for his insight and mentorship to help me understand the broader picture of my research. I acknowledge Prof. Timothy Langrish from The University of Sydney for his fruitful collaboration and professional insights. I would like to thank my dissertation proposal committee members: Dr. Rohit Ramachandran, Dr. Nina Shapley, Dr. Gerardo Callegari for giving advice to my thesis. I acknowledge my colleagues: Dr. Veerakiet Boonkanogwong for being a really great fellow and sharing a great friendship with me, Anusha Noorithaya for her help with the SEM imaging and always being a loyal friend, Cody Bishop for providing me with views as a chemist and support. I acknowledge my outstanding students Subham Rustagi and Emily Diep. They have always been supportive of my research. Their diligence and excellent academic performance have also been an encouragement to push me moving forward. I acknowledge Clara Hartmanshenn for bringing positive energy to the office and inspiring me when the research was stuck.

I acknowledge all the colleagues in Prof. Glasser's research group: Dr. Yangyang Shen, Dr. Bereket Yohannes, Dr. Plamen Grigorov, Prateek Sarkar and Chaitanya Bangalore for offering their advice and help. I acknowledge the (previous) colleagues from the Engineering Research Center, Dr. Sarang Oka, Dr. James Scicolone, Dr. Andrés Román, Dr. Savitha Panikar, Dr. Yifan Wang, Dr. Wei Meng, Thamer Omar, Tianyi Li, Zhanjie Zhou, Jingzhe Li and Qiushi Zhou for their collaboration and advice in this work.

And finally, I express my deepest gratitude to my beloved wife, Wenqi. I will not be able to make it without her support and love.

Table of contents

List of tables

List of illustrations

Chapter 1 Introduction

1.1 Background

Drying is one of the traditional methods used to remove moisture or solvents from slurries or solids [1-3]. The reason for drying is as diverse as the materials which may be dried [4]. A product needs to be dried to a particular moisture content for subsequent processing or sale. For some materials, a pre-drying process at a lower temperature is adopted to reduce the overall operating cost. Furthermore, the transportation cost usually depends on the moisture content of the material, and therefore, the material needs to be dried to a certain moisture content to minimize the cost of transportation and drying.

When a material dries, heat is transferred to the liquid phase for evaporation, and mass is transferred in the form of vapor [5]. Several heat transfer mechanisms include 1) convection from a hot and dry gas (usually air) that is brought in contact with the wet material; 2) conduction from a hot surface that contacts the material; 3) radiation from a heat source that is closed to the wet material; and a less common method 4) dielectric heating that utilizes the molecule vibration to generate the heat internally within the wet materials.

There have been a variety of drying methods in industry application which usually involves more than one of the heating mechanisms discussed above. Small quantities of material are dried in batches while continuous dryers are used when large quantities of material are handled. Sloan [6] has identified more than 20 types of dryers and classified them based on the heat exchange method, operation type (batch or continuous) and whether the heat conduction is direct or indirect. McCormick [7] reviewed 19 types of dryers according to

how well they handle different materials. Keey [4, 8] pointed out three principal factors to classify the dryers: 1) the method which the heat is supplied to the material, 2) operating temperature and the pressure and 3) the way the material is handled within the dryer. Mujumdar [9] classified the dryers based on the previous three factors and discussed the selection of dryers under different circumstances.

In the food industry, drying is used to remove excess water to ensure the stability of the product [10, 11]. Products such as coffee, tobacco, tea, fruit, cocoa beans, rice, and nuts usually require a consistent application of low heat and therefore can use solar dryers [12]. Similarly, in the timber industry, a solar kiln is used for drying the newly cut timbers that need to be dried to a certain moisture content for further processing. The drying process must be controlled carefully to minimize the degradation of the material due to its nonlinearity drying behavior [13-16]. In the dairy industry, milk powder is produced by spray drying to minimize the thermal damage of the product because of the low temperature and short residence time [17]. In the ceramic industry, ceramic tiles are usually manufactured by the 'wet method' with a single firing [18]. Clays, silica, fluxes, pigments and other raw materials are mixed and granulated into solid granules with low water content to be ready for the forming stage. The granules are pressed into thin tiles and then dried in a continuous dryer for subsequent glazing, decorating and final firing. Another route for preparing ceramic tiles is to dry the slurry of raw material suspension in a spray dryer [19].

In the pharmaceutical industry, the selection of a suitable dryer and of a drying model depends mainly on the properties of materials and the production scale [20]. For large molecule products, freeze-drying followed by spray drying is a preferred method to

dehydrate the large molecule (proteins, vaccines) products [21]. Supercritical fluid drying is a potential alternative method for removing water from proteins [22-25]. For small molecules products, two major stages can be distinguished during the manufacturing process– primary and secondary[26]. In the primary stage, active pharmaceutical ingredients (APIs) are manufactured. In the secondary stage, APIs and other inert fillings (excipients) are mixed to form tablets or capsules. Filter dryers and contact dryers are used for recovering intermediates and APIs after the crystallization process [20, 27]. Spray dryers are used for forming desired sizes of APIs and excipients. Fluidized bed dryers are used for drying the wet materials from the wet granulation process. In this dissertation, the drying of pharmaceutical solids will be studied in fluidized bed dryers.

1.2 Moisture in Pharmaceutical Solids

The moisture usually exists in drug products in forms of crystallization/adsorbed water or free water. Moisture may come from the bulk drug or inactive excipients in the formulation. It can be introduced during the manufacturing processes such as granulation and tablet coating or by the absorption of water from the atmosphere at high air humidity due to capillary condensation and deliquescence induced by the hydroscopic property of the high porosity ingredient. The manufacturers control the level of moisture content in the drug products to prevent problems regarding product stability, tablet compaction, microbial control, and solids flow property.

A pharmaceutical dosage form generally consists of an API and several non-active excipients. Moisture in the drug product will reduce product stability, causing the final product degradation. Many factors related to moisture could induce the unexpected phase transformation of APIs [28]. The water presented in the excipients or introduced in

processing may concentrate in amorphous regions of the drug and cause degradation such as hydrolysis reaction [29].

Moisture level is also a crucial factor in tablet compaction as it increases the compact strength by increasing the tensile strength of the power bed. Absorbed water can increase the particle surface energy thus preventing the adhesion of tablets to the die wall. On the other hand, blends with extremely low moisture content could cause a capping tablet defect. Therefore, controlling the moisture content at an appropriate range becomes critical. Pande and Shangraw examined the role of moisture in the compatibility of β-cyclodextrin. They found that the samples lost compactibility at low moisture content. The samples yield maximum compactibility at about 14% moisture content [30].

Moisture level can affect the solids flow property which is critical to continuous manufacturing. In general, increasing the moisture content in the powder blend will reduce its flowability. The strength of the liquid bridges formed between particles is higher when it has a thicker absorbed liquid layer [31]. At higher moisture content, the particle size may be enlarged due to the agglomeration which can also improve the flowability. Erica et al. investigated the effect of moisture content on the flowability of two pharmaceutical ingredients – Aspartame and Hydroxypropyl Methylcellulose (HPMC). A non-linear decrease in flowability of HPMC and a non-linear increase in flowability of Aspartame were found with increasing moisture content [32] .

Measurement of the average moisture content in the samples usually consists of direct methods and indirect methods. The direct methods determine the sample moisture content by drying in an oven with or without blow through of air. The drying process can be considered as complete when the difference between the two consecutive measurements

does not exceed ±0.05% [9]. The moisture content of the sample is calculated by the weight difference before and after drying. Such a method is also called “loss on drying” (LOD). Measuring the loss on drying is typically a fast process for measuring the approximate moisture content of a powder sample. However, the LOD will only be able to report the amount of the volatile substance (the majority being water) in the sample. The molecularly bound water or water of crystallization are not referred by LOD.

For some of the heat-sensitive or porous materials, where the drying temperature needs to be controlled at a low level, and the drying takes a long time, the indirect methods are usually used in industry. Karl Fischer (KF) titration is a chemical analysis that determines the moisture content of a sample. The KF provides an accurate measurement of water in the sample whether its in solid, liquid or gas form. As a result, it is one of the primary ways of moisture content measurement in the chemical, food and pharmaceutical industry. However, the KF method is destructive and is slow for in-process measurement. The near-infrared (NIR) technology allows the investigator to measure the moisture content in-line during the process. NIR moisture measurement uses reflectance and absorbance principles for calculating the moisture content. NIR can detect various drug hydration states and is most suitable for tracing moisture as it shows strong absorption bands in the NIR region[33]. Generally, the NIR absorption spectrum of liquid water at room temperature shows bands at 760, 970,1190,1450 and 1940nm with free water usually shows a band at 1905 nm and bound water shows a band at around 1936nm [34]. Another method of determining the average moisture content and study the drying kinetics is to measure the moisture in the gas. This is usually carried out by measuring the relative humidity of the

inlet and exhaust air. The moisture content can be calculated by the mass balance in the gas phase.

1.3 Fluidized Bed Dryer

Fluidized beds have been widely used in the chemical, pharmaceutical and food industries as batch dryers due to their high heat and mass transfer rates as a result of the high contact between gas and particles in the chamber [35-38]. Successful applications of fluidized bed dryers include drying food products such as soybeans, agricultural products such as paddy and colza, biochemical products such as baker's yeast and pharmaceutical materials such as dibasic calcium phosphate powder [39-43]. The reason for the extensive use of fluidized bed dryers is due to several features: 1) they provide a fairly uniform bed temperature in the chamber for homogenous drying and easy control of temperature and operation [44] and 2) they can be operated at a relatively low temperature with a high drying rate which makes them favorable for heat sensitive materials [35]. In the pharmaceutical industry, fluidized bed drying plays an important role in producing the high porosity of pharmaceutical granules which promotes drug delivery [45-50].

The fluidization of the powders in a fluidized bed can be described according to the model from Kunni and Levenspiel. As the flow of gas passes through a particulate solid bed, the solids remain static on a gas distributor plate when the air flow is low (see Figure 1-1a). The pressure drop across the bed increases as the air velocity raises (see Figure 1-2) .As we keep increasing the air flow, at a certain point, the drag force applied to the particles is equivalent to the weight, the bed will be barely lifted (see Figure 1-1 b) The corresponding air velocity is called the "minimum fluidization velocity." For materials with high initial moisture content, the minimum fluidization velocity will be higher. The minimum

fluidization velocity can be estimated by balancing the gravitational force and the drag force from the Ergun equation.

$$W_s = \Delta P A_c$$

Eq. 1-1

where, W_s is the weight of the solid bed, ΔP is the pressure drop across the bed and A_c is the cross-sectional area.

The weight of the solids in the bed:

$$W_s = g(1-\varepsilon)(\rho_p - \rho_g)hA_c$$

Eq. 1-2

ε is the porosity of the bed at the minimum fluidization condition. ρ_p and ρ_g are the density of the solid particles and the air, respectively. h is the height of the static bed.

The pressure drop from the Ergun equation:

$$\frac{\Delta P}{h} = \rho_g U^2 \left[\frac{150(1-\varepsilon)}{Re\psi} + 1.75\right]\frac{(1-\varepsilon)}{\psi d_p \varepsilon^3}$$

Eq. 1-3

U is the air velocity. Re is the Reynolds number. Ψ is the shape factor of the particles. d_p is the diameter of the particles.

The minimum fluidization velocity is, therefore,

$$u_{mf} = \frac{(\psi d_p)^2}{150\mu}\left[g(\rho_p - \rho_g)\right]\frac{\varepsilon_{mf}^3}{1-\varepsilon_{mf}}$$

Eq. 1-4

With a further increase in the air flow, the air suspends the particles in the air stream, resulting in a dynamic fluid-like state for the particles [34] (see Figure 1-1c). An expanded bed is obtained with some particles brought up into the air stream. As the upward drag force keeps increasing, eventually the weight of particles is counterbalanced, the separation of the particles increases, and the bed is fluidized. The pressure drop will be constant during this period (Figure 1-2).

Depending on the particle sizes and density, the fluidization state might be different. According to Geldart, the particles can be classified into four categories [51]. Group A particles have a small mean size and/or a low density in general. Group A particles flow smoothly when the air flow exceeds the minimum fluidization velocity. The circulation of the powder occurs even when few bubbles exist, and thus results in rapid mixing during fluidization. Group B particles have a mean particle size that typically falls in the range of 40 μm – 500 μm, and a density of 1.4 g/cm^3 - 4.0 g/cm^3. The group B powders are sand-like particles. There's little circulation in the absence of air bubbles. Group C particles are fine, cohesive powders. Fluidization of group C powders is extremely difficult because the interparticle forces are so strong that the air cannot disperse the particle clumps. Therefore, the heat and mass transfer between the gas phase and solid phase is much poorer than group A and B powders. Fluidization of group C powders can be made possible by adding agitation or vibration to the system and using a higher air flow rate. Coating the particles is also a solution to fluidize group C particles[52]. Group D particles are large and dense particles. Group D particles usually result in large bubbles and a relatively more mixing state.

As the air flow keeps increasing, a slug flow (Figure 1-1d) will occur as the bubble size exceeds the diameter of the fluidized bed. At extremely high air velocity, the materials might be blown out of the fluidized bed causing "entrainment" (Figure 1-1 e). The pressure drop of the bed will be therefore decreasing due to the loss of the materials (Figure 1-2).

1.4 Fluidized Bed Dryer Modeling

1.4.1 Drying Process

In a fluidized bed dryer system, the material being treated is a bulk of particles. As the fluidized bed has extremely well mixing, the drying process in a fluidized bed can, somehow, be considered as a scale-up of a single particle drying process or a thin layer drying process. For a single porous solid particle surrounded by a flow of atmospheric air, a schematic figure of the drying is shown in Figure 1-3. The drying process can be divided into three different drying periods: the preheating period, the unhindered drying period (some literature referred as "constant-rate period") and the hindered drying period (some literature referred as "falling rate period") [53-56]. At the start of drying, the particles are covered with excess liquid. As dry heating air flows through the particle, the liquid on the droplet surface is heated, and evaporation starts. In this preheating period, the drying rate keeps increasing until the wet-bulb temperature of the drying air is reached within a short period of time. During the unhindered drying period, the system reaches a steady state. The drying rate is independent of the drying time which can be described with zero order kinetics. As soon as the exterior moisture has been evaporated and the moisture content decreases to a critical value, the drying front penetrates the particle surface, and the drying rate drops significantly. The cause of the hindered drying period is that convection no longer dominates the drying process. Instead, capillary forces are introduced as the outside

surface turns into dry porous crust and water is drawn through the pores from the wet core. It has been reported that for particle diameters greater than 2 mm, a linear curve could be used to describe the hindered drying period [57].

Many drying models have been proposed to simulate the drying kinetics. As it is difficult to monitor the properties (moisture content, temperature) of a single particle during the drying process in practice, an average of the powder bed properties is often used for describing the drying kinetics. These models have been developed based on different assumptions.

1.4.2 Heat Transfer

The heat transfer in a fluidized bed dryer can occur by conduction, convection and radiation. Heat transfer between a particle and gas phase can be described as:

$$q = h_p A_p (T_p - T_g)$$

Eq. 1-5

where q is the rate of heat transfer,

h_p is the heat transfer coefficient,

A_p is the particle surface area,

T_p is the particle temperature,

and T_g is the gas temperature.

The heat transfer coefficient can be estimated from the equation below [58]:

$$h_p = \frac{k_g}{d_p} Nu_p$$

Eq. 1-6

where, k_g is the air thermal conductivity,

d_p is the particle diameter,

Nu_p is the particle Nusselt number.

For $0.1<Re_p<50$, $Nu_p = 0.0282Re_p^{1.4}Pr_g^{0.33}$.

For $50<Re_p<10^4$, $Nu_p = 1.01Re_p^{0.48}Pr_g^{0.33}$.

Re_p is the particle Reynolds number, and Pr_g is the gas Prandtl number.

1.4.3 Diffusion Model

Zahed and Epstein [59] developed a diffusion model for spout bed drying and Martinez-Vera et al. [60] verified the model for a fluidized bed dryer. The model made the following assumptions:

1. The diffusive mass transfer controls the process.
2. The particles are spherical, isotropic and of uniform size.
3. The temperature gradients inside the particle are negligible.
4. The fluidized bed system is a perfectly mixed system.
5. The diffusivity is constant.

The moisture content during the drying process is then,

$$\frac{\partial X}{\partial t} = D\left[\left(\frac{\partial^2 X}{\partial r^2}\right) + \frac{2}{r}\left(\frac{\partial X}{\partial r}\right)\right]$$

Eq. 1-7

where X is the moisture content,

D is the diffusivity,

and r is the radial dimension.

The average moisture content $\bar{X}$ is

$$\bar{X} = \frac{4\pi}{V_p}\int_0^{r_p} r^2 X dr$$

Eq. 1-8

where, V_p is the particle volume.

Another diffusion model that is often used was developed based on Fick's second law of diffusion [61]:

$$\frac{\partial X}{\partial t} = D_{eff}\nabla^2 X$$

Eq. 1-9

where, D_{eff} is the effective diffusivity.

The mathematical solution of the above equation in the spherical coordinate is given by[61, 62]

$$MR = \frac{X - X_{eq}}{X_0 - X_{eq}} = \frac{6}{\pi^2}\sum_{n=1}^{\infty}\frac{1}{n^2} exp\left[-n^2\frac{\pi^2 D_{eff} t}{4L^2}\right]$$

Eq. 1-10

where MR stands for moisture ratio. X_0 and X_{eq} are the initial moisture content and the equilibrium moisture content. L is the half thickness of the sample. n is a positive integer. t is time. At a sufficiently long drying time, the above equation can be simplified to:

$$MR = \frac{6}{\pi^2} exp\left(-\frac{\pi^2 D_{eff} t}{4L^2}\right)$$

Eq. 1-11

Taghavivand et al. [62] validated the model for pharmaceutical granules and the model prediction showed a good agreement with the experimental data.

1.4.4 Empirical Model

The moisture ratio during the drying often follows a linear or an exponential decaying trend. For simplicity, empirical models are often used for describing the drying process. Table 1-1 summarizes some common models for isothermal drying.

1.4.5 Mechanic Model

Mortier et al. [63] reviewed some sophisticated drying models for fluidized bed that are developed to understand the drying behavior of pharmaceutical granule at a different level of scale. Three different types of models, each with its own objectives, have been developed for modeling of fluidized bed drying: porous material models, population balance models, and computational fluid dynamics models. The porous material models, as a starting point, investigate the dynamics of the drying process at a pore level. The continuum approach, pore network modeling, and single particle modeling are the three most often used approaches in this area. Dong-Hyun Lee et al. [64] developed a mathematical model for batch drying in fluidized bed dryers using a continuum approach. A three-phase model was used with a bubble phase, an interstitial gas phase, and a solid

phase. A surface-stripping model was used to describe the decrease in particle size with drying time due to attrition and entrainment. Modified overall heat and mass transfer coefficients between the particles and the external gas film were proposed. The model successfully predicted the mass and heat transfer in a conventional fluidized bed dryer using an inert medium. Population balance modeling provides the particle distribution for different properties of interest, such as particle size, moisture content, and temperature. Limited work has been done in terms of the drying kinetics of batch drying processes. However, similar work for granulation and spray-drying processes has been performed [65-69]. Computational fluid dynamics (CFD) models provide detailed information about the spatial behavior of the system but require a large amount of computational power. The two most popular methods for performing CFD modeling are the Eulerian-Lagrangian, and the Eulerian-Eulerian approaches, where the former can calculate the behavior of every single particle but requires significant computational effort and the latter considers the gas phase and solid phase as continuous and fully interpenetrating.

1.5 Energy Efficiency of Fluidized Bed Dryers

Several challenges of commercializing fluidized bed drying include its high energy cost, low energy efficiency, the complexity of scale-up and difficulty determining the process end-point. It has been reported that an average of 12 % of all energy consumed is used on drying, and the cost of drying could reach up to 60 % - 70 % of total cost of investments [42, 70]. Emrah Özahi et al. [71] established a model of a batch fluidized bed dryer in terms of mass, energy and exergy balances. They found that lower initial moisture content and higher ambient temperature led to the lower energy efficiency of drying, whereas increasing the material loading could increase the efficiency. The flow rate of the heating

air and the initial loading of the material were found to have more of an effect on drying than other operating parameters. Sazzat et al. [42] presented an energy and exergy analysis of paddy drying using an industrial fluidized bed dryer. They stated that higher initial moisture content led to an increase in energy usage and energy usage ratio (EUR). Syahrul et al. [72] conducted experiments with wheat and corn and then compared the data with predictions from a model developed from thermodynamics. The results showed that the effect of the heating air flow rate and heating air temperature on drying varied with different particle properties. Hematian et al. [39] studied the kinetics of drying sodium percarbonate particles in a conical fluidized bed. They compared 15 widely used empirical models of drying. For most operating conditions, the modified Hendersen and Pabis model had good agreement with experimental data points.

Zielinska et al. [3] studied the drying behavior of carrot cubes in a fluidized bed dryer. It was discovered that a higher air velocity of heating air was required when the moisture content of the carrot particles was higher. As the drying process proceeded, a lower value of air velocity was required to maintain the same height of the bed. The drying rate was influenced by the applied heating temperature. With a higher temperature, the mass and heat transfer were more intense producing a higher drying rate. Zhao et al. [73] investigated the effect of drying temperature, air velocity, vibration, particles size and bed height on the drying of Chinese lignite in a vibration fluidized bed. A drying curve was fitted using the Midilli-Kucuk model [74] which is an empirical model that is suitable for a single layer drying process. They found that the drying rate increased when higher temperature and higher superficial air velocity were applied. Reducing the size of particles and bed height increased the effective contact area, therefore enhancing the drying. Liu et al. [75] reported

that the effect of particle size on drying is not significant for dibasic calcium phosphate anhydrous (DCPA).

An important parameter in the design of fluidized beds is the air pattern, defined by the geometry of the dryer and the inlet air introduction manner, which determines the fluidization of the materials and the corresponding drying performance [76]. Michael et al. [77] studied the hydrodynamic behavior inside different types of fluidized vessels. They stated that the bubbling frequency decreased with time in conical beds whereas cylindrical beds experienced an increase due to different particle circulation patterns. These results indicated that some undesirable fluidization phenomena such as defluidization or segregation could be caused by the improper choice of vessel geometry which may lead to the failure of whole batches. Eliaers et al. [78] compared the performance of a rotating fluidized bed in a static geometry (RFB-SG) to a conventional fluidized bed. The RFB-SG introduced air tangentially by using a vortex chamber. Upon contact with granules, the direction of the inlet air shifts vertically upwards. By using such a design, the wet granules were able to form denser and more uniform beds. It was found that RFB-SG was able to dry the biomass at a much higher feed rate but maintained the same energy efficiency as compared to a conventional fluidized bed.

1.6 Scaling of Fluidized Bed Dryers

Another major problem for fluidized beds is the difficulty in scaling. Although the pharmaceutical industry has been adopting continuous manufacturing which, to some extent, can avoid scale-up problems through parallel manufacturing lines [79], a majority of pharmaceutical manufacturers still use batch processing or are in a slow transition to continuous process due to the strong regulatory dependent nature of the pharmaceutical

industry. Furthermore, the transfer from lab-scale to commercial-scale is usually carried out in a batch process and still requires scaling. A successful scale-up of a new process requires careful consideration of equipment selection, sizing and operating condition [80]. For a fluidized bed dryer, the scale-up process requires not only the knowledge of the fluidized state of the solids but also an understanding of the drying process.

As a fluidized bed is a sophisticated system containing heterogeneous phases (gas, solid and liquid), the particle flow patterns and the particle drying inside the fluidized bed are subject to many uncertainties that can significantly affect the performance and economics of the fluidized bed. Rüdisüli et al. [12] discussed several challenges in the scale-up of bubbling fluidized bed reactors. Some of the parameters that were important in small scales may not be critical in larger scales. Masten [13] reported that the bed density and thus expansion is scale-independent. However, that conflicted with De Groot's [81] findings which showed that the bed expansion was a function of the bed diameter. Rüdisüli pointed out that such a contradiction was due to the effect of the wall, which was more significant in small scales. In general, scale-up cannot be described merely by a few mathematical equations as Matsen [82] has discussed: "Scale-up is still not an exact science, but is rather that mix of physics, mathematics, witchcraft, history and common sense that we call engineering."

Fluidized bed scale-up has scale related properties such as mass/heat transfer, solid circulation, gas flow, and bubble growth, as well as scale independent properties such as material properties. A scaling model can help to understand the critical parameters determining the hydrodynamics of the solids and the drying or reaction rate in different sized fluidized beds. One of the most widely used scaling models to describe the

hydrodynamics is the Glicksman scaling laws where a series of non-dimensional parameters are defined based on the equations of motion and conservation of the gas and solid phases [83, 84]. The dimensionless parameters are the Reynolds number, the Froude number, the ratio of the density of the gas and solids, the aspect ratio of the reactor, the ratio of the particle size to the fluidized bed reactor size, the particle sphericity and the particle size distribution. Ommen et al. [85] validated the Glicksman scaling rules using computational fluid dynamics (CFD) simulations. A set of simplified scaling parameters was compared to the full set of scaling parameters because it is difficult to match all the parameters in practice. The pressure and bed voidage were compared after the bed height and width were doubled, and good agreement was observed [86].

The Glicksman scaling rules focused on hydrodynamics and did not provide information about the reaction/drying occurring in the fluidized bed. Rambali et al. [87] scaled up the batch fluidized granulation process by matching the powder bed moisture content at the end of spraying as well as the droplet size with the granule size. A regression model was proposed for the granule sizes produced in different sized fluidized beds. The model was able to successfully predict the granule size in pilot scale experiments from lab scale experiments.

In the pharmaceutical industry, the scale-up of the drying unit operation is required to take place without changes to the critical quality attributes (CQAs) of a drug product (DP) [88]. The chemical and physical stability of the API may change when the drug product is exposed to heat and agitation for a long period of time. Therefore, being able to predict the drying time under different operating conditions that affect the drying kinetics becomes critical to pharmaceutical manufacturing. Keech et al. studied the drying kinetics of purolit

and silica gel particles using the thin-layer method described by Langrish et al. [89-91]. The proposed method related the drying kinetics of a fluidized bed dryer to a single particle. The results showed that the characteristic drying rate is independent of external drying conditions. When modeling the drying kinetics, many drying parameters such as the heat transfer coefficient and diffusion coefficient are difficult to predict from theoretical considerations and require experimental measurement because the moisture transport is highly correlated to the internal structure of the material. Reay and Allen [92] developed a model for the thermal design of a fluidized bed dryer that predicts isothermal bed drying curves from measurements made at constant inlet gas temperature. Based on Reay and Allen's model, Bahu [93] developed a more complete formulation for predicting the batch drying curve and successfully applied the model to the scale-up of continuous fluidized bed dryer on a wide variety of materials. The model was then modified by Kemp and Oakley [94] to obtain a scale-up equation:

$$Z = \frac{\Delta\tau_2}{\Delta\tau_1} = \frac{\left(\frac{m_B}{A}\right)_2 G_1 (T_{GI} - T_{wb})_1}{\left(\frac{m_B}{A}\right)_1 G_2 (T_{GI} - T_{wb})_2}$$

Eq. 1-12

The normalization scaling factor, Z, is the ratio of $\Delta\tau$ for two fluidized beds where $\Delta\tau$ is the time required to remove a fixed amount of moisture from the materials and allows the prediction of the drying time under different operating conditions – loading, air flow and air temperature. The rate of drying is related to several parameters such as, $\frac{m_B}{A}$, the bed weight (m_B) per unit area (A), G the gas mass velocity and $T_{GI} - T_{wb}$ the temperature difference between the inlet gas (T_{GI}) and the bed (T_{wb}). Each of these parameters are

directly related to the heat and mass transfer that occurs within the fluidized bed. For example, the difference in the inlet gas temperature and the bed temperature encompasses the driving force for evaporation in the system.

As the Kemp and Oakley [94] model showed its potential advantages in predicting the drying curves without needing to determine the heat and mass transfer coefficient, we are interested in testing the model under a variety of operating conditions in two different size fluidized bed systems for a porous pharmaceutical powder. In this dissertation, an in-depth investigation of this model will be presented to validate this model experimentally and to provide information for industrial applications.

1.7 Continuous Manufacturing in Pharmaceutical Industry

Traditional pharmaceutical oral dosage manufacturing is carried out in a series of batch unit operations which is usually inefficient and expensive. In recent years, the pharmaceutical industry has been in the transition from the traditional batch process to continuous process due to the improved agility, flexibility, and robustness. In continuous manufacturing, the drug product is being produced in a continuous manner, and the amount of product can, ideally, be determined by the production time. Therefore, continuous manufacturing can be scaled into commercial size by either scaling up the equipment size or increasing production time, which results in a significant reduction in cost compared to the batch processes [95]. Using continuous manufacturing saves a tremendous amount of expensive APIs for the design of experiments (DOE) during development to support a quality-by-design (QbD) filing which fits the US food and drug administration (FDA) requirement of a shorter time frame for drug development [96]. Continuous manufacturing also reduces the production time because less time is spent as downtime as compared to

the traditional batch processes, which allows extended patent lifetime [97]. Furthermore, the number of materials in stock can be reduced via supply chain management.

Tablets are the most commonly used solid dosage forms in the pharmaceutical industry [98]. Direct compaction is often considered the easiest and the most cost-efficient way of carrying out continuous manufacturing for oral solid dosage [99]. However, it remains a challenge when dealing with high drug dosage with poor compressibility. The literature has reported a number of drug products with high-dose and/or poor compressability[100] – paracetamol [101], ibuprofen [102], mefenamic acid [103], acetazolamide [104], metformin [105], and hydroxyapatite [106]. At low dosage, the direct compaction process also suffers from the drug uniformity issues due to the poor flowing and the cohesive drug substance in the powder blend [107, 108]. Such issues can be resolved by the wet granulation process.

The wet granulation process brings into contact the APIs and other excipients to form granules [109]. As a result, the flowability and the uniformity of the powder blend are improved [110]. Vervaet et al. [111] reviewed a list of different types of granulator used in the pharmaceutical industry. A typical layout of the continuous wet granulation process is shown in Figure 1-4. Fonteyne et al. [112] studied the ConsiGma 25 twin-screw granulator in a continuous process line. Several process analytical technology (PAT) tools – NIR, Raman spectroscopy, and on-line particle sized analyses – were used to identify the critical process parameters that influence the granule properties. The barrel temperature, the amount of liquid addition, and to a lesser extent, the powder feed rate affected the granules solid state. Meng et al. [113] compared the critical process parameters and the granulation mechanism of a high shear wet granulator and a twin screw granulator. A DOE was set up

based on three process variables – rotation speed of the shaft/screw, liquid to solid ratio, and throughput of the material. The high shear granulator showed high dependence on process variables and produced smaller size variance compared to the twin-screw granulator.

While the granulation process has been widely studied these years, there is limited literature focused on the subsequent drying process. By reducing the moisture level, several problems of wet granules related to the solids flowability, tablet compaction, microbial control, and product stability are resolved [29]. Fluidized bed drying is one of the most popularly used unit operations for drying pharmaceutical wet granulations due to its several advantages. The high heat and mass transfer rate between the gas and solid phases provide a mild heating profile which prevents potential degradation of the heat-sensitive APIs. The excellent mixing ensures the uniform property of the processing materials.

Although batch-wise fluidized bed process has been well studied, continuous fluidized bed drying remains to be a somewhat new process to the pharmaceutical industry. Process understanding is a critical prerequisite for continuous manufacturing. A deep understanding of the process enables one to design, analyze and control manufacturing through measurements of several critical quality attributes from the process, which is consistent with the current drug quality system requirement “quality cannot be tested into products; it should be built-in or should be by design” [114]. Pramod et al. listed various critical quality attributes (CQA) for drug substances, excipients and drug products [115]. As the purpose of the fluidized bed drying process is to reduce the moisture level while keeping product uniformity, the particle size distribution and the moisture level are of most interest [26]. The effect of critical process parameters (CPP) on the CQAs of the fluidized

bed was well-studied. Leersnyer et al. [116] studied the breakage and attrition phenomena during fluidized bed drying after continuous twin screw granulator. It was discovered that the breakage of the granules occurred during the first seconds of drying. The drying time did not affect the breakage and attrition after the critical moisture content was reached. In addition, the air temperature and air flow did not influence the granule size distribution. Chen et al. [117] carried out a parametric study of initial moisture, loading, airflow, and air temperature on the effect of drying time in different scales of fluidized bed dryers. It was found that each operating parameter had a significant impact on drying independently. Furthermore, the drying process was more efficient when carried out at a lower temperature and higher airflow. The primary thermal design of a batch fluidized bed dryer can be described by an incremental model. Kemp et al. [94] summarized a drying kinetic model developed by Reay and Allen [92] and extended by Reay [118], McKenzie and Bahu [93, 119]. The model predicted the drying rate as a function of the solids moisture content and the dryer operating conditions (loading, airflow, and air temperature).

To ensure the product quality is within the desired space over time, a continuous manufacturing process needs to operate under a state of control. The process parameters and quality attributes are designed to be kept within a specific range. However, during the start-up, shut-down, and transition between states, the process parameters and quality attributes will be changed inevitably. The disturbances triggered by the deviations of the process parameters could affect the final product quality, leading to a product failure. For a continuous process, since the regulatory definition of a batch has no restriction regarding the manufacturing method, it is possible to rescue a failure process and reject only part of the product by adequately defining a “batch” via a thorough understanding of the process

dynamics of how material flows through the process. Engisch et al. [120] studied the traceability of a continuous direct compaction system. They obtained the residence time distribution (RTD) and the cumulative distribution function F(t) of the direct compaction process from tracer experiments. The batch boundaries were defined as F(t) equals to 0.5% and 99.5%, respectively. A pulse-like addition of a component was introduced to simulate the hazard affecting the content uniformity. With the help of RTD, the disturbance was quantified, allowing for a downstream control.

1.8 Overview of the Thesis

The thesis aims to implement the fluidized bed drying technology into the continuous pharmaceutical manufacturing of drug products by 1) understanding the drying process in fluidized bed dryers, 2) establishing a model that is able to scale up the lab fluidized bed process and 3) studying and characterizing a continuous fluidized bed dryer based on the knowledge from batch fluidized bed drying. Chapter 2 will focus on a parametric investigation of batch fluidized beds. Chapter 3 will introduce a scaling model developed based on a mass and energy balance. The impact of the drying process and design parameters will be elucidated. Chapter 4 will discuss the hydrodynamics and the drying process of solid particles in a continuous fluidized bed. Chapter 5 will summarize the overall conclusion from the above chapters.

1.9 Figures for Chapter 1

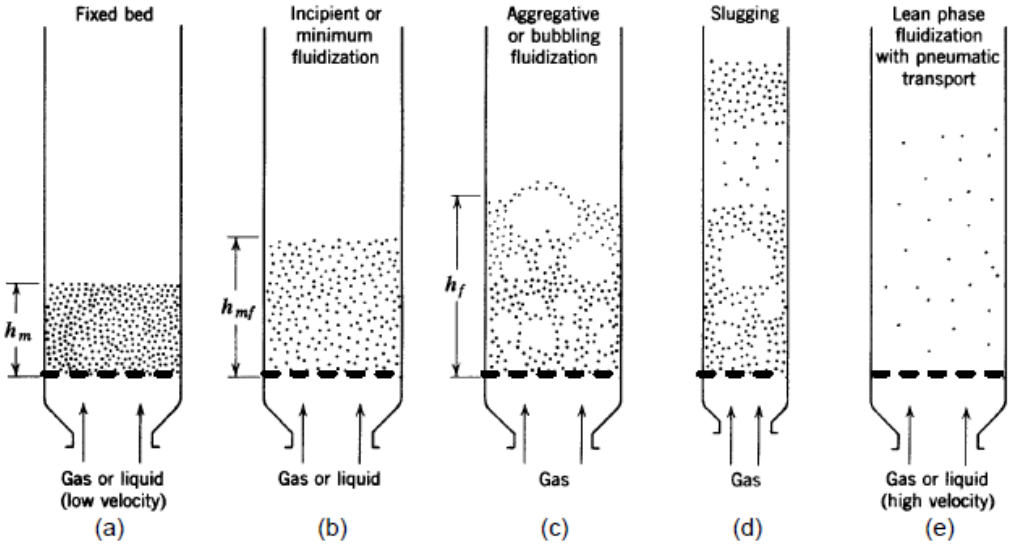

Figure R12.3-2 Various kinds of contacting of a batch of solids by fluid. Adapted from Kunii & Levenspiel, *Fluidized Engineering* (Huntington, NY: Robert E. Krieger Publishing Co., 1977).

Figure 1-1:Various kinds of fluidization status of a batch fluidized bed. Figure source: Kunii and Levenspiel.

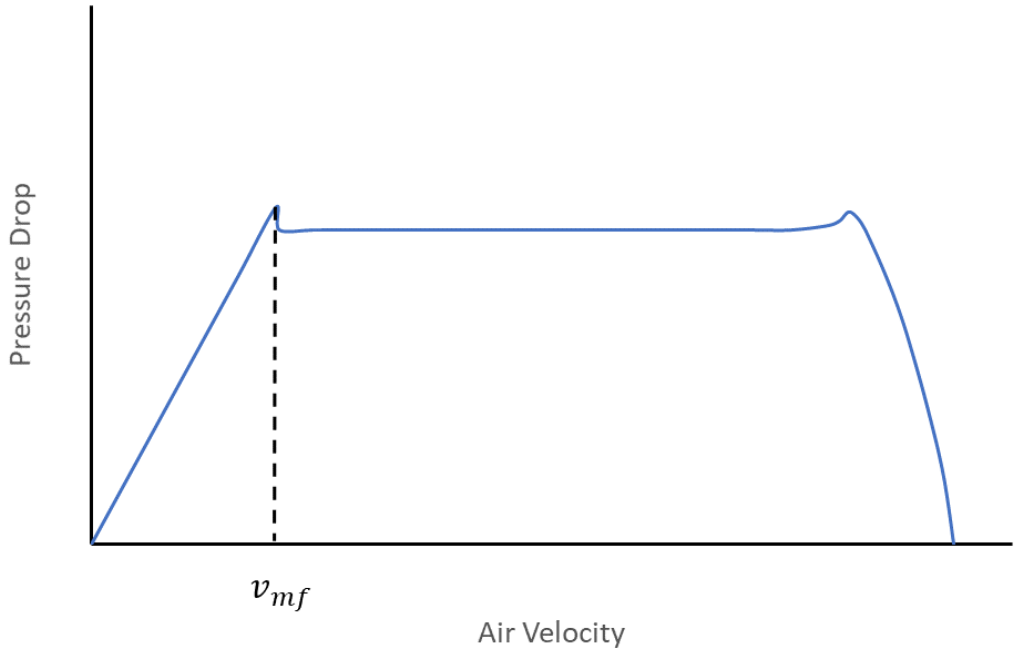

Figure 1-2: Pressure drop vs. air velocity in a fluidized bed

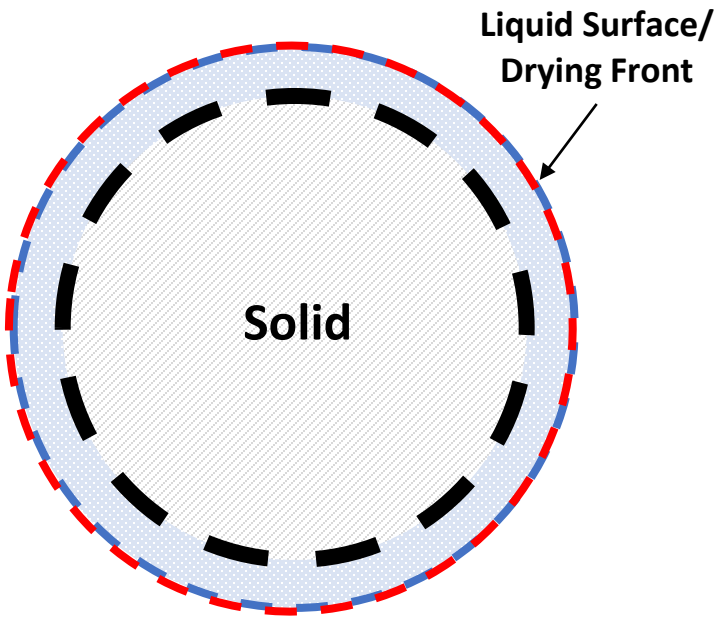

Figure 1-3: Scheme of single particle drying

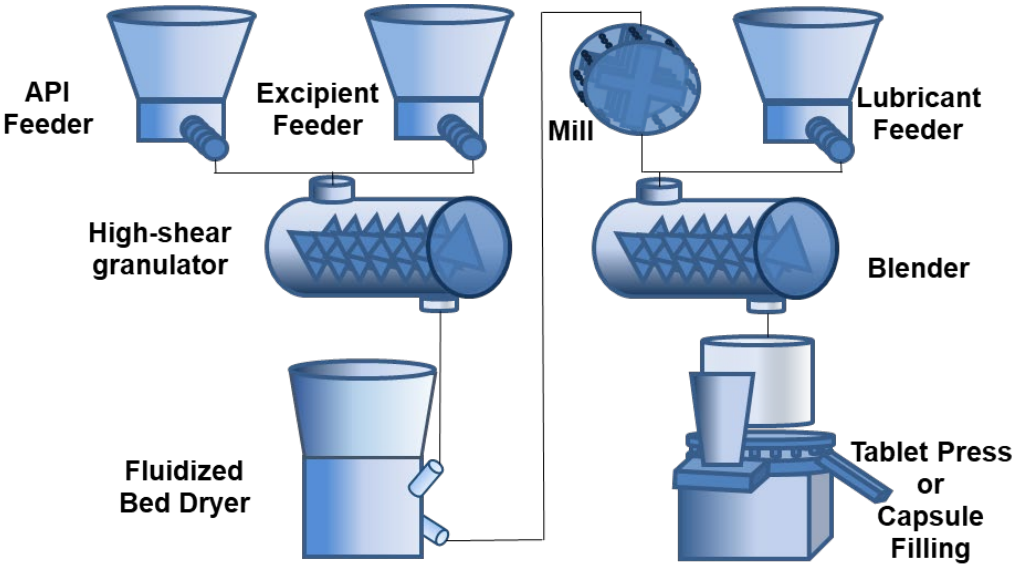

Figure 1-4: A typical layout of continuous granulation process.

1.10 Tables for Chapter 1

Table 1-1:Empirical models for drying

Model name	Model equation	Parameters
Newton [121-123]	$MR = \exp(-kt)$	k
Page [124, 125]	$MR = \exp(-kt^n)$	k, n
Midilli-Kucuk [74]	$MR = a\exp(-kt^n) + bt$	a, b, k, n
Two-term [126]	$MR = a\exp(-k_0 t) + b\exp(-k_1 t)$	a, b, k_0, k_1
Two-term exponential[127]	$MR = a\exp(-kt) + (1-a)\exp(-kat)$	a, k
Verma[128]	$MR = a\exp(-kt) + (1-a)\exp(-gt)$	a, k, g

Chapter 2 Parametric Study of Batch Fluidized Bed Drying

Drying consumes a significant amount of energy and requires a relatively long time in the pharmaceutical industry. Fluidized bed drying is widely used for drying granules due to its mild and uniform drying. In this section, the effect of several important operation parameters – (1) the initial moisture content, (2) the inlet heating air temperature, (3) the inlet heating air mass flow rate, and (4) the material loading for batch fluidized bed drying process will be discussed. The drying curve will be compared for different conditions. An energy efficiency analysis will be carried out to determine the energy-friendly operating condition.

2.1 Introduction

There has been a limited amount of work examining the kinetics of drying of particles in fluidized beds, and many questions remain unanswered. In Chapter 2, the drying of a pharmaceutical excipient in batch fluidized beds will be investigated. Firstly, an investigation of operating conditions on fluidized bed drying will be carried out. Four parameters have been considered vital for the drying performance: 1) the initial moisture content, 2) the inlet heating air temperature, 3) the inlet heating air mass flow rate and 4) the material loading in the dryer; these four parameters will be considered in this work. Two batch type fluidized bed dryers with different geometry and size will be studied. The effect of operating parameters on drying will be analyzed using normal plots and Pareto charts. Secondly, the drying kinetics of the particles in a lab scale batch fluidized bed will be investigated with various drying models. The fluidized bed results will be compared to a traditional oven drying. The effect of the particle size will be discussed. Eventually, the effect of the aforementioned operating conditions on the drying efficiency will be

studied.This work serves to characterize the performance of these two fluidized bed dryer systems and to provide physical insight into the fundamentals of drying of porous materials.

2.2 Experiment setup

2.2.1 Materials and Methods

Dibasic calcium phosphate anhydrous (DCPA) particles were purchased from Fuji Chemical Industries (USA). DCPA is a common excipient in pharmaceutical manufacturing. The average surface area of the DCPA material is 40 m^2/g (data provided by Fuji Chemical Industries). The pore volume of the DCPA material was analyzed by the N_2 adsorption and desorption method (TriStar 3000, Micrometrics, USA). The pore volume of the DCPA material was found to be 0.19 cm^3/g. The mean size of the particles is 120 μm. Figure 2-1 shows SEM micrographs for the DCPA particles, which have a fairly spherical shape.

2.2.2 Fluidized Bed Apparatus

Two commercial lab-scale batch-type fluidized bed dryers, Glatt GPCG-1 and MiniGlatt 5 (Glatt Air Techniques Inc., Ramsey, NJ, USA), were used to investigate the effect of operating conditions on the drying kinetics. The geometries of the two fluidized bed dryers are shown in Figure 2-2. The conical drying chambers of the two dryers are made of stainless steel. The chamber of the GPCG-1 (a) is 58 cm in height, and the diameter of the top and the bottom are 15 cm and 30 cm, respectively. The cone entrance angle is 15°. For the MiniGlatt (see Figure 2-2b), the chamber is 11 cm in height, and the diameter of the top and the bottom are 14 cm and 6.6 cm respectively with a cone entrance angle of 37°. The chamber volume is 23 L for the GPCG-1 and 3 L for the MiniGlatt. Compared to the MiniGlatt dryer, the GPCG-1 dryer has a smaller relative change in radius along its vertical

axis. This leads to relatively uniform air flow, whereas the drastic change of air flow at the bottom of the MiniGlatt dryer results in a spout-like circulation pattern of powders. The product temperature was measured using a thermocouple placed 2.5 cm above the distributors and was immersed in the bed. A two-phase nozzle was placed in the middle of the chamber which was used to spray atomized water into the dry powders. Figure 2-3 shows the full-cone nozzle spraying the mist. We estimate the size of the water droplets to be about 50 microns while the DCPA particles have a mean size of 120 microns. The average DCPA particle volume was approximately 14 times larger than the water droplet volume. A sample thief at the wall of the chambers allows sampling in order to measure the moisture content during the drying process. A thermocouple that allows the monitoring of inlet air temperature was attached below the distributor. Hot air was pretreated to remove moisture through an air desiccant dryer (manufactured by Van Air Inc., Lake City, PA, USA), and then supplied from the bottom. Filters with fine holes were placed above the chambers to prevent the loss of particles. In order to prevent filter blockage, the Glatt system has an automatic shaking function that was applied to the frame of the filter. A window at the side wall of the chamber enables one to monitor the situation inside by visual observation. Figure 2-2c and Figure 2-2d show the actual experimental setup of the GPCG-1 and the MiniGlatt, respectively.

The oven drying study was carried out by using a moisture analyzer MB45 (Ohaus, Corporation, Parsippany, NJ, USA), which is shown in Figure 2-4. The original purpose of a moisture analyzer is for measuring the loss on drying (LOD) of a material. In this study, the LOD vs. time was exported to investigate the drying behavior in a moisture analyzer which could also be considered as an oven. The main part of the MB45 consists of a

weighing part and a heating part. During the measurement, the heating part is above the weighing part (i.e., above the samples). An opening window on top of the cover and a gap between the cover and the weighing part allow the drying air flow through passively. The weighing part measures the weight of the samples every second and calculates the weight loss. The moisture analyzer is set up in such a way that the measurement is considered as finished when the weight loss is less than 1mg in 30 seconds.

2.2.3 Operating Conditions

Prior to drying, a pre-determined amount of DCPA material was weighed and pretreated in an oven at 80 °C for 2 days. The DCPA was then placed in the fluidized bed vessel, and the process was divided into two stages: the wetting stage and the drying stage. During the wetting stage, cold air at room temperature flows upwards through the bed to fluidize the dry material. Atomized water was sprayed at 20 ml/min into the bed until pre-determined moisture content was achieved. The drying stage was initiated immediately after the wetting stage. Approximately 8 g of powder was sampled every 5 minutes to measure the moisture content based on LOD during the drying stage. The end-point of drying was achieved once the product moisture content dropped below 1 %.

The drying in the MB45 was studied for a thin layer of samples (1g) and a thick layer of samples (5g) (see Figure 2-5). The drying in a batch fluidized bed was carried out in the MiniGlatt. The drying of different DCPA particle sizes was carried out by sieving the bulk materials into three particle size groups using sieve shaker. Sieves with mesh size of 53, 106, 150, 212 µm were used to separate the powders. Therefore, the small group is particles with a size of 53-106 µm, the medium group with a size of 106 - 150 µm and the large group with a size of 150 - 212 µm.

Parametric analysis was carried out using a factorial experimental design. For both dryers, four factors were taken into consideration: 1) the initial moisture content, 2) the inlet heating air temperature, 3) the inlet heating air mass flow rate and 4) the material loading in the dryer. The experimental design is shown in Table 2-1 and Table 2-2.

The design of experiments (DOE) was conduct using Minitab statistical software. The resulting Pareto charts and normal plots were also analyzed using Minitab. For the set of experiments using the MiniGlatt dryer, two different loadings, 0.8 kg, and 0.5 kg, were investigated. The initial moisture content ranges from 10 % to 20 % (measured as the mass of liquid divided by the mass of solid). The inlet air temperature has a high level of 80 °C and a low level of 60 °C. The inlet air flow should exceed the minimum fluidization velocity in order to achieve fluidization. A low level of 10 m^3/h was just enough to keep the fluidization state and a high level of 15 m^3/h was chosen for comparison. Similarly, for the GPCG-1, loadings of 3.0 kg and 4.0 kg were investigated. The same initial moisture content as the MiniGlatt was adopted (i.e., 10 % and 20 %) for the GPCG-1. As the GPCG-1 has much larger loadings, requiring significantly more drying time, the heating air temperature was set at 80 °C and 100 °C. The inlet airflow was also elevated to 40 m^3/h and 54 m^3/h for the GPCG-1.

2.3 Results and Discussion

The factors that affect drying in a fluidized bed are typically related to the initial moisture content of the materials, the heating temperature of the inlet air, the flow rate of the inlet air and the amount of material that is loaded in the chamber. Due to the different dryer geometries, the effect of the above parameters on the drying process may vary at different dryer scales. In this study, we compare the performance of the Glatt GPCG-1 and MiniGlatt.

The effect of each operating parameter on drying was examined. Furthermore, the interaction of different parameters is studied using Pareto charts and normal plots. At the end of this section, an energy efficiency analysis is introduced to investigate the overall drying behavior which could lead to a deeper fundamental understanding of drying processes.

2.3.1 Reproducibility of the drying process

Due to time and material costs, the fluidized bed drying experiments were not replicated for every condition. Preliminary experiments were conducted to ensure reproducibility of the drying process in the GPCG-1 and the MiniGlatt. Figure 2-6a shows 3 kg of DCPA with 20 % initial moisture dried in the GPCG-1 fluid bed dryer at 80 °C. Three samples were taken at a 5-second interval for each data point displayed and error bars showing the standard deviation are plotted in Figure 2-6a; the error bars are less than or equal to the size of the data points in Figure 2-6a. Since the fluid bed is a well-mixed system, the samples at the thief position should be representative of the entire fluid bed. The standard deviation for each data point is very small, with the largest value less than 0.58 % of moisture, indicating that the moisture content of the powder throughout the fluidized bed dryer is almost the same for a given time point. For the MiniGlatt, taking three samples for each data point would result in a loss of 10 % of the loaded materials, which may have impacted the drying results. Instead, the drying process was replicated three times for the same operating condition. Figure 2-6b shows 0.5 kg of DCPA with 25 % initial moisture dried in the MiniGlatt fluid bed dryer at 60 °C. All three of the drying curves in Figure 2-6b overlap to a large extent. The results show a good batch to batch.

2.3.2 Drying of DCPA in the GPCG-1

The effect of the initial moisture content on drying was investigated as shown in Figure 2-7. The bed temperature was recorded every 3 minutes (Figure 2-7b) as it is an important parameter for determining the drying status. In this work, the moisture content describes the mass of water per mass of dry powder (Figure 2-7a). The drying rate used in this study is defined as the loss of water (kg) per 1 kg of dry powder per minute, which can be calculated from the following equation

$$R = \frac{M_{t+\Delta t} - M_t}{\Delta t}$$

Eq. 2-1

where R is the drying rate, and M is the moisture content of the materials at drying time t.

The three drying stages can be easily distinguished from the drying rate curves (Figure 2-7c). During the preheating stage, the bed temperature rises quickly, as shown in Figure 2-7b, from room temperature (18 °C) to around 30 °C in 6 minutes when drying at 80 °C. The moisture content of the materials didn't change significantly as the drying rate is slow during the preheating stage. During the constant rate stage, the bed temperature remained constant (Figure 2-7b) and the moisture content dropped linearly with time, (Figure 2-7a) with the drying rate at its maximum (Figure 2-7c). For higher initial moisture content, longer drying times are required, and thus longer constant rate stages were observed (Figure 2-7a and b). When the moisture content dropped to around 1 %, the drying rate decreased significantly to a very low level. In this falling rate stage, the bed temperature increased (Figure 2-7b) as the supplied heat was no longer being used for evaporation.

The effect of drying temperature was studied with two levels of initial moisture content and the results are shown in Figure 2-8: panels a and b were obtained at 10 % initial moisture, and c and d were obtained at 20 % initial moisture. In Figure 2-8a the moisture content as a function of time is shown for three drying temperatures and an initial moisture content of 10 %. Slightly difference among three curves is observed due to the experimental error. Corresponding bed temperatures are shown in Figure 2-8b. It can be seen that most of the drying takes place in the constant rate stage with the moisture content dropping linearly with time (Figure 2-8a) and the bed temperature remaining constant (Figure 2-8b). As before, once moisture contents fall below ~1 % the bed temperature starts to increase (Figure 2-8b). As the temperature increases the drying rate increases (Figure 2-8a) and the bed temperature increases (Figure 2-8b). Similar results can be seen for an initial moisture content of 20 % in Figure 2-8c and d. However, it can be seen that the drying time is greatly increased with an increase in the initial moisture content.

The effect of air flux was studied with two levels of initial moisture content and the results are shown in Figure 2-9: panels a and b were obtained at 10 % initial moisture, and c and d were obtained at 20 % initial moisture. In Figure 2-9a and Figure 2-9c the moisture content as a function of time is shown for two air fluxes and initial moisture content of 10 % and 20 % respectively. Corresponding bed temperatures are shown in Figure 2-9b and Figure 2-9d. As observed previously, it can be seen that most of the drying takes place in the constant rate stage with the moisture content dropping linearly with time (Figure 2-9a and Figure 2-9c) and the bed temperature remaining constant (Figure 2-9b and Figure 2-9d). During the constant rate stage, the same temperature is observed in the bed for the two different air fluxes (see Figure 2-9b and Figure 2-9d).

The effect of initial loading was also studied with two levels of initial moisture content, and the results are shown in Figure 2-10: panels a and b were obtained at 10 % initial moisture, and c and d were obtained at 20 % initial moisture. In Figure 2-10a and Figure 2-10c the moisture content as a function of time is shown for two initial loadings and initial moisture content of 10 % and 20 % respectively. Corresponding bed temperatures are shown in Figure 2-10b and Figure 2-10d. As observed previously, it can be seen that most of the drying takes place in the constant rate stage. In addition, the larger loading of the material decreases the rate of drying.

When the same drying temperature was applied, with different air fluxes (Figure 2-9) and loadings (Figure 2-10), the bed temperature profiles have similar shapes, indicating that for the ranges we have examined a change of scale or air flux does not change the general drying behavior. Figure 2-11shows the effect of initial moisture on the end-point drying time for the different operating conditions in Figure 2-8, Figure 2-9 and Figure 2-10. The endpoint drying time is taken to be the time needed to reduce the moisture content to 1 %. Figure 2-11a and Figure 2-11b show the impact of initial moisture content on the total drying time for different drying temperatures. As the initial moisture content increased from 6 % to 10 % and 20 %, the resulting total drying time increased accordingly. For 6 % initial moisture, the total drying time dropped from 30 minutes at 60 ^{o}C to 24 minutes at 80 ^{o}C and to 18 minutes at 100 ^{o}C. Similar phenomena were observed for 10 % and 20 % initial moisture. In general, one can see that there is a fairly linear relationship between drying time and initial moisture content. The drying time ratio and the moisture content ratio is shown in Figure 2-11b were calculated as follows. The drying time ratio is defined as the ratio of the drying time at a given initial moisture content to the drying time at a 20 %

initial moisture content for DPCA powders under the same drying conditions. The moisture content ratio is defined as the ratio of given initial moisture content to the 20 % initial moisture content. It is observed in Figure 2-11b that the drying time ratio is proportional to the initial moisture content ratio, which indicates that the constant rate stage (zero order kinetics) dominates the drying process. Furthermore, the drying time ratio didn't vary much for drying at 60/80/100 °C – all three points lie nearly on top of one another (Figure 2-11b). Therefore, the interaction between drying temperature and initial moisture content can be neglected.

Figure 2-11c and Figure 2-11d illustrate the impact of initial moisture content on total drying time for different material loadings. Once again one can see that there is a fairly linear relationship between drying time and initial moisture content. Higher loading and initial moisture content lead to higher drying time. The drying time ratio of different loadings are 0.72, 0.67 and 0.80 for 6 %, 10 % and 20 % initial moisture content, respectively, which is comparable to the loading ratio, indicating that the drying time is proportional to the initial material loading.

The effects of initial moisture content, drying temperature, air flow rate and loading on the drying process were further confirmed with the Pareto chart of effects and normal plot shown in Figure 2-12. Pareto analysis [129] can help determine the factors that are responsible for the drying process. The drying time was regarded as the response for drying in the Pareto analysis as shown on the horizontal axis in Figure 2-12a. The listed factors on the vertical axis represent either a single operating condition or the interaction of several conditions. The confidence level for all intervals was set at 97.5 % (α = 0.025). Minitab uses Lenth's pseudo-standard error (PSE) for the error term, which assumes that random

error caused the variation in the smallest effects. The vertical red reference line indicates the significance of factors to the drying process. It can be observed that the initial moisture content dominates the drying time as it has the largest effect. The air flow rate and the loading have a smaller effect on drying compared to initial moisture content. The effect of drying temperature is the least important factor; however it is still significant. None of the factor interactions have a significant effect on the drying time. The normal plot is typically used to examine the distribution of data. In this study, the normal probability plot can be interpreted as an indication of whether the operating parameters affect the process positively or negatively. The fitted line indicates the position of the data point if the effect of a factor is zero. The points on the right indicate a positive effect and those on the left a negative effect. Thus, the further a point is from the fitted line, the larger the magnitude and statistical significance of the effect on drying time. It can be observed from the plot that increasing the initial moisture content and material loading will increase the drying time while increasing temperature and air flow rate will decrease the drying time. It can be concluded that all four parameters are independent of each other and have a significant effect on the end-point of the required drying time. The interaction effects were not found to be significant. The Pareto chart and the normal plot not only allow for a quantitative understanding of the effect of different parameters on drying but also provide a potential method of optimizing the drying process.

2.3.3 Drying of DCPA in MiniGlatt

In the MiniGlatt study, the material loading was reduced to 500 g and 800 g, which was approximately $^1/_8$ and $^1/_4$ of the loading in Glatt GPCG-1 fluidized bed dryer. The inlet air

flow rate was $^1/_4$ and $^1/_3$ of that used in GPCG-1. The heating temperature and initial moisture content were adopted at the same level as before: 60 °C/80 °C and 10 %/20 %.

The effect of initial moisture content was investigated first in the MiniGlatt. In Figure 2-13, we present results for 0.5 kg of material with different initial moisture contents (20 % and 10 %) that were dried at 80 °C with an inlet air flux of 15 m^3/h. As observed in the GPCG-1, the three drying stages can be easily distinguished from the drying rate curves (Figure 2-13c). The system reached the constant-rate stage very quickly as the bed temperature increased from 13 °C to 24 °C (Figure 2-13b). During the constant rate stage, the bed temperature remained constant (Figure 2-13b), and the moisture content dropped linearly with time (Figure 2-13a) with the drying rate at its maximum (Figure 2-13c). For material with higher initial moisture content, longer drying times are required and thus a longer constant rate stage was observed for the 20 % initial moisture sample (Figure 2-13a and b). When the moisture content dropped to around 1 %, the drying rate decreased significantly. In this falling rate stage, the bed temperature increased (Figure 2-13b) as the supplied heat was no longer being used for evaporation. When the initial moisture content in the material was lower, both MiniGlatt and GPCG-1 demonstrated a significant drying time reduction.

The effect of drying temperature was studied with two levels of initial moisture content and the results are shown in Figure 2-14: panels a and b were obtained at 10 % initial moisture, and c and d were obtained at 20 % initial moisture. In Figure 2-14a the moisture content as a function of time is shown for two drying temperatures and initial moisture content of 10 %. Corresponding bed temperatures are shown in Figure 2-14b. It can be seen that most of the drying takes place in the constant rate stage with the moisture content dropping linearly with time (Figure 2-14a) and the bed temperature remaining constant

(Figure 2-14b). As before, once moisture contents fall below ~1 % the bed temperature starts to increase (Figure 2-14b). As the temperature increases the drying rate increases (Figure 2-14a) and the bed temperature increases (Figure 2-14b). Similar results can be seen for initial moisture content of 20 % in Figure 2-14c and Figure 2-14d. Once again, it can be seen that the drying time is greatly increased with an increase in the initial moisture content. Increasing the drying temperature from 60 °C to 80 °C has only a small effect on the drying time.

The effect of air flux was studied with two levels of initial moisture content and the results are shown in Figure 2-15: panels a and b were obtained at 10 % initial moisture, and c and d were obtained at 20 % initial moisture. In Figure 2-15a and Figure 2-15c the moisture content as a function of time is shown for two air fluxes and initial moisture content of 10 % and 20 % respectively. Corresponding bed temperatures are shown in Figure 2-15b and Figure 2-15d. As observed previously, it can be seen that most of the drying takes place in the constant rate stage with the moisture content dropping linearly with time (Figure 2-15a and Figure 2-15c) and the bed temperature remaining constant (Figure 2-15b and Figure 2-15d). During the constant rate stage, the same temperature is observed in the bed for the two different air fluxes (see Figure 2-15b and Figure 2-15d). Increasing the air flux from 10 m^3/h to 15 m^3/h has a significant effect on the drying time.

The effect of initial loading was also studied with two levels of initial moisture content, and the results are shown in Figure 2-16: panels a and b were obtained at 10 % initial moisture, and c and d were obtained at 20 % initial moisture. In Figure 2-16a and Figure 2-16c the moisture content as a function of time is shown for two initial loadings and initial moisture content of 10 % and 20 % respectively. Corresponding bed temperatures are

shown in Figure 2-16b and Figure 2-16d. As observed previously, it can be seen that most of the drying takes place in the constant rate stage. Unlike the GPCG-1, higher material loading in the MiniGlatt did not extend the drying time.

Pareto analysis was also carried out for the MiniGlatt. As shown in Figure 2-17, the effect of material loading on the drying time was found to be no longer significant. Unlike the GPCG-1, moisture content and flowrate were found to have an equivalent effect on the drying time. Interestingly, the factor interaction between moisture content and flow rate was found to be significant for the MiniGlatt. As with the GPCG-1, increasing the heating air temperature from 60 °C to 80 °C still only had a small effect on the drying time.

2.3.4 Comparison of Oven Drying and Fluidized Bed Drying

The drying curve of both the oven drying and fluidized bed drying at 60 °C was compared in Figure 2-18 and Figure 2-19. For both dryers, higher loadings resulted in longer drying time. However, the characteristics of the drying curves were not changed. The fluidized bed drying can be considered as drying of a thin layer of particles because the mixing between the solid phase and gas phase is excellent. However, when comparing the fluidized bed drying curve and the MB45 drying curve, it was observed that the fluidized bed drying curve had a larger linear part. The unhindered period is longer in a fluidized bed dryer than in an oven dryer. This was due to the fact that the particles are static in an oven dyer and was direct contact with the aluminum weighing plate in the moisture analyzer. The heat transfer was mainly by the conduction between the particles and the aluminum plate. While in a fluidized bed dryer, the particles were fluidized and were surrounded by the heating air. The heat transfer was mainly by the conduction between the particles and the air. As the air has much smaller heat capacity than aluminum, the heat flow rate is much smaller

in a fluidized bed dryer than in an oven dryer. The heat transfer in an oven dryer is much faster than the mass transfer, and therefore the drying process is dominated by diffusion.

As reviewed in section 1.4.4, a drying curve can be described by the empirical models summarized in Table 1-1. Table 2-3 shows the fitting of MiniGlatt B1 case drying curve using different empirical models. Table 2-4 shows the fitting of the drying curve from the 5g DCPA drying in MB45 at 60 °C using different empirical models. For both drying curves, out of the six empirical models, the Verma model failed to fit the drying curve. The Page model and the Midilli-Kucuk model had the best fitting for the experimental data. The Midilli-Kucuk model had a slightly better fitting than the Page model. This could be due to the fact that the Midilli-Kucuk model has a linear term other than the exponential decaying term, which results in a better fitting for the unhindered drying period.

To compare the mass transfer between the oven drying and the fluidized bed drying, the diffusion model was applied to both the drying curves shown in Figure 2-18 and Figure 2-19. The model is derived from Fick's second law of diffusion which was discussed in Sec 1.4.3 previously.

$$MR = \frac{X - X_{eq}}{X_0 - X_{eq}} = \frac{6}{\pi^2} \sum_{n=1}^{\infty} \frac{1}{n^2} exp\left[-n^2 \frac{\pi^2 D_{eff} t}{d^2}\right]$$

Eq. 2-2

where MR stands for moisture ratio. X_0 and X_{eq} are the initial moisture content and the equilibrium moisture content. d is the diameter of the particles. n is a positive integer. t is time. At a sufficiently long drying time, the above equation can be simplified to:

$$MR = \frac{6}{\pi^2} exp\left(-\frac{\pi^2 D_{eff} t}{d^2}\right)$$

Eq. 2-3

Therefore,

$$\ln(MR) = \ln\left(\frac{M - M_e}{M_0 - M_e}\right) = ln\left(\frac{6}{\pi^2}\right) + \left(\frac{-D_{eff} n^2 \pi^2}{d^2}\right) t$$

Eq. 2-4

If we plot $\ln(MR)$ against the time, the slope of the line will be:

$$k = \frac{-D_{eff}\pi^2}{r^2}$$

Eq. 2-5

Figure 2-20 and Figure 2-21 present the $\ln(MR)$ vs. t for the drying cases described above. The D_{eff} is summarized in Table 2-5. The D_{eff} was constant during the unhindered drying period. The D_{eff} started to drop as the drying process entered the hindered drying period. In MB45, the effective diffusivity reduced from 1.04×10^{-11} to 2.54×10^{-12} (4.11x) when the loading was increased from 1g to 5g. For MiniGlatt, the D_{eff} reduced from 3.46×10^{-12} to 8.81×10^{-13} (3.92x) when the loading was increased from 100g to 500g. The D_{eff} reduces when the loading is higher. Compare between the MB45 and the MiniGlatt, the D_{eff} in MiniGlatt is much smaller than the oven drying 1 g case (approximately 10 folds). The D_{eff} of the 5 g case in MB45 is comparable to the 100g case in MiniGlatt but is still much larger than the 500g case in MiniGlatt. In conclusion, the D_{eff} is generally larger in an oven dryer than in a fluidized bed dryer.

2.3.5 Effect of Particle Size

It is often believed that the smaller particles should have a faster drying rate than the larger particles because 1) the smaller particles have a larger surface area for a given total volume, and 2) the diffusion from the core to the surface takes shorter distance for smaller particles. The particles have a distribution of particles sizes and the required drying time for different particle sizes in a fluidized bed dryer could be potentially different. This is important when the pharmaceutical granules can sometimes have a broad particle size distribution within the same bulk of materials.

Figure 2-22 shows the DCPA cumulative particle size distribution after being sieved and categorized into three groups (small, medium and large). The d50 of the three groups of particles are 79 μm, 119 μm and 161 μm for the small, medium, and large groups, respectively.

Figure 2-23 presents the drying curve of three particle size groups of DCPA particle drying in MiniGlatt with the drying condition of 40% initial moisture content, 500 g of loading, 15 m^3/h air flow rate and 60 °C air temperature. It was discovered that the drying rate of the three particle size groups was similar. It can be explained by the fact that the fluidized bed drying is limited by heat transfer due to the relatively small air heat capacity. The drying rate is determined by the heat transfer rate. As the operating conditions were the same for all of the three groups, the determining factor would be the heat transfer area. It was reported that heat transfer in a fluidized bed drying occurs only at a few distances above the air distributor [94]. Therefore, the heat transfer area is the surface area of the air distributor, which is the same during the drying of all the three particle size groups. Therefore, the drying rate for different DCPA particle sizes in MiniGlatt was similar.

2.3.6 Energy Efficiency Analysis

In this study, energy efficiency is defined as the ratio of energy used for water evaporation to the input energy. The energy efficiency can thus be calculated as follows:

$$Energy\ efficiency = \frac{energy\ used\ for\ water\ evaporation}{input\ energy}$$

$$= \frac{moisture\ content \times material\ loading \times heat\ of\ evaporation}{air\ flux \times (T_{inlet} - T_{outlet}) \times drying\ time \times specific\ heat\ capacity\ of\ air}$$

For a given initial moisture content and material loading, both the heating temperature and air flux can be adjusted to affect the drying process. As discussed in the previous section, increasing the heating temperature only had a small effect on the drying time. In order to compare different cases, we define the energy efficiency ratio as the ratio of energy efficiencies for two different operating conditions. In Figure 2-24 we show the energy efficiency ratio for the GPCG-1 for different temperatures and moisture contents (Figure 2-24a) and different air fluxes and moisture contents (Figure 2-24b). Analogous results are shown in Figure 2-25 for the MiniGlatt. As shown in Figure 2-24a and Figure 2-25a, the energy efficiency for drying at 60 °C is around 30 % higher than drying at 80 °C for both the GPCG-1 and MiniGlatt indicating that a relatively low heating temperature is favorable in terms of energy efficiency. Increasing the drying temperature from 80 °C to 100 °C yields a decrease in energy efficiency (Figure 2-24a) for the GPCG-1. By increasing the air flux, the energy efficiency is increased by a moderate amount as shown in Figure 2-24b and Figure 2-25b. Therefore, in order to achieve a high energy efficiency profile for the parameter ranges we have examined, low temperature and high air flux should be used in the drying process.

A mass and heat balance was carried out at the external surface of the wet particles

$$k(c_{g,in} - c_{g,out})\Delta H_{vap} = h(T_\infty - T_{bed})$$

Eq. 2-6

where $c_{g,in}$ and $c_{g,out}$ are the inlet and outlet moisture content of the air, T_∞ is the ambient drying temperature, T_{bed} is the bed temperature and h and k are the heat and mass transfer coefficients, respectively. ΔH_{vap} is the latent heat of water vapor which is 2260 kJ/kg [130]. Therefore, *h/k* represents the energy efficiency coefficient which can be expressed as

$$\frac{h}{k} = \frac{(c_{g,in} - c_{g,out})\Delta H_{vap}}{T_\infty - T_{bed}}$$

Eq. 2-7

h/k describes the amount of moisture removed per unit of energy consumed for a given effective surface area. Thus, higher values of *h/k* indicate higher energy efficiencies. The effect of the operating parameters on the energy efficiency coefficient for the MiniGlatt is shown in Figure 2-26. The *h/k* profiles of drying were similar to that of the drying rate curve. Three stages can be observed: the energy efficiency coefficient increased slowly during the preheating stage, then reached a maximum value during the constant rate stage and finally dropped quickly to almost zero during the falling rate stage.

Figure 2-26 illustrates the *h/k* profile for different material loadings. In the smaller MiniGlatt, different loadings were found to have no effect on drying time, indicating that unless the scale of the fluidized bed drying is changed and the resulting fluidization behavior of the materials is changed during the drying, material loading does not affect the

energy efficiency coefficient. It is often difficult to characterize the fluidization status during drying since the drop of moisture content will promote fluidization [63]. High loadings can potentially increase the risk of defluidization, clumping of powders or other undesired situations when the air flux is insufficient. Similar results were found when different temperatures, air flux, and initial moisture content were applied (figures not shown here). Increasing the drying temperature decreases the drying times slightly. However, the *h/k* ratio dropped noticeably at the higher temperature for all three drying stages. Therefore, if energy utilization is of prime concern, drying should be kept at lower temperatures to maximize energy efficiency. The energy efficiency coefficient for the constant rate stage increased up to 50 % when the air flux increased from 10 m^3/h to 15 m^3/h. High air flux not only helps promote mass transfer between the gas and liquid phase, achieving a higher energy efficiency ratio but also reduces the drying time so that less energy is consumed overall. The initial moisture content is a measure of the amount of water/solvent in the material, and therefore it is not surprising that it did not have an effect on the energy efficiency coefficient. However, since the maximum energy efficiency coefficient is reached during the constant rate stage, drying materials with a higher initial moisture content result in a larger proportion of the drying process to occur at the maximum energy efficiency coefficient.

2.3.7 Comparison of GPCG-1 and MiniGlatt

The GPCG-1 and the MiniGlatt have different bed geometries. The GPCG-1 is a cylindrical fluidized bed dryer, providing a homogenous airflow profile along the vertical axis. The MiniGlatt has a lower conical section in the body chamber. The inlet air flow is much higher at the bottom than that at the top due to the cross-sectional area difference. Spouted

fluidization is usually observed in this type of geometry[76]. For the two fluidized bed dryers, the initial moisture content, the drying temperature and the air flux show a significant effect on the drying process. The initial loading is important to the GPCG-1, however, for the MiniGlatt the effect is not significant. This could be due to the geometry differences between the two fluidized bed dryers. Tanfara et al.[131] discovered that in a conical fluidized bed dryer, a centralized core flow pattern could be observed at a high air flow rate. Increasing the loading of materials will enhance the centralized flow pattern and results in better circulation of powders in the conical body chamber. Therefore, in the MiniGlatt, the powders have a better chance to be in contact with the drying air.

2.4 Conclusion

The impact of the operating parameters on the drying time and energy efficiency of the drying process was investigated in this chapter via parametric analysis. Initial moisture content, material loading, heating air temperature, and air flux were examined for their effect on drying. Two fluidized bed dryers, the Glatt GPCG-1, and MiniGlatt, the former one with a more cylindrical-like chamber (with respect to a smaller entrance angle) and the latter one conical, were studied using DCPA powders. The constant rate stage was found to dominate the drying process for all process conditions. Through Pareto analysis, the effects of all parameters were reviewed quantitatively. For the small dryer, the initial moisture content and air flux affected the drying time significantly for the conditions we examined. For the larger dryer, the effect of loading was as important as air flux for the present study. It was found that for both sizes of fluidized bed dryers, the heating air temperature, though not insignificant, had the least impact on drying time for the conditions we examined. For the GPCG-1, the interaction effects were found not to be important.

However, in the small scale MiniGlatt dryer, the interaction of the initial moisture content and the air flux could not be neglected, which should be further examined.

Energy efficiency analysis was carried out based on a simple mass and heat balance. It was found that drying had a higher energy efficiency for low temperatures and high air flux for the conditions we examined. The energy efficiency coefficient *h/k* was evaluated by studying the mass and heat balance at the surface of the particles. The energy efficiency coefficient is low during the preheating stage as heating air is used to raise the bed temperature. During the constant rate stage, *h/k* reaches its maximum value before the moisture content drops to a critical level. In the falling rate stage, *h/k* drops to almost zero as capillary forces start to dominate the drying process. Higher initial moisture content was found to have higher average energy efficiency as drying remains in the constant rate stage, and thus has the maximum *h/k* value, for a larger proportion of the process.

Our work serves to characterize the performance of fluidized bed dryer systems and provide physical insight into the fundamentals of drying of porous materials. At the same time, our results are for a limited number of drying conditions, two pieces of equipment and only one material. Further work is needed to see if the results we have obtained here can be generalized to other materials and drying conditions. It would also be of interest to examine other fluidized bed dryers to see how equipment changes might affect the drying process.

2.5 Figures for Chapter 2

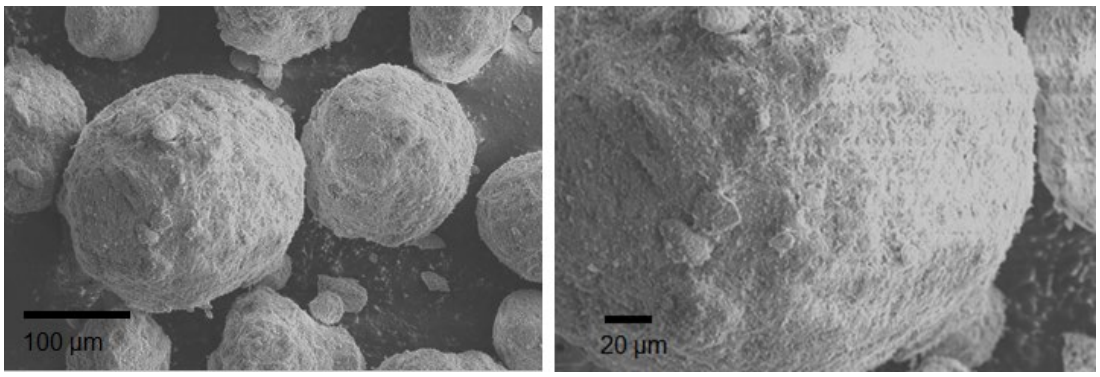

Figure 2-1: SEM images of dibasic calcium phosphate anhydrous (DCPA).

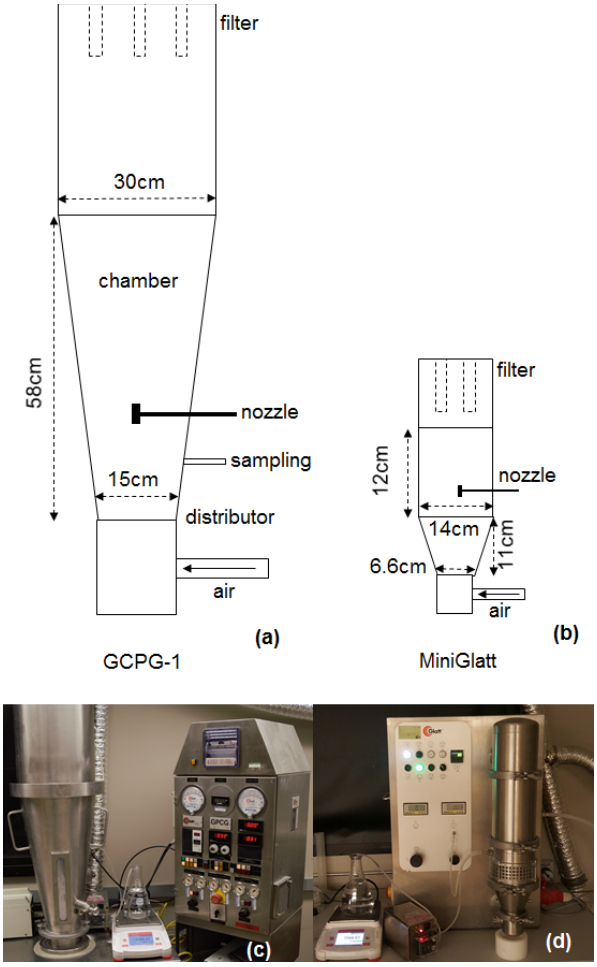

Figure 2-2: Schematics of a) Glatt GCPG-1 and b) MiniGlatt fluidized bed dryers and the experimental setup for c) Glatt GCPG-1 and d) MiniGlatt fluidized bed dryers.

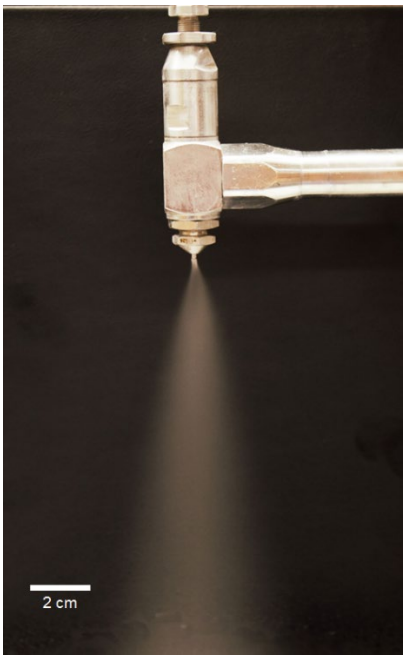

Figure 2-3: The two-phase nozzle spraying water

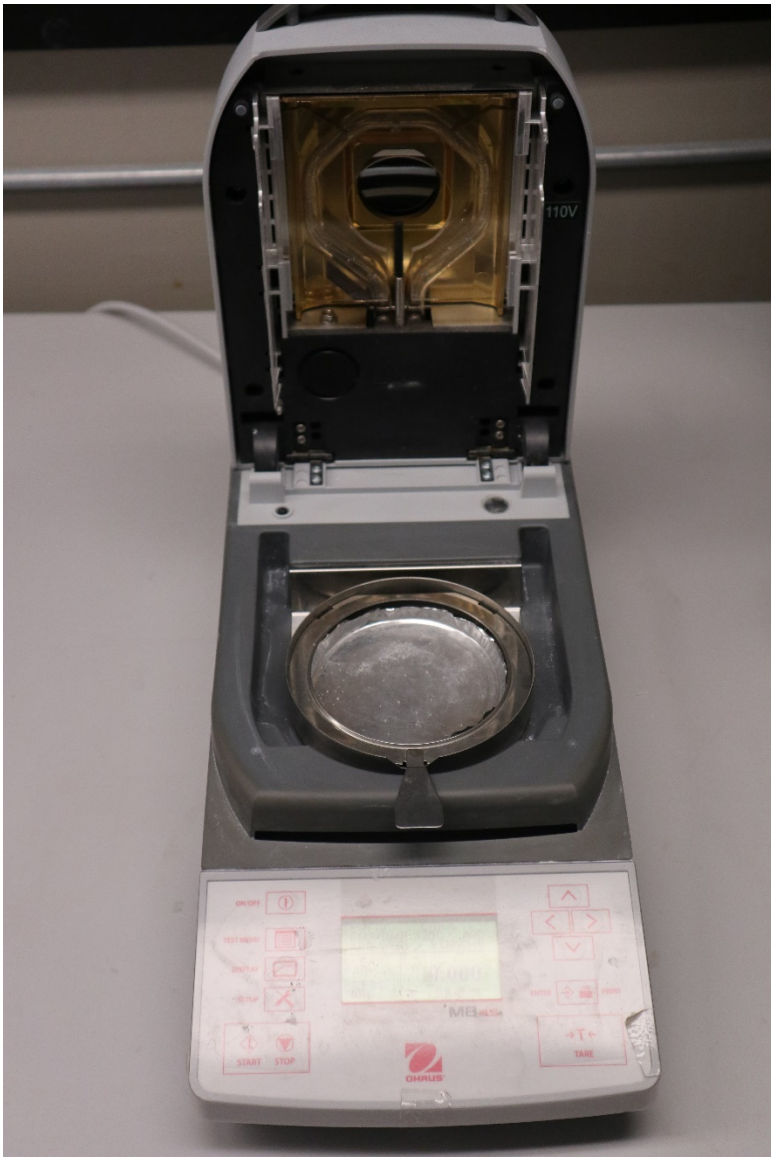

Figure 2-4: MB45 moisture analyzer

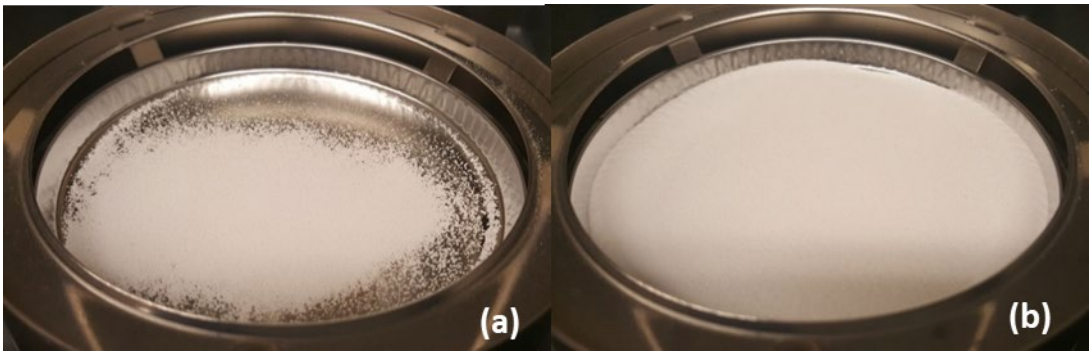

Figure 2-5: DCPA powders drying in MB45 with (a) 1g loading (thin layer) and (b) 5g loading (thick layer)

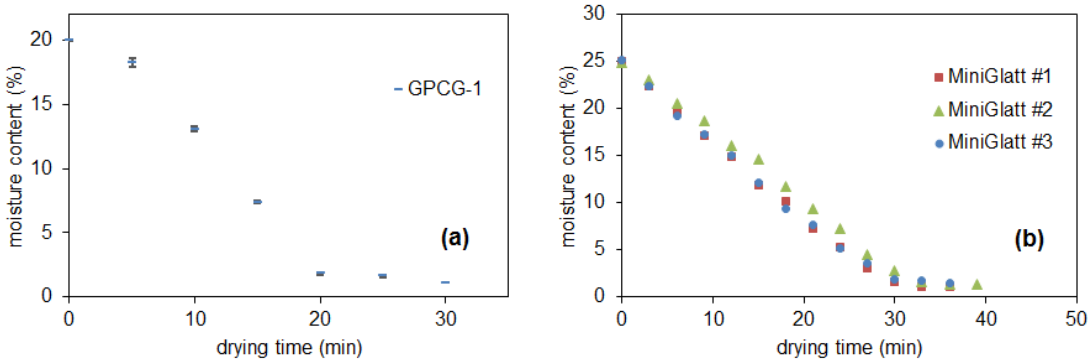

Figure 2-6: Drying curves of DCPA with a) sampling variability for the Glatt GCPG-1 and b) batch to batch reproducibility for the MiniGlatt fluidized bed dryer.

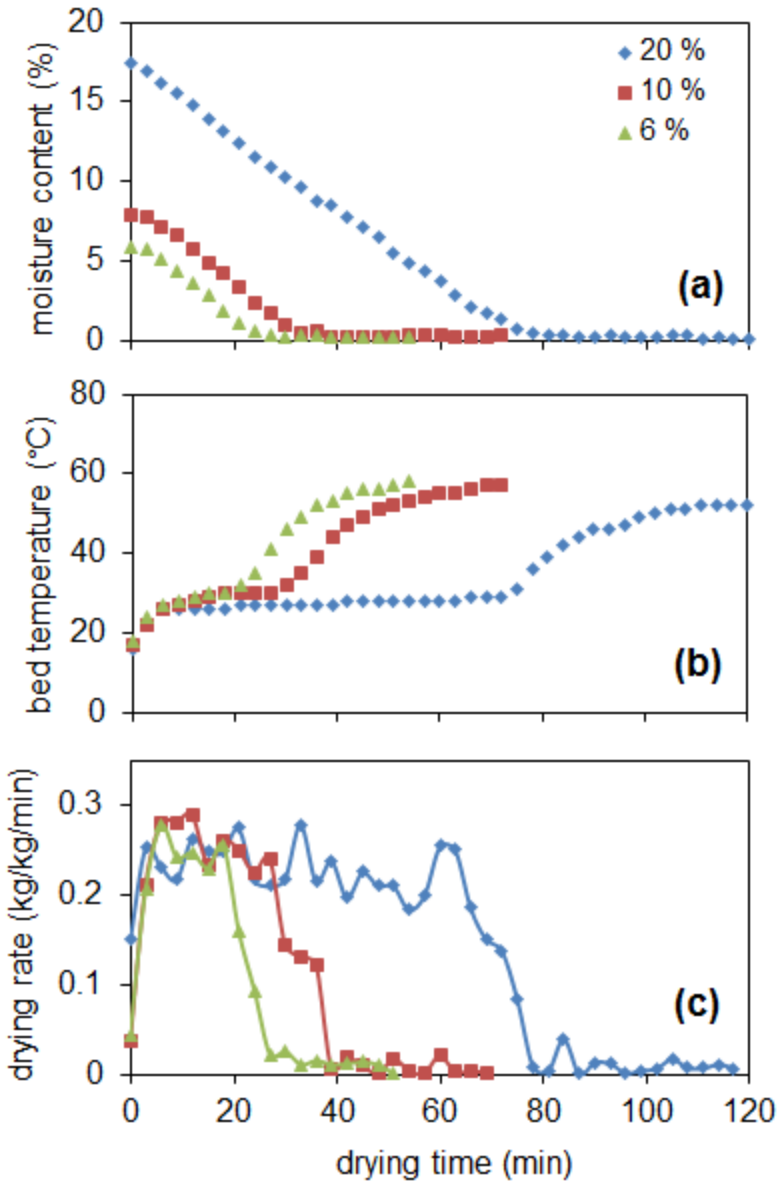

Figure 2-7: Effect of the initial moisture content on drying of DCPA using the GCPG-1 (T = 80 °C, air flux = 40 m^3/h, loading = 3 kg) for a) sample moisture content vs. drying time, b) bed temperature vs. drying time and c) drying rate vs. drying time.

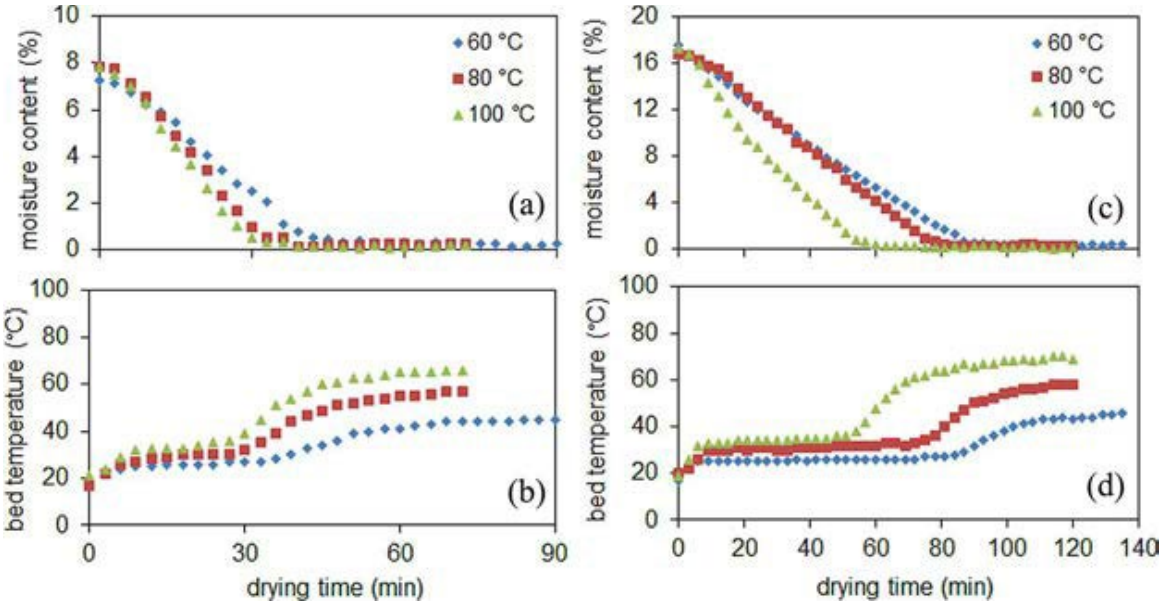

Figure 2-8: Effect of the inlet air temperature on drying of DCPA using the GCPG-1 (air flux = 40 m^3/h, loading = 3 kg) for a) sample moisture content vs. drying time and b) bed temperature vs. drying time at 10 % initial moisture content. c) Sample moisture content.

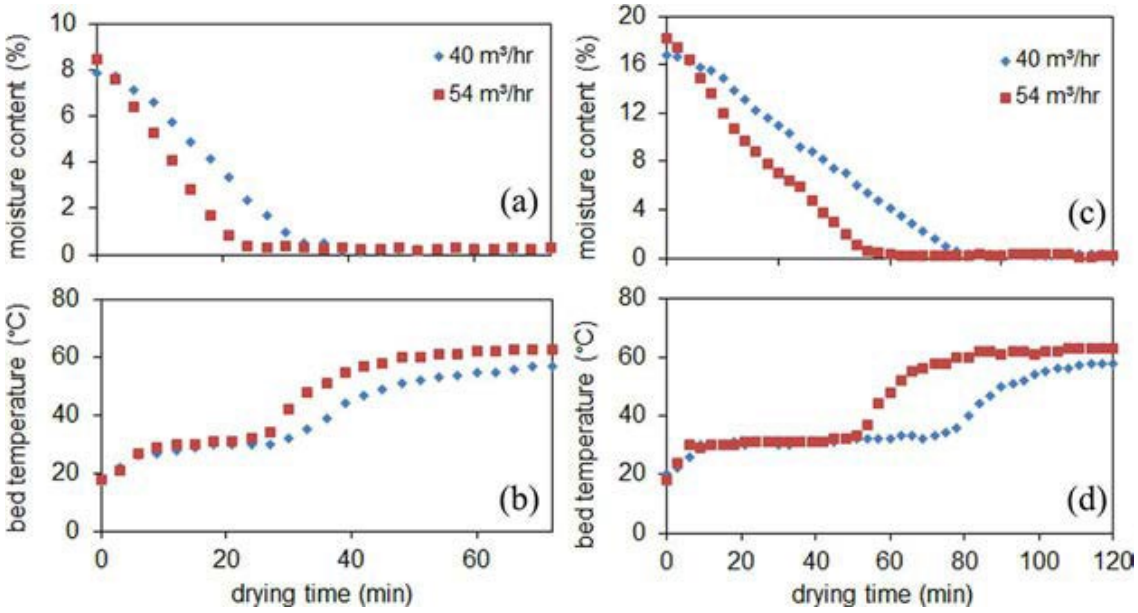

Figure 2-9: Effect of the inlet air flux on drying of DCPA using the GCPG-1 (T = 80 °C, loading = 3 kg) for a) sample moisture content vs. drying time and b) bed temperature vs. drying time at 10 % initial moisture content. c) Sample moisture content vs. drying time and d) bed temperature vs. drying time at 20 % initial moisture content.

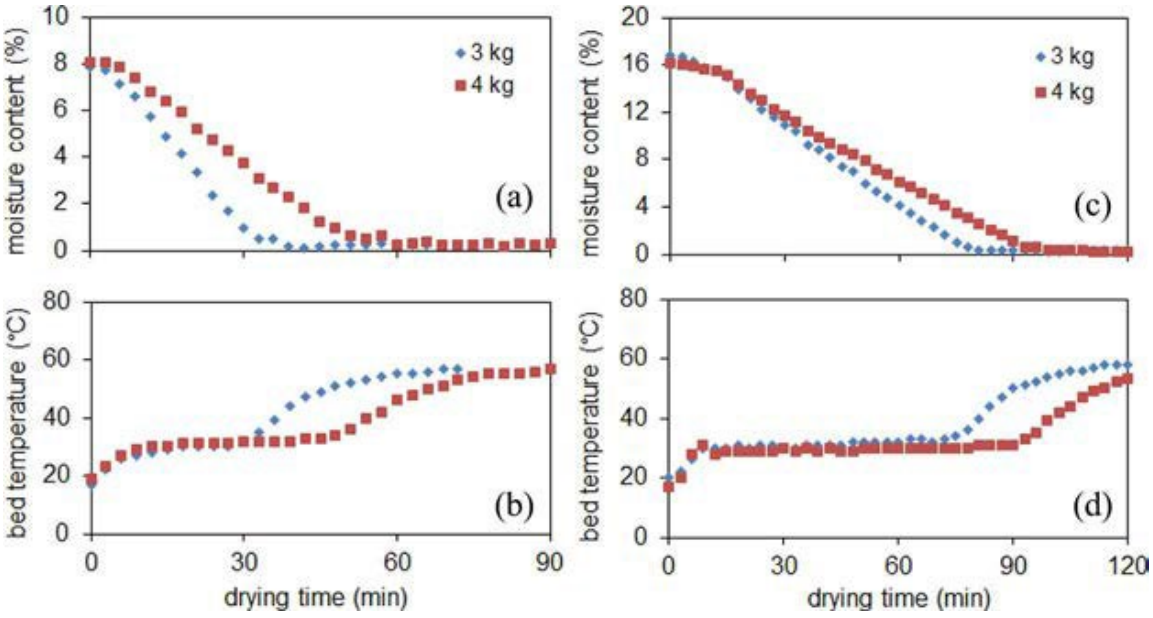

Figure 2-10: Effect of the material loadings on drying of DCPA using the GCPG-1 (T = 80 °C, air flux = 40 m^3/h) for a) sample moisture content vs. drying time and b) bed temperature vs. drying time at 10 % initial moisture content. c) Sample moisture content vs. drying time and d) bed temperature vs. drying time at 20 % initial moisture content.

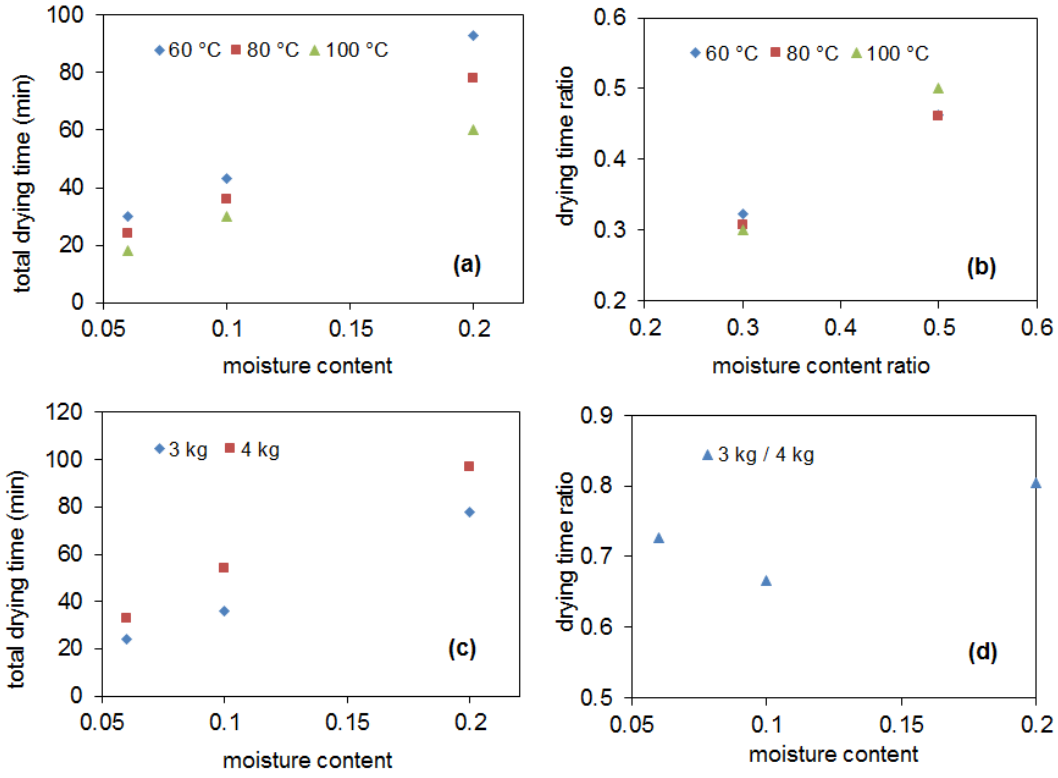

Figure 2-11: Impact of the initial moisture content on the end-point drying time for a) different inlet air temperatures and c) different material loadings. Drying time ratio as a function of the moisture content for b) different inlet air temperatures and d) different material loadings.

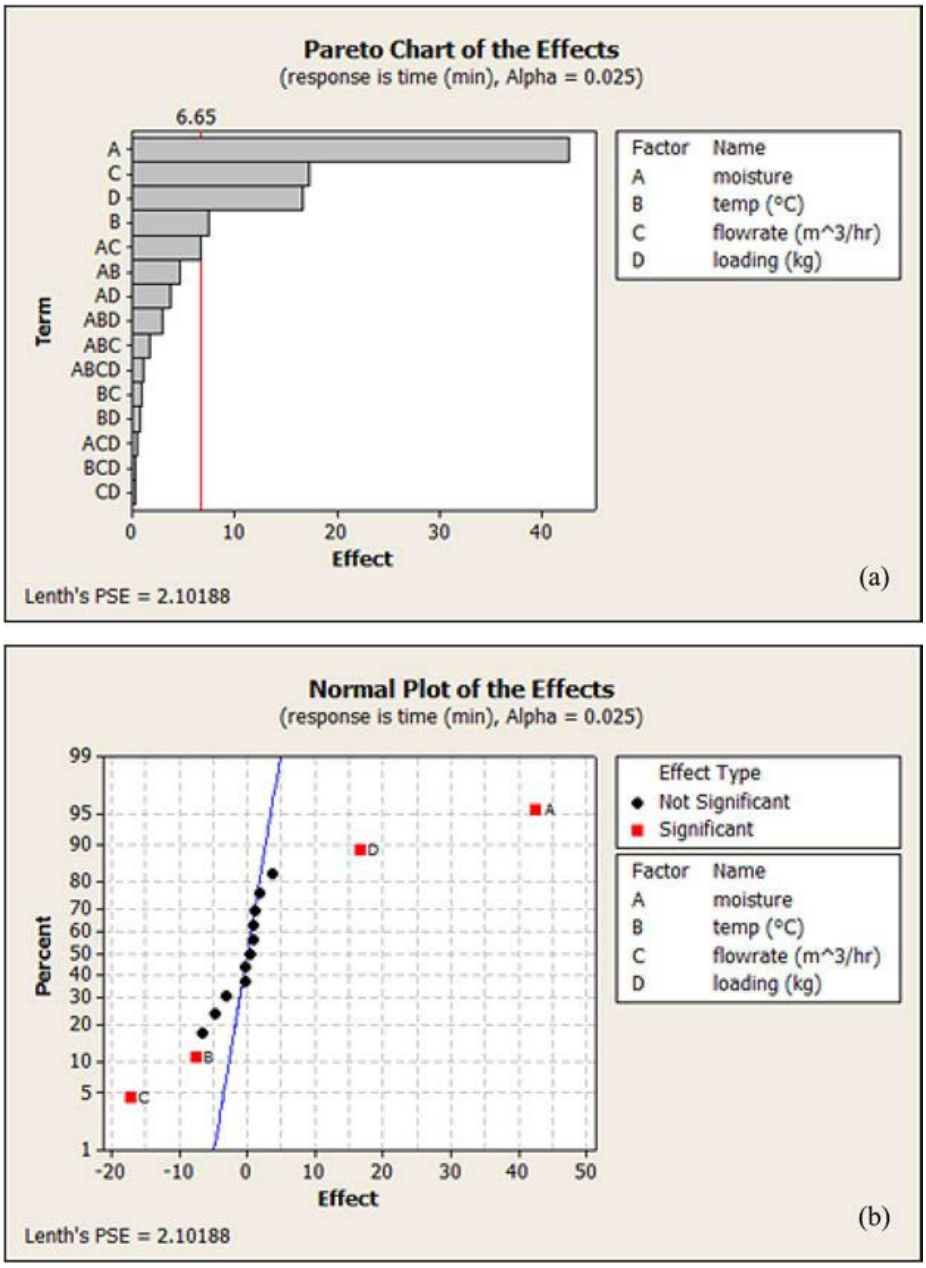

Figure 2-12: Two-level factorial analysis for drying of DCPA using the GCPG-1: a) Pareto charts of the effects and b) normal plot of the effects.

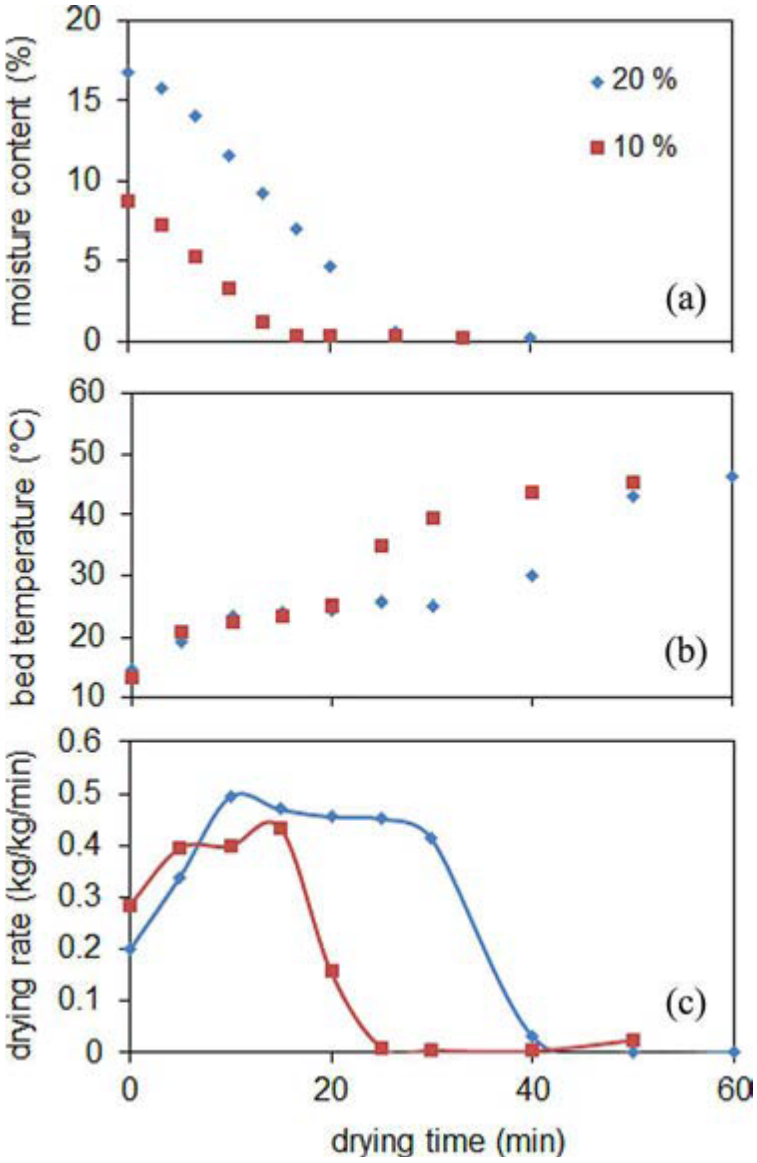

Figure 2-13: Effect of the initial moisture content on drying of DCPA using the MiniGlatt (T = 80 °C, air flux = 15 m^3/h, loading = 0.5 kg) for a) sample moisture content vs. drying time, b) bed temperature vs. drying time and c) drying rate vs. drying time.

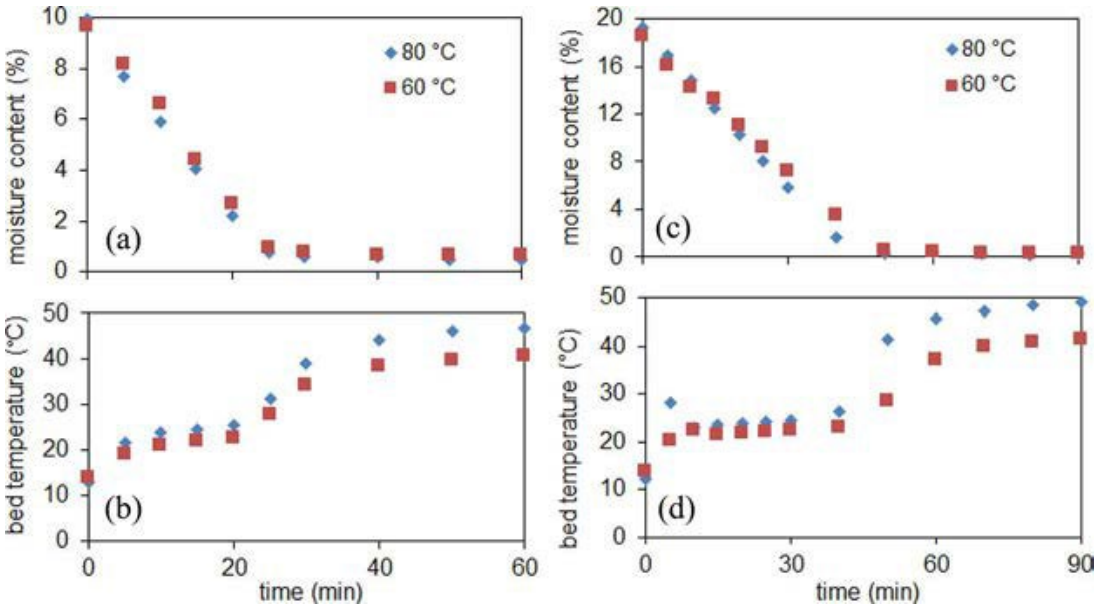

Figure 2-14: Effect of the inlet air temperature on drying of DCPA using the MiniGlatt (air flux = 15 m^3/h, loading = 0.8 kg) for a) sample moisture content vs. drying time and b) bed temperature vs. drying time at 10 % initial moisture content. c) Sample moisture content vs. drying time and d) bed temperature vs. drying time at 20 % initial moisture content.

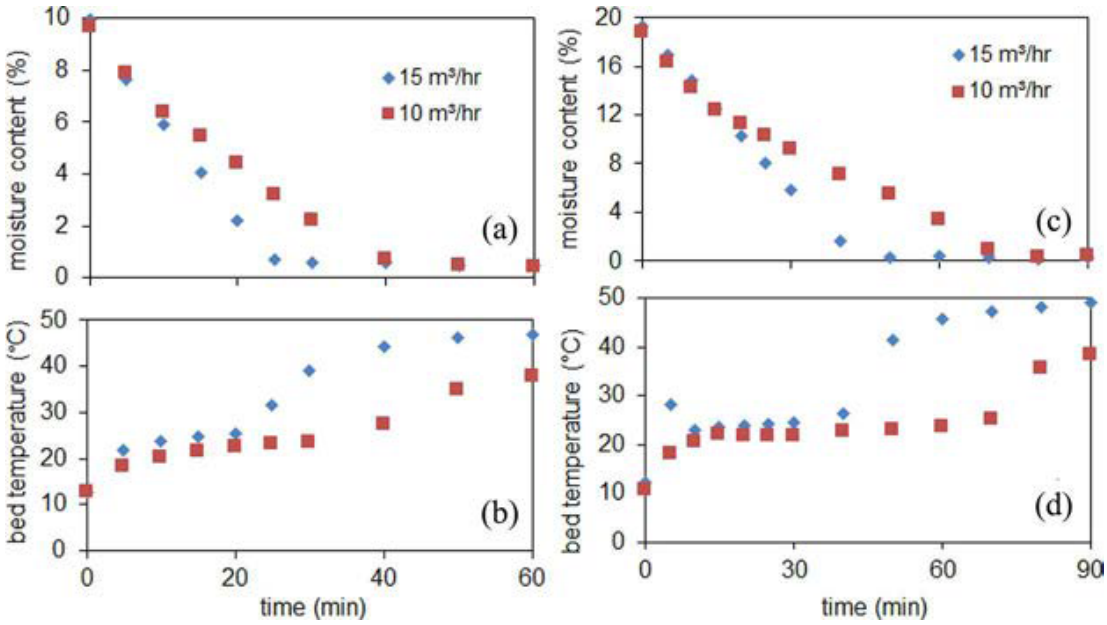

Figure 2-15: Effect of the inlet air flux on drying of DCPA using the MiniGlatt (T = 80 °C, loading = 0.8 kg) for a) sample moisture content vs. drying time and b) bed temperature vs. drying time at 10 % initial moisture content. c) Sample moisture content vs. drying time and d) bed temperature vs. drying time at 20 % initial moisture content.

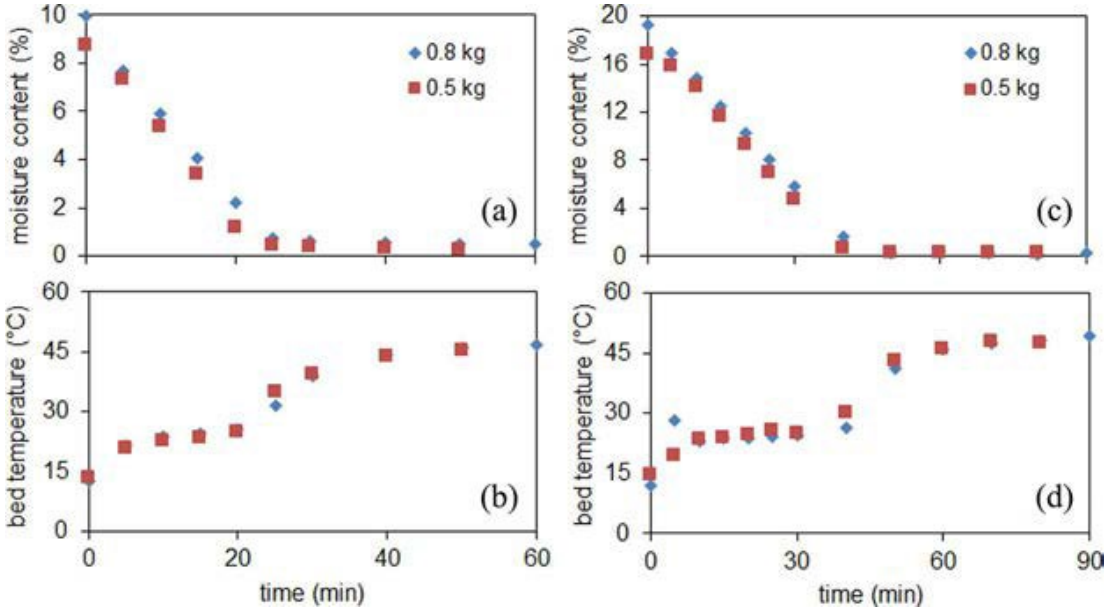

Figure 2-16: Effect of the material loadings on drying of DCPA using the MiniGlatt (T = 80 °C, air flux = 15 m^3/h) for a) sample moisture content vs. drying time and b) bed temperature vs. drying time at 10 % initial moisture content. c) Sample moisture content vs. drying time and d) bed temperature vs. drying time at 20 % initial moisture content.

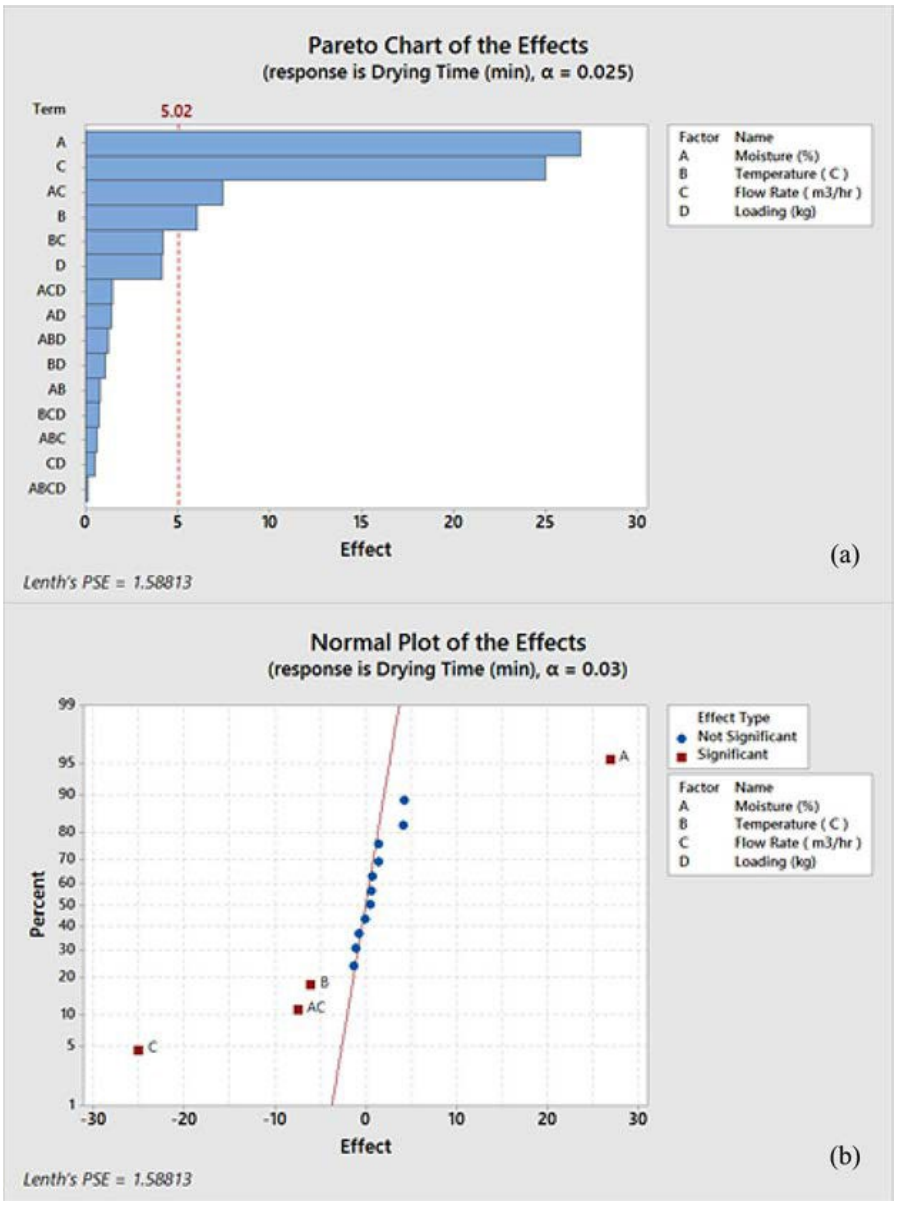

Figure 2-17: Two-level factorial analysis for drying of DCPA using the MiniGlatt: a) Pareto charts of the effects and b) normal plot of the effects.

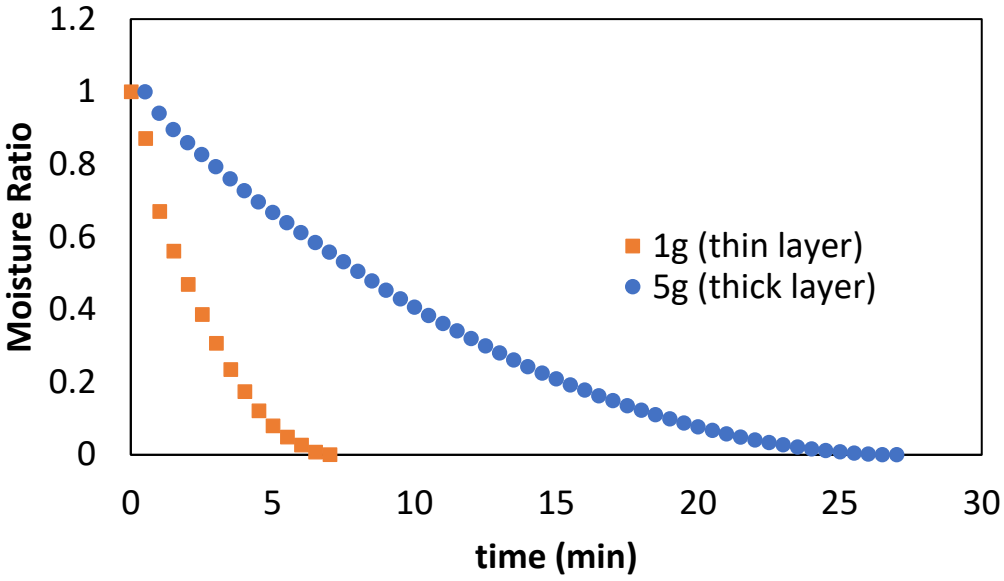

Figure 2-18: Oven drying in MB45 with loadings of 1g and 5g at 60 °C

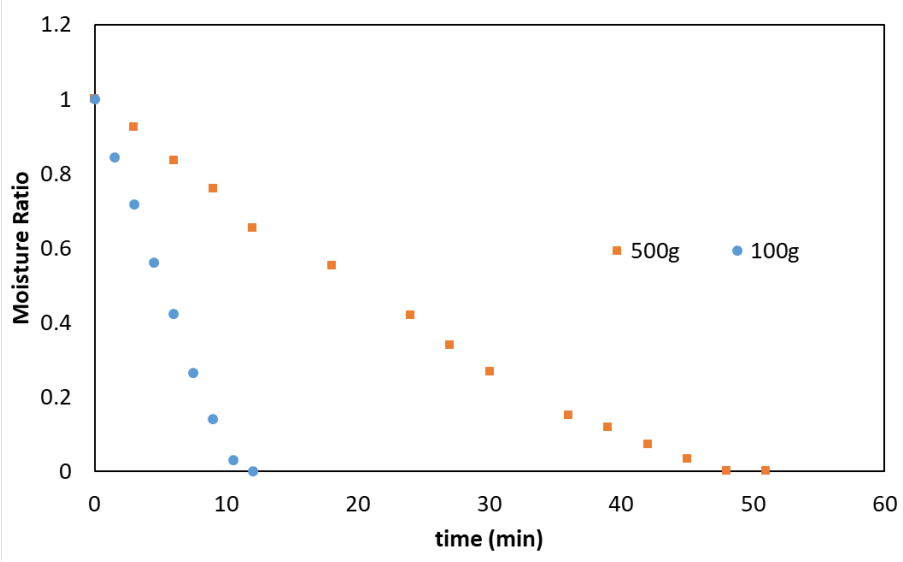

Figure 2-19: MiniGlatt drying with loadings of 100g and 500g at 60 °C.

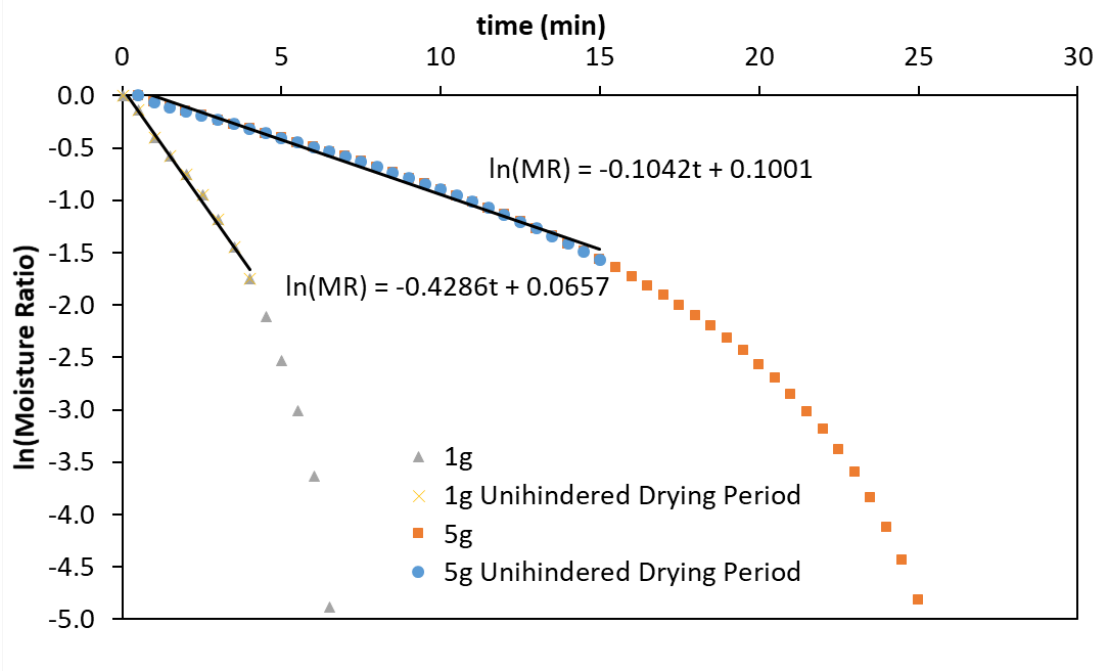

Figure 2-20: Diffusion model fitting of oven drying in MB45 with loadings of 1g and 5g at 60 °C.

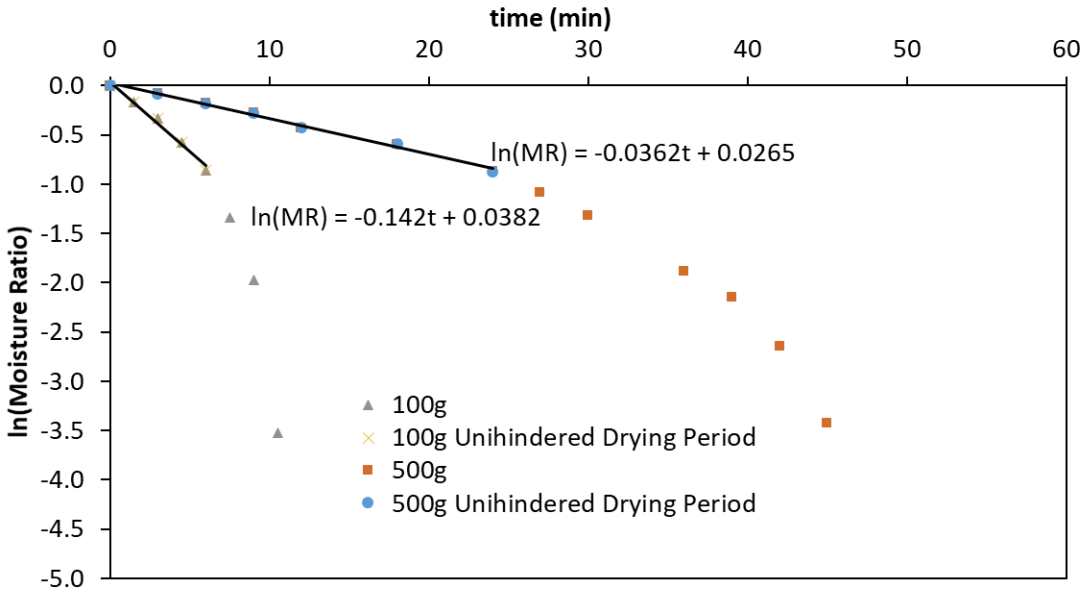

Figure 2-21: Diffusion model fitting of MiniGlatt drying with loadings of 100g and 500g at 60 °C.

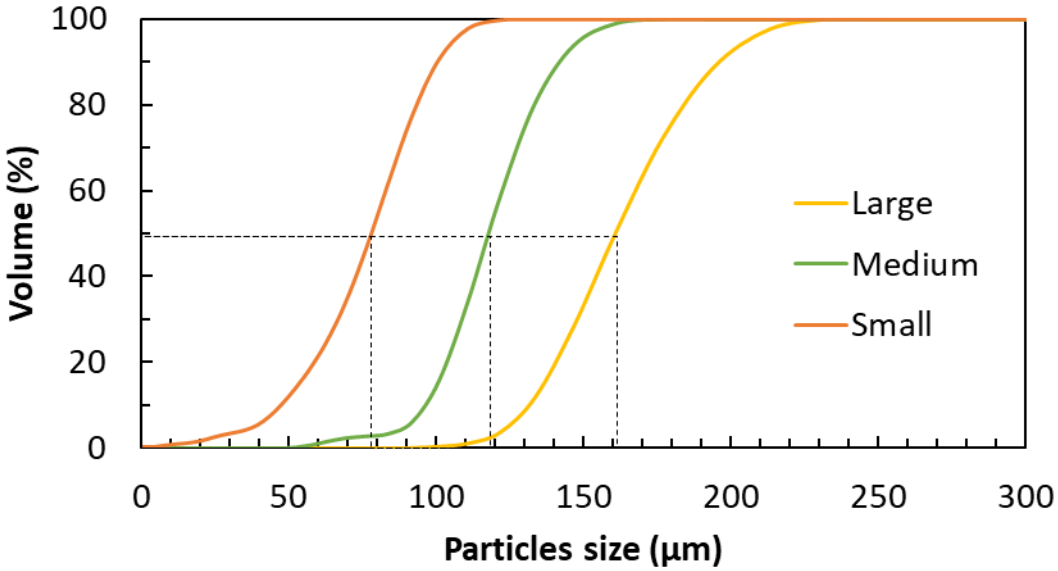

Figure 2-22: Cumulative particle size distribution of DCPA after being sieved.

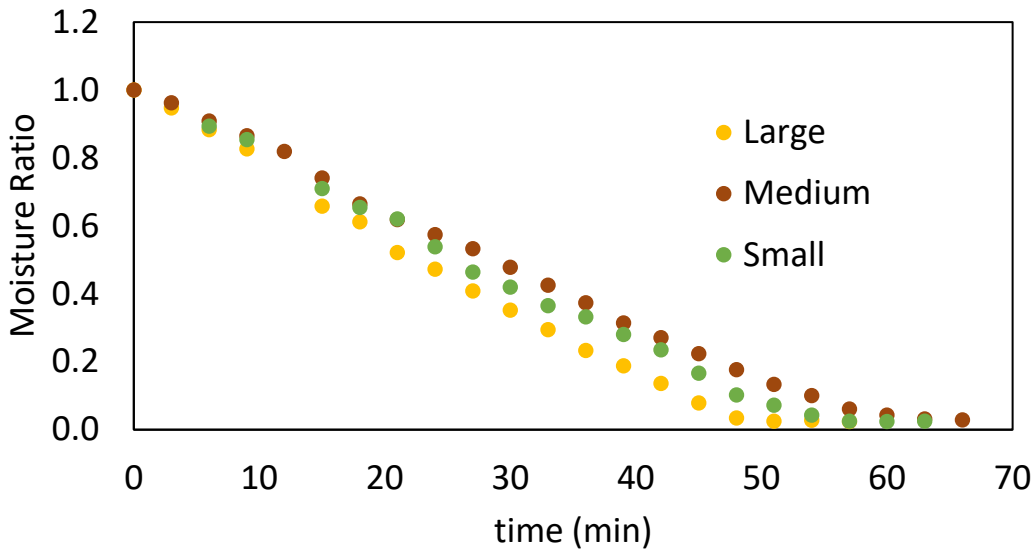

Figure 2-23: Drying curve of different particle size of DCPA drying in MiniGlatt with the drying condition of 40% initial moisture content, 500 g of loading, 15 m^3/h air flow rate and 60 °C air temperature.

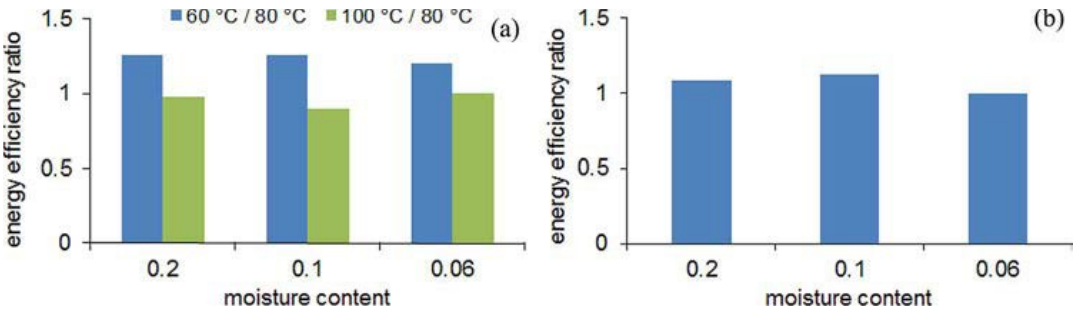

Figure 2-24: Energy efficiency ratios for the GCPG-1 for different moisture contents. a) The ratios of the energy efficiencies for drying air temperatures of 60 °C and 80 °C (blue bars); and 100 °C and 80 °C (green bars). Air flux = 54 m^3/h and loading = 3 kg. b) The ratios of the energy efficiencies for inlet air fluxes of 54 m^3/h and 40 m^3/h. T = 80 °C and loading = 3 kg.

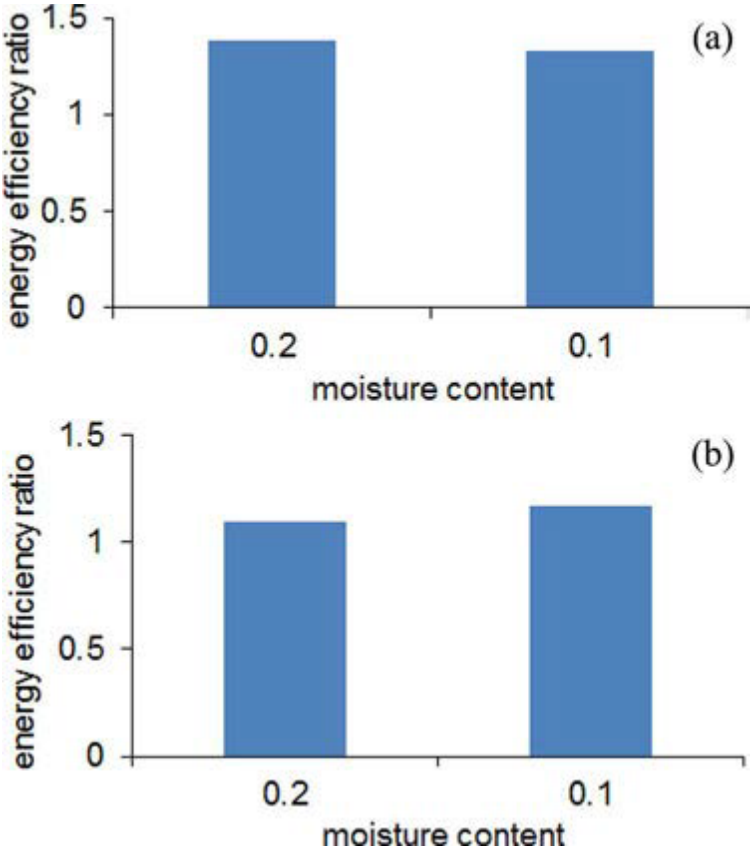

Figure 2-25: Energy efficiency ratios for the MiniGlatt for different moisture contents. a) The ratios of the energy efficiencies for drying air temperatures of 60 °C and 80 °C. Air flux = 15 m^3/h and loading = 0.8 kg. b) The ratios of the energy efficiencies for inlet air fluxes of 15 m^3/h and 10 m^3/h. T = 80 °C and loading = 0.8 kg.

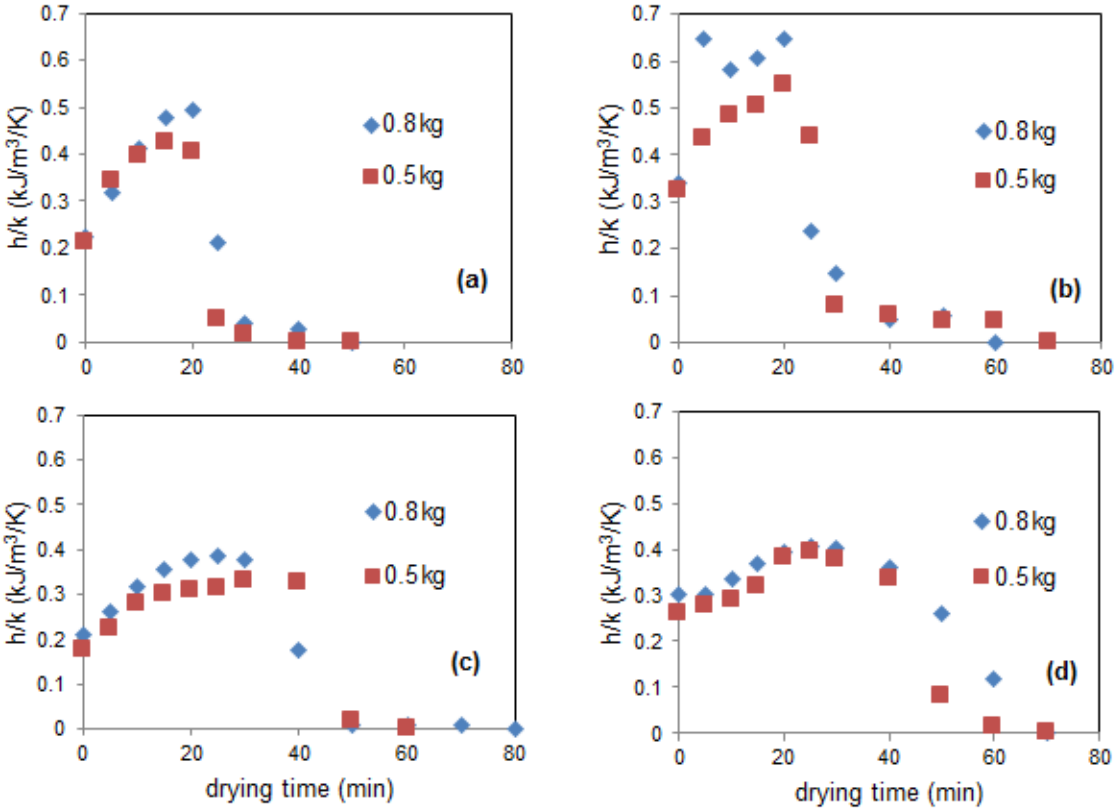

Figure 2-26: Effect of loading on energy efficiency coefficient h/k. a) T = 80 °C, air flux = 15 m³/h, 10 % initial moisture; b) T = 60 °C, air flux = 15 m³/h, 10 % initial moisture; c) T = 80 °C, air flux = 10 m³/h, 10 % initial moisture; d) T = 60 °C, air flux =10 m³/h, 10 % initial moisture.

2.6 Tables for Chapter 2

Table 2-1: MiniGlatt experimental design

	Conditions			
Test #	Loading (kg)	Initial moisture (%)	Heating temperature (°C)	Flow rate (m^3/h)
A1	0.8	20	80	15
A2	0.8	20	60	15
A3	0.8	20	80	10
A4	0.8	20	60	10
A5	0.8	10	80	15
A6	0.8	10	60	15
A7	0.8	10	80	10
A8	0.8	10	60	10
B1	0.5	20	80	15
B2	0.5	20	60	15
B3	0.5	20	80	10
B4	0.5	20	60	10
B5	0.5	10	80	15
B6	0.5	10	60	15
B7	0.5	10	80	10
B8	0.5	10	60	10

Table 2-2: GPCG-1 experimental design

Test #	Conditions			
	Loading (kg)	Initial moisture (%)	Heating temperature (°C)	Flow rate (m^3/h)
A1	3	20	60	40
A2	3	20	80	40
A3	3	20	80	54
A4	4	20	80	40
A5	3	20	100	40
B1	3	10	60	40
B2	3	10	80	40
B3	3	10	80	54
B4	4	10	80	40
B5	3	10	100	40
C1	3	6	80	40
C2	3	6	100	40
C3	3	6	60	40
C4	3	6	80	54
C5	4	6	80	40

Table 2-3:Fitting of MiniGlatt B1 case using different empirical models

	χ^2	Residual sum of squares	R^2
Newton	0.01244	0.13684	0.92147
Page	6.81E-04	0.00681	0.99609
Midilli-Kucuk	7.20E-04	0.00576	0.99669
Ter-term	0.01295	0.10359	0.94055
Two-term Exponential	0.01368	0.13685	0.92147
Verma	0.14673	1.32057	0.24216

Table 2-4: Fitting of drying in MB45 using different empirical models

	χ^2	Residual sum of squares	R^2
Newton	0.00277	0.14661	0.96854
Page	4.76E-04	0.02474	0.99469
Midilli-Kucuk	7.51E-04	0.00376	0.99919
Ter-term	0.00178	0.08918	0.98086
Two-term Exponential	0.00282	0.1467	0.96852
Verma	0.02279	1.16226	0.75061

Table 2-5: Effective diffusivity

	Oven		Fluidized Bed	
Loading (g)	1	5	100	500
D_{eff} (m^2/s)	1.04E-11	2.54E-12	3.46E-12	8.81E-13

Chapter 3 Scale-up of Batch Fluidized Bed

3.1 Introduction

In the pharmaceutical industry, the formulation stage and process development stage are usually carried out in lab-scale or pilot-scale equipment since the cost of pharmaceutical ingredients is usually high. How to be able to scale the process up with minimum trials of experiments becomes a crucial problem. The most commonly described approach in open literature to achieve similarity between two scales of fluidized beds is to match sets of dimensionless numbers [132]. Several scale-up methods have been reviewed in chapter 1. In this chapter, with the understanding of the effect of operating parameters on the required drying time, we will define a dimensionless factor Z based on a mass balance between the solid and gas phase which correlate the operating parameters. Z is designated to predict the drying curves under different operating conditions for different scale fluidized beds based on one existing experimental data that hopefully could reduce the number of trials required for process development.

3.2 Material and Methods

3.2.1 Apparatus

A small-scale MiniGlatt (Glatt Air Tech, Inc) and a medium-scale Glatt GPCG-1 (Glatt Air Tech, Inc) fluidized bed dryer were used in this study. Figure 3-1 shows the design of the two fluidized beds. The smaller size MiniGlatt had a chamber volume of 6 L. The chamber consisted of two parts – a lower conical (d_{min} = 6.6 cm; d_{max} = 14 cm; height = 11cm) and upper cylindrical body (d = 14 cm; height = 12 cm). A nozzle was placed in the upper part of the cylindrical body for preparing wet materials. The larger size Glatt GPCG-1 had a chamber volume of 23 L. The GPCG-1 had a conical body (d_{min} = 15 cm; d_{max} = 30

cm; height = 58 cm). Both fluidized bed dryers operated in a similar way. The hot air flowed into the material chamber from the air inlet below the air distributor. The air distributor covered the whole base of the fluidized bed to provide a uniform air flow throughout the area of the base. The fluidization status of the material could be monitored by visual observation through a glass window on the wall. For both wet and dry materials, no significant difference was observed in terms of the fluidization behavior. The filter bags above the chamber collected small particles and prevented them from escaping the fluidized bed. A backflow air pulse blew back the powder from the filter chambers, so the total mass of the dry material did not change to any appreciable extent.

Several diagnostic devices were used to measure the bed temperature, the exhaust air temperature, and humidity continuously throughout the process. The bed temperature was measured by a K-type thermocouple (OMEGA MWTC). The exhaust air temperature and humidity were measured by means of a hydrometer (HOBO UX100-011). The moisture content of the materials was measured using a moisture analyzer (OHAZ MG45) by loss on drying (LOD).

3.2.2 Materials

The materials investigated is a patented excipient called Fujicalin (Fuji Inc). Fujicalin is a unique dibasic calcium phosphate anhydrous (DCPA). Figure 3-2 shows the SEM image of the solids. The DCPA appears to be a spherical shape. The particle size distribution was characterized by means of the laser diffraction (LS 13 320, Beckham Coulter), and the results are shown in Figure 3-3. The DCPA has a unimodal distribution, and the mean size of the DCPA is 120 microns. The average surface area of the DCPA material is 40 m^2/g (data provided by Fuji Chemical Industries). The pore volume of the DCPA material was

analyzed by the N_2 adsorption and desorption method (TriStar 3000, Micrometrics, USA). The pore volume of the DCPA material was found to be 0.19 cm^3/g. The wet DCPA material used for the tests was prepared by spraying water from the top using the fluidized beds. The water was sprayed through the nozzle until targeted moisture content was reached. Both dry and wet particles fell in the Geldart group A classification.

3.2.3 Operating conditions and procedure

The design of experiments for the tests is given in Table 3-1 and Table 3-2. The effect of loading, initial moisture content, air temperature, and air flow rate were studied in the MiniGlatt and GPCG-1. Before the drying process, the system was preheated. The materials were then loaded and dried. During the experiment, samples were taken every 3 min from the chamber to measure the LOD. Our previous study had shown that the drying process of DCPA in the MiniGlatt and GPCG-1 had excellent reproducibility [117]. For experiments when three consecutive samples were taken, the standard deviation of the measurements was less than 0.58%. Since our initial loading for experiments could be as small as 100 g, each data point was measured only once to prevent taking out more than 10% of the total material in the fluidized bed. Under the same drying conditions, triplicated experiments showed overlapping drying curves. The drying process was stopped when the change in the moisture content of the last three samples was less than 1%.

3.2.4 Scale-up methods

The drying process in the fluidized bed dryers under different operating conditions was correlated using a normalization factor Z (discussed in Section 1), which is defined as the ratio of the required drying time to remove a fixed amount of moisture from the material for two cases under different operating conditions.

$$Z = \frac{\Delta\tau_2}{\Delta\tau_1}$$

Eq. 3-1

In fluidized bed drying processes, the drying temperature, the air flow rate and the initial material loading have a significant effect on the required drying time, and each factor has an independent impact [117, 133]. The scaling rule was initially developed by Reay and Allen [92] and later modified by Kemp and Oakley [94].

Consider a mass balance between the gas and solid phase through a bed height of z to be [4]:

$$\int_{Y_I}^{Y_O} \frac{dY}{Y_{wb} - Y} = f \cdot NTU \int_0^z dz$$

Eq. 3-2

where Y_I and Y_O are the absolute humidity of the drying air coming in and going out respectively, Y_{wb} is the absolute humidity of air at the wet bulb temperature, f is the falling rate factor that describes the drying period with $f = 1$ representing constant rate drying and NTU is the number of transfer units of the drying process.

The evaporative flux per unit bed area, J_{ev}, is given by the following equation [4]:

$$J_{ev} = -\frac{dX}{dt}\frac{m_B}{A_B} = G(Y_o - Y_I)$$

Eq. 3-3

where, X is the moisture content of the materials in the bed, m_B is the bed weight, A_B is the bed area and G is the drying air flux. Over the same increment of moisture content that

uses the temperature difference as the driving force and assumes the drying rate remains constant until hitting the same critical drying point under two initial operating conditions (i.e., similar f), the ratio of the evaporative flux of two sets of conditions gives [4]:

$$\frac{\Delta\tau_2}{\Delta\tau_1} = \frac{\left(\frac{m_b}{A}\right)_2 G_1(T_{GI} - T_{wb})_1(1 - e^{-f \cdot NTU \cdot z})_1}{\left(\frac{m_b}{A}\right)_1 G_2(T_{GI} - T_{wb})_2(1 - e^{-f \cdot NTU \cdot z})_2} = Z$$

Eq. 3-4

We will consider the term "fast-drying" to describe materials where the diffusion of moisture within the porous particle is not rate limiting [4]. For the drying process of fast-drying materials in fluidized bed dryers, the NTU approaches infinity because thermal equilibrium is reached rapidly when the gas is in contact with the solids. The $e^{-f \cdot NTU \cdot z}$ term approaches zero [4], and thus the above equation is reduced to Eq. 3-5.

$$Z = \frac{\left(\frac{m_b}{A}\right)_2 G_1(T_{GI} - T_{wb})_1}{\left(\frac{m_b}{A}\right)_1 G_2(T_{GI} - T_{wb})_2}$$

Eq. 3-5

In Eq. 3-5, increasing the bed depth would reduce the drying rate. The bed weight per unit area, $\frac{m_b}{A}$, was used to represent bed depth as bed depth would vary as the powder is fluidized, expanded, and repacked. An example of where this scaling rule would not be expected to work is drying of wheat where drying is only related to the drying temperature because of the high resistance of moisture diffusion within the solid particles.

With Eq. 3-5, the transformation of a batch drying curve to another drying curve at desired operating condition can be carried out as follows:

1. Obtain X vs. t_1 curve for the base case experimentally.
2. Calculate Z based on the operating conditions from the base and the new cases using $J_{ev}=-\frac{dX}{dt}\frac{m_B}{A_B} = G(Y_o\text{-}Y_I)$
3. Eq. 3-3.
4. Calculate the required time for reaching each moisture content under the new operating conditions using $t_2 = t_1 \cdot Z$.
5. Reconstruct the new drying curve by plotting X vs. t_2.

3.3. Results and discussion

3.3.1 The effect of the initial moisture

The effect of initial moisture content on the drying curve was first studied. The drying air almost reached saturation immediately when it came in contact with the solid phase because the NTU is large in the fluidized bed dryer. Therefore, the driving force due to the drying air humidity change is independent of the initial moisture content. As the initial moisture was not included in the scaling equation (Eq. 3-5), the drying rate should not be affected by the initial moisture content. Figure 3-4 shows the drying curves for MiniGlatt (Figure 3-4a) and GPCG-1 (Figure 3-4b) with different initial moisture contents. For MiniGlatt, 500 g of dry powder was dried at 60 °C with 18 m^3/h air flow rate. Three levels of initial moisture content were investigated (40 %, 25 %, and 10 %). The drying rate of the process during the constant rate period can be obtained by fitting the linear part of the drying curve. The drying rate for the 10 %, 25 %, and 40 % cases were 0.64 %/min, 0.75 %/min and 0.84 %/min, respectively. For GPCG-1, 3 kg dry powder was dried at 80 °C with 54 m^3/h air flow rate. The initial moisture content of 6 %, 10 %, and 20 % was investigated. The drying rate for the 6 %, 10 %, and 20 % cases were 0.25 %/min, 0.25 %/min and 0.22 %/min, respectively.

In all cases shown in Figure 3-4a and Figure 3-4b, the drying process remained in unhindered drying period until the moisture content dropped below 1 %. For MiniGlatt, the initial moisture content did not affect the drying rate significantly as the drying rate increased by 0.2 %/min when the initial moisture was increased from 10 % to 40 %. A similar discovery was found for GPCG-1, the drying rate decreased by 0.03 % as the initial moisture increased from 6 % to 20 %. The inconsistent change of drying rate may be due to the experimental error. When operating at the same air temperature, air flux, and loading, drying rate is independent of initial moisture content. The results indicate that the drying curve for higher initial moisture content can be recreated using the drying curve from the low initial moisture content case by applying the same drying rate, and vice versa.

3.3.2 The effect of the air temperature

During the fluidized bed drying process, the low air humidity and the long drying time at high temperature could cause process-induced transformation (PIT) of the APIs [134, 135]. For example, over drying a monohydrate can result in the formation of a dehydrated monohydrate and other anhydrous crystalline forms[136]. Being able to reconstruct the drying curve under different air temperature enables us to determine the time it takes for a phase transformation to occur under such operating conditions. The design of the drying process could then be adjusted before committing significant resources at commercial scale.

Figure 3-5 shows the drying curve prediction based on the drying temperature: panel a and b were obtained from MiniGlatt runs with 800 g of loading, 20 % initial moisture, and 14 m^3/h, panel c and d were obtained from GPCG-1 runs with 3 kg of loading, 20 % initial moisture and 40 m^3/h. Since the loading and the air flow were kept unchanged when the temperature increased,

Eq. 3-2 then reduced to:

$$Z = \frac{(T_{GI} - T_{wb})_1}{(T_{GI} - T_{wb})_2}$$

Eq. 3-6

where the gas inlet temperature T_{GI} represents the final equilibrium bed temperature, and the wet bulb temperature T_{wb} is the bed temperature during the constant rate period. Both T_{GI} and T_{wb} can be obtained from Figure 3-5a and Figure 3-5b. Increasing the air temperature increases the temperature difference between the solid and gas phase, thus the drying force for heat transfer increases. The grey curves in Figure 3-5c and Figure 3-5d were predicted based on the drying data from lower temperature cases (60 °C case for MiniGlatt and 80 °C case for GPCG-1) using Eq 6. The prediction shows good agreement for both MiniGlatt and GPCG-1.

3.3.3 The effect of the air flux

During the drying process, the air flux determines the amount of liquid that the drying medium is able to remove from the solid. Figure 3-6 shows the drying curves for MiniGlatt and GPCG-1 obtained under different air flow. Two levels of air flow were investigated with all other operating conditions kept the same: Figure 3-6a was obtained from MiniGlatt runs at 14 m^3/h and 18 m^3/h (250 g of loading, 40% initial moisture and 60 °C). The blue line represents the prediction of the 18 m^3/h case by applying the scaling

Eq. 3-2 to the experiment 14 m^3/h curve. Figure 3-6b was obtained from GPCG-1 runs at 40 m^3/h and 54 m^3/h (3 kg of loading, 20% initial moisture and 80 °C). The blue line represents the prediction of the 54 m^3/h case by applying the scaling

Eq. 3-2 to the experiment 40 m^3/h curve. Since the airflow is the only changing variable in this case,

Eq. 3-2 is then reduced to:

$$Z = \frac{G_1}{G_2}$$

Eq. 3-7

The predictions have a good agreement with the experimental data because the system is heat transfer limited, i.e., the drying process is limited by the heat supply from the air, which is reflected by the fact that most of the drying occurred under the constant rate period. Therefore, increasing the flow of the hot air will instantly enhance the heat input. According to Eq. 3-7, the drying rate is proportional to the air flow.

3.3.4 The effect of the loading

Figure 3-7 shows the drying curves for MiniGlatt and GPCG-1 obtained under different air flow. Figure 3-7a was obtained from MiniGlatt runs with 100g, 250g, 500g, and 800g of loading (14 m^3/h air flow, 40% initial moisture and 60°C). The lines represent the prediction of the 250g, 500g and 800g cases by applying the scaling Eq. 3-2 to the experiment 100g curve. Figure 3-6b was obtained from GPCG-1 runs at 2 kg, 3 kg and 4 kg (54 m^3/h air flow, 20% initial moisture and 80 °C). The lines represent the prediction of the 3 kg and 4 kg cases by applying the scaling Eq. 3-2 to the 2 kg experimental curve. Since the loading is the only changing variable, in this case, Eq. 3-2 is then reduced to:

$$Z = \frac{\left(\frac{m_b}{A}\right)_2}{\left(\frac{m_b}{A}\right)_1}$$

Eq. 3-8

The bed area initially used for the calculation was the average area over the volume occupied by the materials. For the MiniGlatt, the predicted drying curves (see Figure 3-7a) had over-predicted drying rates. The predictions of the drying rate were over-predicted by about 36 %, 93 %, and 153 %, for the 250 g, 500 g, and 800 g cases, respectively. The predictions had better agreement with the experimental data for the GPCG-1 (see Figure 3-7b). The predictions of the drying rate were over-predicted by about 7 %, and 13 %, for the 3 kg and 4 kg cases, respectively. A possible reason for the discrepancy between predictions and experiments was that the area used for Eq. 3-5 was being overestimated. Several studies showed that although the air and the particles interact throughout the entire volume of the chamber, most of the drying occurs in the space immediately above the air distributor due to the excellent heat transfer in fluidized beds [94, 137]. Therefore, the area of the distributor represents the relevant area where the drying is taken place and should be used as the bed area for the calculation in Eq. 3-5.

Figure 3-8 shows the prediction after the air distributor area was used for the MiniGlatt (Figure 3-8a) and GPCG-1 (Figure 3-8b). For MiniGlatt, the prediction for 250 g based on the 100 g drying curve overlaps with the 250 g experimental data. The predictions of the drying rate were overestimated by about 13 % and 27 % for the 500 g and 800 g cases. The predictions for GPCG-1 were also improved – the prediction for 3 kg from 2 kg drying curve now agreed with the experimental data; the prediction of the drying rate for 4 kg from 2 kg drying curve was now underestimated by about 8 %. Using the area of the air distributor for the calculation apparently gave a better prediction.

To further understand the effect of loading in the scaling prediction, the predictions in MiniGlatt for 100 g, 250 g, and 800 g based on the 500 g experimental data were also investigated, and the results are shown in Figure 3-9. The prediction for 800 g had an excellent agreement with the experimental drying curve. The predictions of the drying rate were overestimated by about 13 % and 10 % for the 100 g and 250 g cases. The results showed that the scaling rules gave a better prediction for the 250 g case when predicting from the 100 g drying curve and better prediction for the 800 g case when predicting from the 500 g drying curve. It should be noted that 250 g of particles fill the lower conical part of the MiniGlatt while 500 g of particles fill the lower part and some of the upper cylindrical part (see Figure 3-1a). Therefore, the scaling rule worked well with both lower loadings (100 g and 250 g) and higher loadings (500 g and 800 g), respectively. However, as the geometry is changed when predicting from lower loadings to higher loadings, the scaling rule has to be further modified to include the changes in the fluidization and the mixing due to the geometry change.

Figure 3-10 shows a summary of $Z_{prediction}$ vs. $Z_{observation}$. $Z_{observation}$ was the ratio of the required drying time for each case over the shortest required drying time. $Z_{prediction}$ was calculated by using the case that has the shortest drying time as the base case and then applying Eq. 3-2 to each case. For MiniGlatt, the two data points circled out are 20% initial moisture cases, the rest are from 40% initial moisture cases. The predictions are in good agreement with the experimental observations until Z reaches 2.5. In the middle range (Z = 3 - 5), the two circled out points from 20 % initial moisture cases have higher prediction than the experimental observation. It suggests that larger error may occur when scaling between different initial moisture contents. As Z approaches a value greater than 5, the

scaling equation tends to underestimate the normalization factor and therefore will predict less drying time. For GPCG-1, Z ranges from 1 to 2 for all cases, and the predictions are in good agreement with the experimental observations.

3.3.5 Scaling from MiniGlatt to GPCG-1, and to GPCG-2

To test whether the model can be used for scaling-up, the drying curves obtained from the MiniGlatt, GPCG-1 and GPCG-2 were compared. Figure 3-11 represents the results of the scale-up attempt from the MiniGlatt to the GPCG-1. The blue line shows the prediction of the GPCG-1 drying curve based on the MiniGlatt experimental data. In this case, the initial moisture content and the drying temperature were kept the same. Both the drying experiment in the MiniGlatt and GPCG-1 were carried out with 20 % initial moisture content and 80°C air temperature. The MiniGlatt was loaded with 800 g of materials, and the GPCG-1 was loaded with 2 kg of materials. The air flow for the MiniGlatt and GPCG-1 were 18 m^3/h and 40 m^3/h, respectively. The drying curve prediction showed a good agreement with the experimental data. Similar results were also found when scaling from a 500 g loading in the MiniGlatt to a 3kg loading in the GPCG-1 (not shown).

Figure 3-12 shows drying of DCPA with 20 % initial moisture content at 60°C. The air flow rates used for the MiniGlatt and GPCG-1 were 14 m^3/h and 40 m^3/h respectively. The blue curve represents the prediction of the GPCG-1 drying curve based on the MiniGlatt drying experimental data. The GPCG-1 prediction did not agree as well with the experimental data as in the previous case (see Figure 3-11) but was able to match the basic shape of the experimental GPCG-1 drying curve.

Figure 3-13 represents the results of the scale-up attempt from the MiniGlatt to the GPCG-2. The lines show the prediction of the GPCG-2 drying curve based on the MiniGlatt

experimental data from different loadings. It was found that predictions from 100 g and 250 g had good agreement with GPCG-2 experimental data. However, the predictions from 500 g and 800 g overestimated the required drying time by about 5 min.

3.4. Conclusion

Fluidized bed drying of a pharmaceutical excipient was carried out in a small-scale unit (MiniGlatt) and a medium-scale unit (GPCG-1). A scaling equation was used to predict the drying curve under different operating conditions (initial moisture content, air flow, air temperature and loading) based on the existing experimental data. Based on the results, we made the following conclusions:

1. During the constant rate period, the drying rate depended on the air flow rate, air temperature, and the initial loading. The initial moisture did not have a significant effect on the drying rate.
2. For both MiniGlatt and GPCG-1, the drying curve predictions had a good agreement with the experimental data when scaling by the air temperature and air flow rate
3. While scaling the loading, our results supported that the air distributor area should be used for the calculation because the drying process occurs mostly near the air distributor. For the MiniGlatt, the scaling rule worked well for scaling between lower loading cases (100 g and 250 g) and higher loading cases (500 g and 800 g). The model overpredicted the drying rate when scaling from low loadings to high loadings. We hypothesized that this is because of the material chamber geometry change.

4. The model predictions had good agreement with the experimental observations at low Z (1-2.5). At higher Z (>3), the model tended to not agree as well with the experimental data.
5. The model was able to provide a scale-up prediction for the GPCG-1 using experimental data from MiniGlatt.

This work gave an experimental validation for the previously proposed scaling rule from Kemp et al. [94]. Based on the results shown in this chapter, this method worked fairly well while scaling up from a small lab-scale unit (MiniGlatt) to a medium lab-scale unit (GPCG-1). At the same time, our results had been obtained from a limited number of drying conditions, two pieces of equipment and only one material. The material that had been discussed in this chapter is a Group A powder with a unimodal particle size distribution. The drying process of this material was dominated by the unhindered drying period. Issues may be caused when applying the proposed model to new material because 1) the fluidization pattern may change if the material falls in a different Geldart group category which in turn affect the heat and mass transfer and 2) the internal porous structure may be different resulting in a hindered period dominated drying profile. Therefore, further work is needed to see if the results we have obtained here can be generalized to other materials and drying conditions. It would also be of interest to examine other fluidized bed dryers to see how equipment changes might affect the drying process. In addition, further work is needed to examine this method while scaling to a larger pilot scale and commercial scale. This is only a start for fluidized bed dryer scaling. We hope that the results discussed in this chapter would be a good foundation for future work in this area.

3.5 Notation

Notation

A	bed area, m^2
a	surface per unit volume per unit volume, m^2/ m^3
d	diameter, cm
f	falling-rate drying factor, -
G	volumetric velocity of gas, m^3/h
J	mass flux, kg/m^2h
m	mass loading, kg
NTU	number of transfer units, -
T	temperature, °C
t	time, min
Y	Absolute humidity (mixing ratio) of gas (dry basis) (kg/kg)
Z	normalization factor, -

Greek Letters

τ	required drying time (min)

Subscripts and Superscripts

1	reference case
2	target case
b	for bed of material
ev	for evaporation
I	at inlet
O	at outlet
wb	at wet bulb conditions

3.6 Figures for Chapter 3

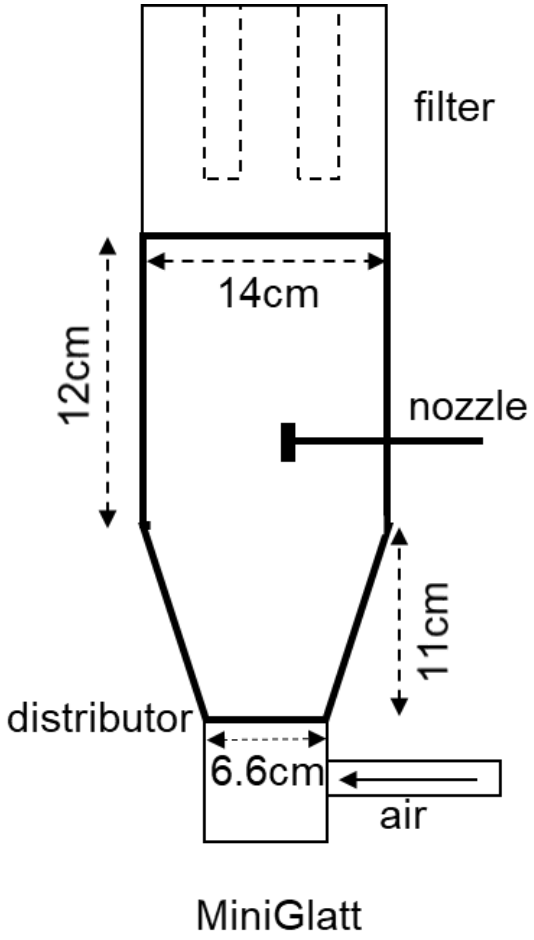

MiniGlatt

(a)

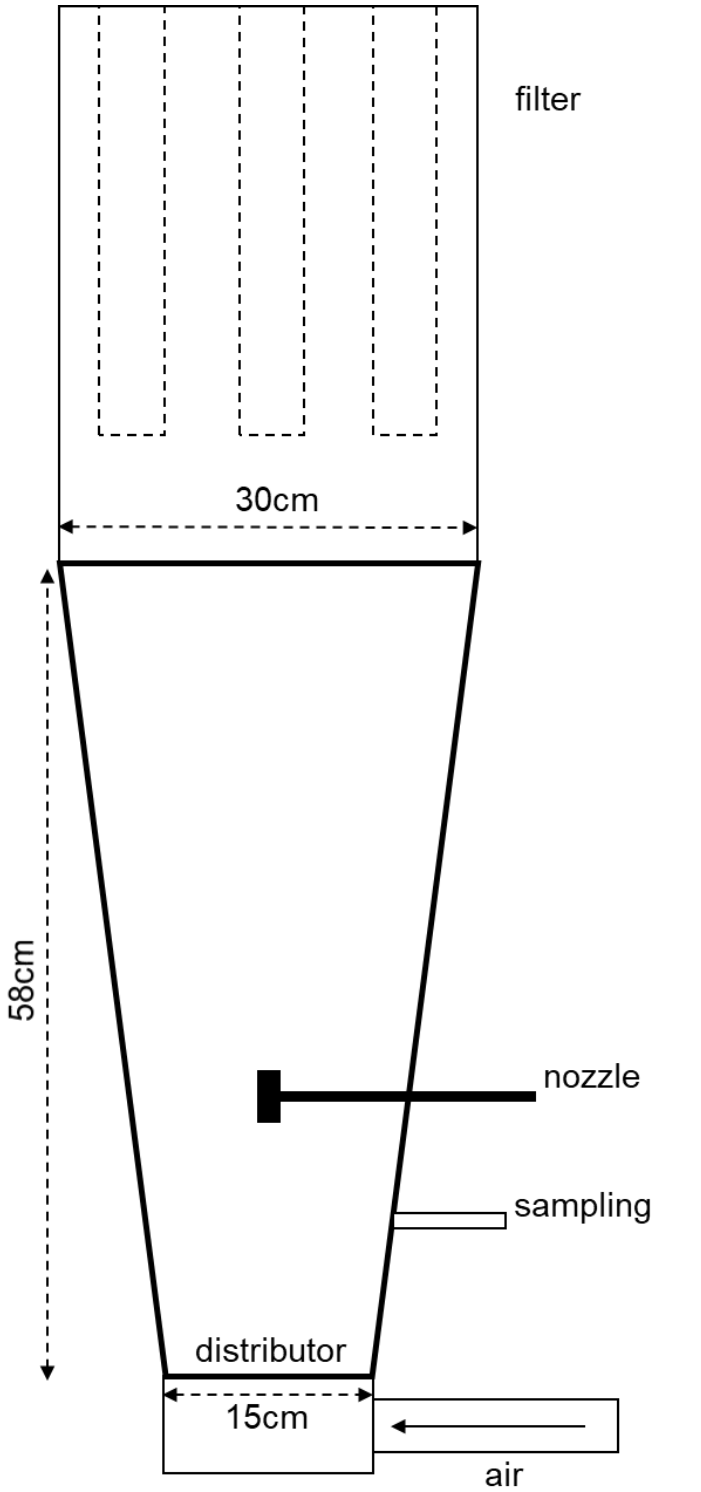
filter
30cm
58cm
nozzle
sampling
distributor
15cm
air
GPCG-1

(b)

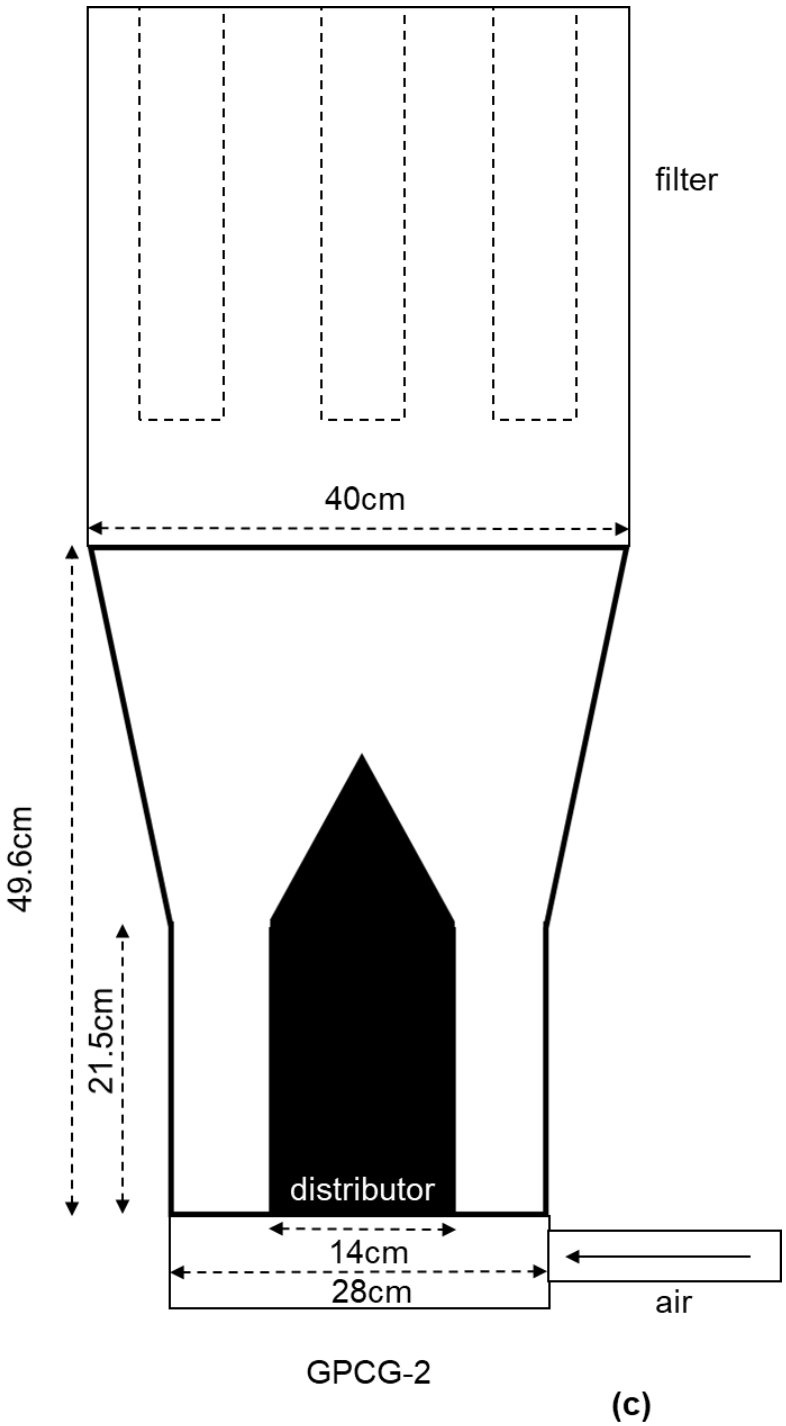

Figure 3-1: Schematics of a) MiniGlatt and b) Glatt GCPG-1 fluidized bed dryers.

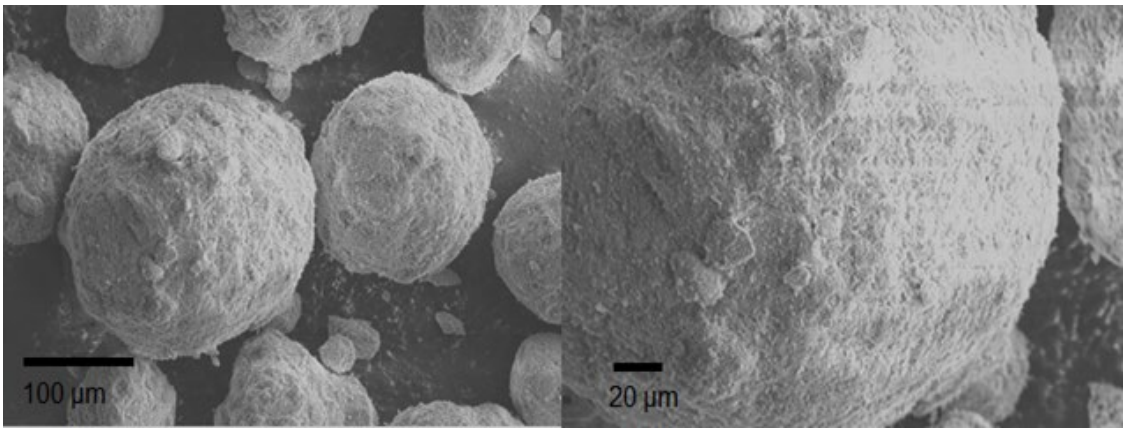

Figure 3-2: SEM images of dibasic calcium phosphate anhydrous (DCPA).

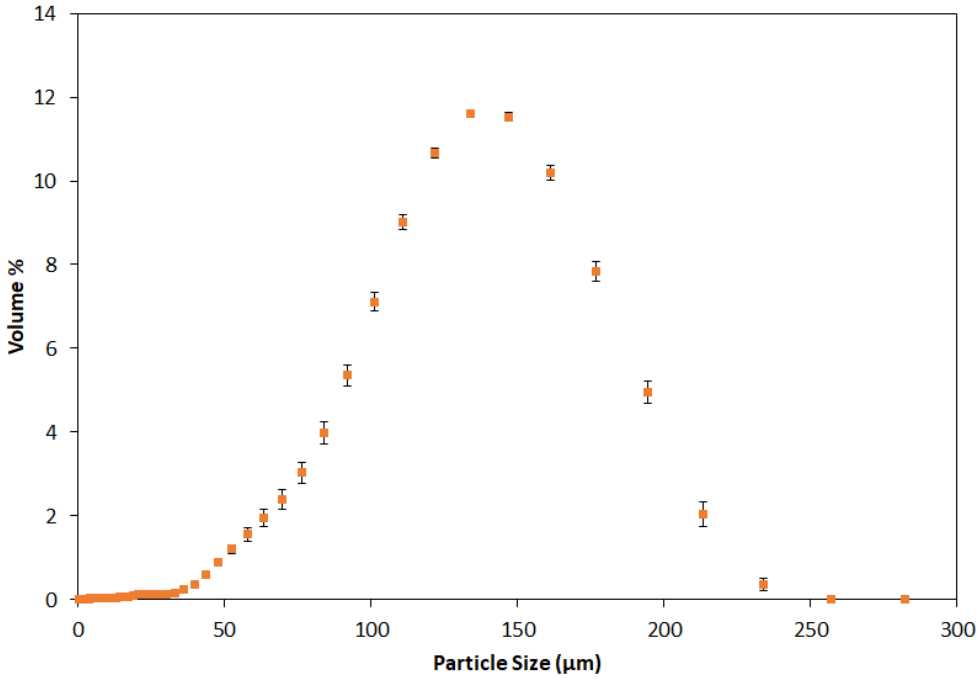

Figure 3-3: Particle size distribution of dibasic calcium phosphate anhydrous (DCPA).

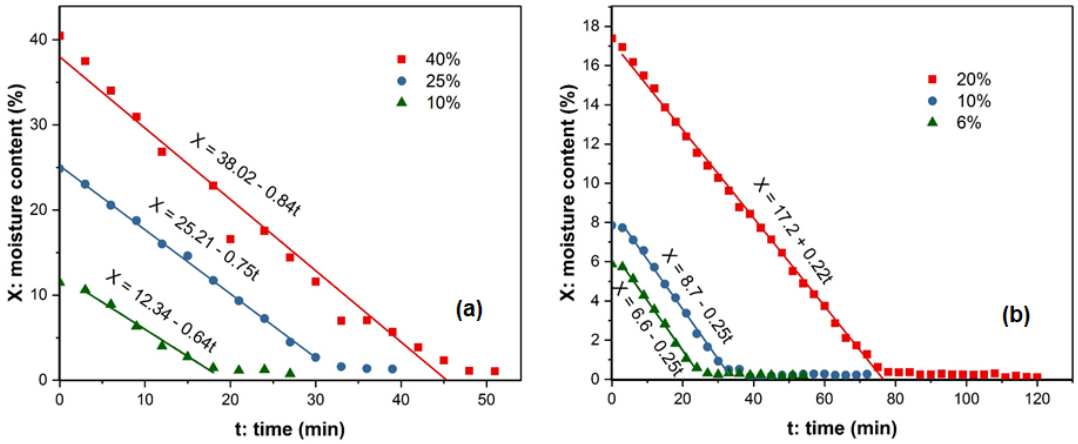

Figure 3-4: Drying curves of a) MiniGlatt (T = 60 °C, air flow rate= 18 m^3/h, loading = 3 kg) at different initial moisture content 10%, 25% and 40%; and b) GPCG-1 (T = 80 °C, air flow rate= 54 m^3/h, loading = 3 kg) at different initial moisture content 6%, 10% and 18%.

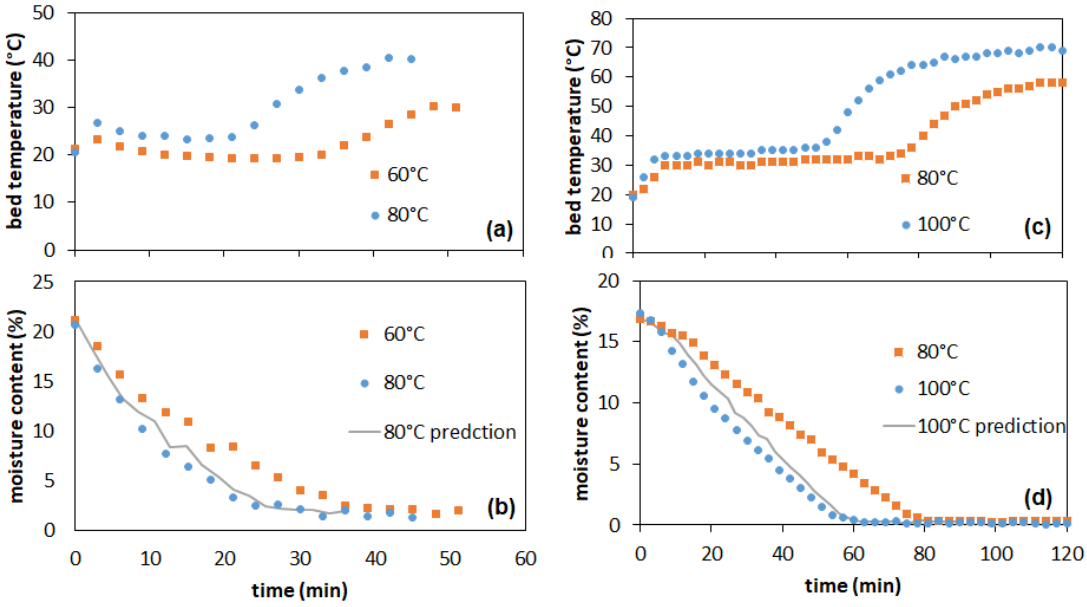

Figure 3-5: Drying DCPA using MiniGlatt (air flow rate= 14 m^3/h, loading = 800 g, initial moisture content 20%) a) bed temperature profile and b) drying curve; and using GPCG-1 (air flow rate= 40 m^3/h, loading = 3 kg, initial moisture content 18%) c) bed temperature profile and d) drying curve.

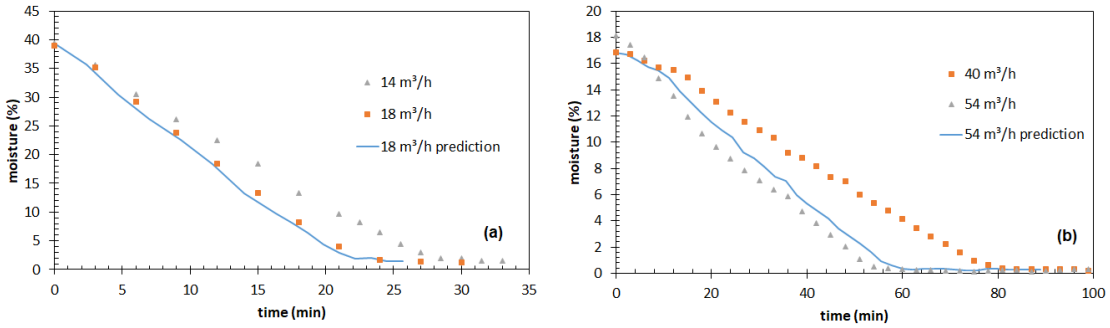

Figure 3-6: Drying curves of a) MiniGlatt (T = 60 °C, loading = 250 g, initial moisture content 40%) and b) GPCG-1 (T = 80 °C, loading = 3 kg, initial moisture content 18%).

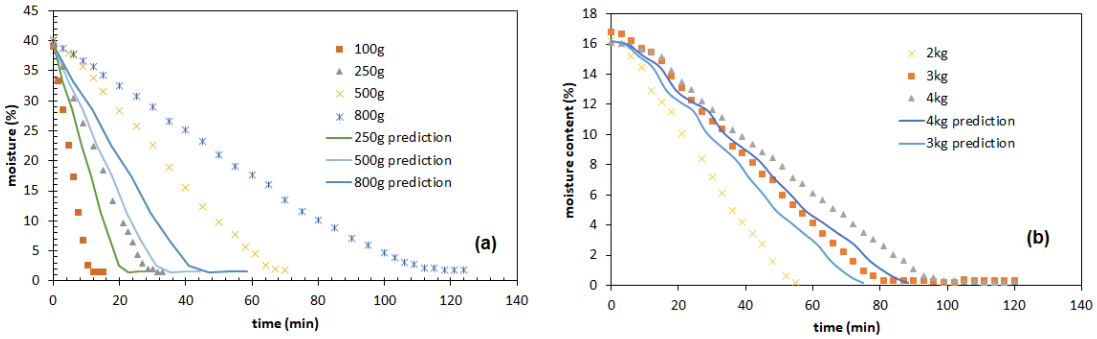

Figure 3-7: Drying curves of a) MiniGlatt (T = 60 °C, air flow rate= 14 m^3/h, initial moisture content 40%) and b) GPCG-1 (T = 80 °C, air flow rate= 54 m^3/h, initial moisture content 18%) .

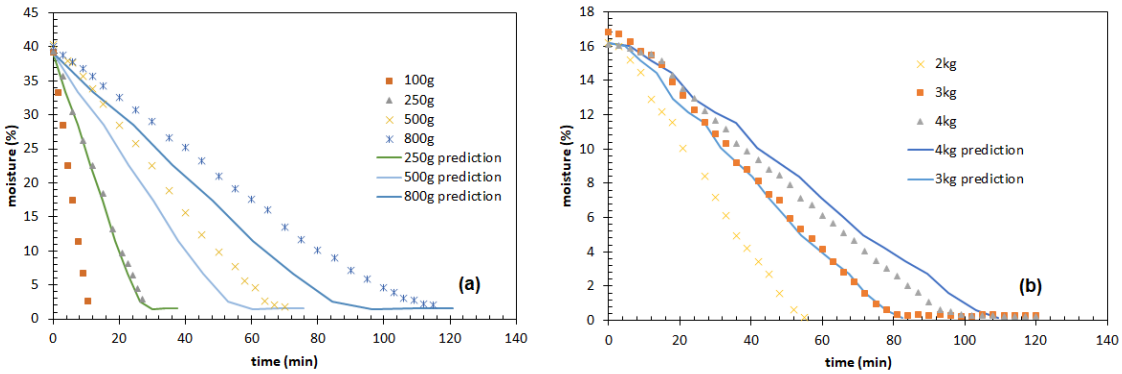

Figure 3-8: Drying curve predictions after using air distributor area for calculation a) MiniGlatt and b) GPCG-1.

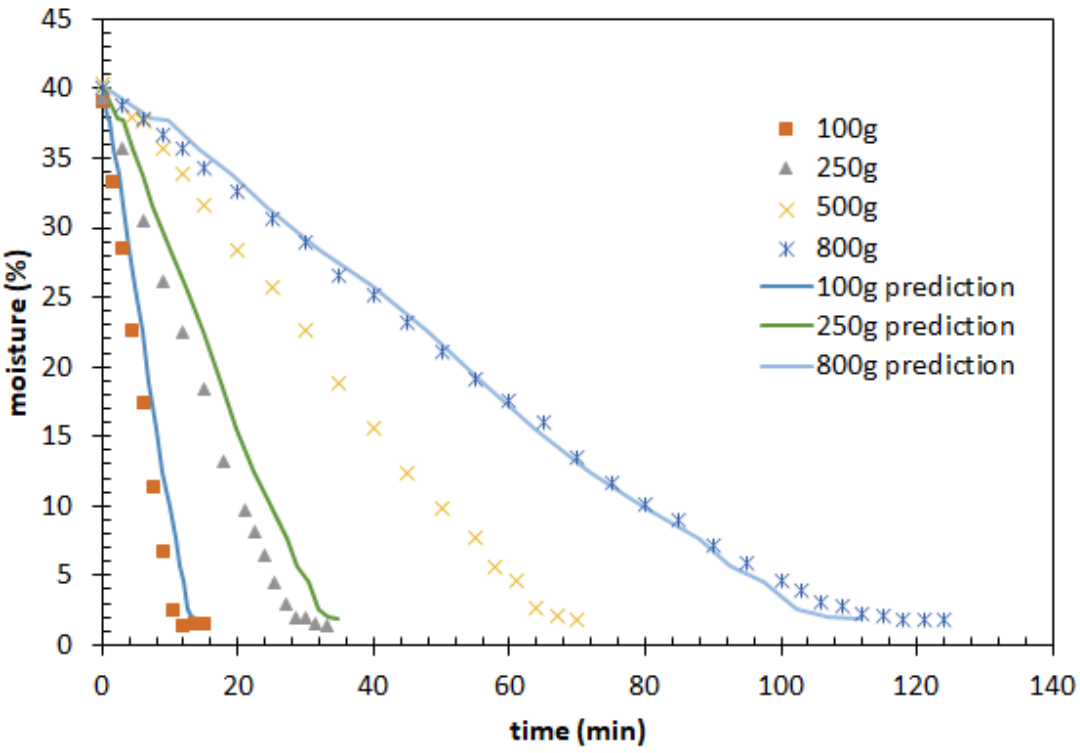

Figure 3-9: Drying curve predictions of MiniGlatt based on the loading of 500 g.

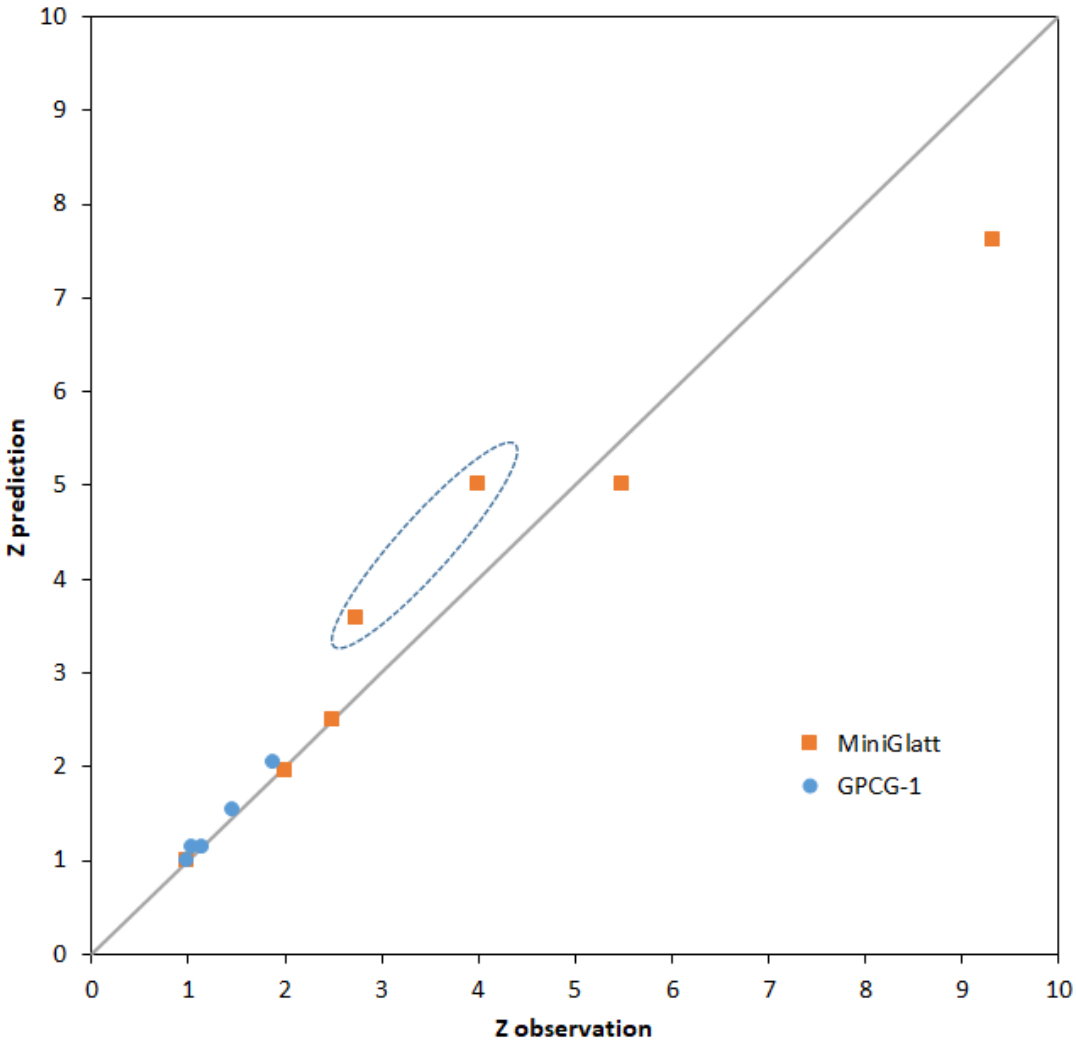

Figure 3-10: Zprediction vs. Zobservation for MiniGlatt and GPCG-1.

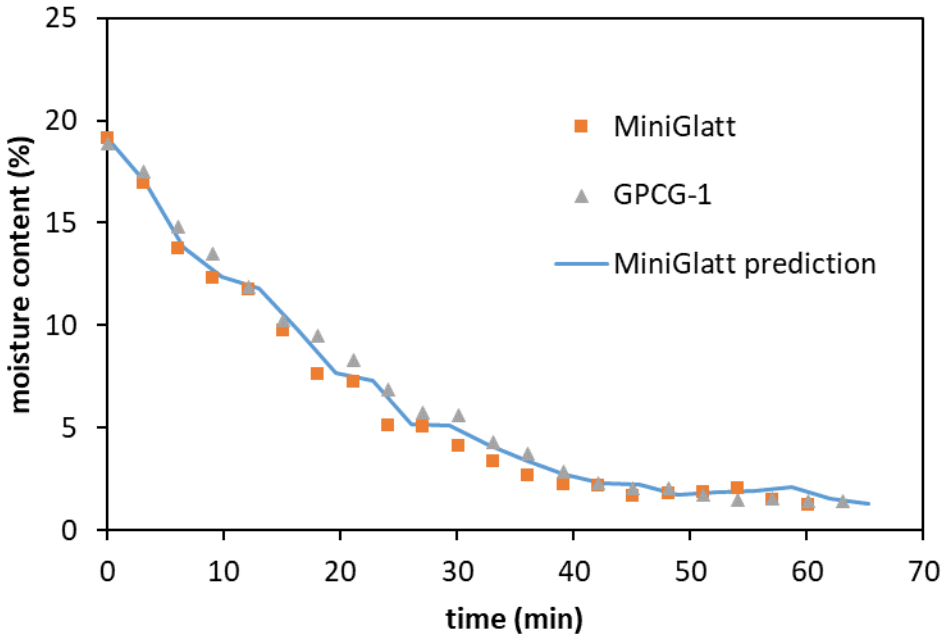

Figure 3-11: Prediction of GPCG-1 (T = 80 °C, air flow rate= 40 m^3/h, loading = 2 kg, initial moisture content 20%) based on MiniGlatt (T = 80 °C, air flow rate= 18 m^3/h, loading = 800 g, initial moisture content 20%).

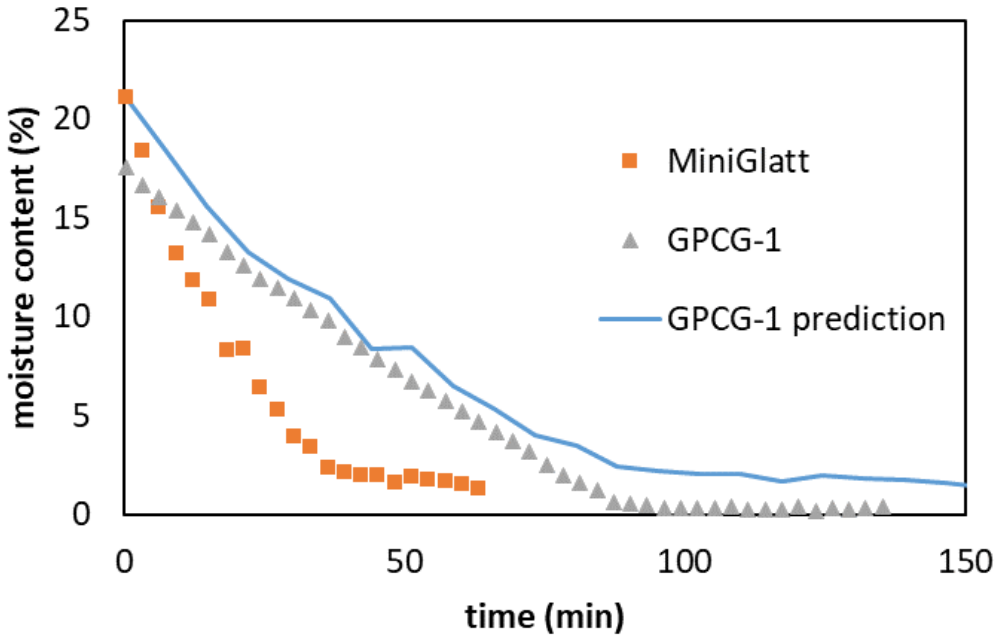

Figure 3-12: Prediction of GPCG-1 (T = 80 °C, air flow rate= 40 m^3/h, loading = 2 kg, initial moisture content 20%) based on MiniGlatt (T = 80 °C, air flow rate= 18 m^3/h, loading = 800 g, initial moisture content 20%).

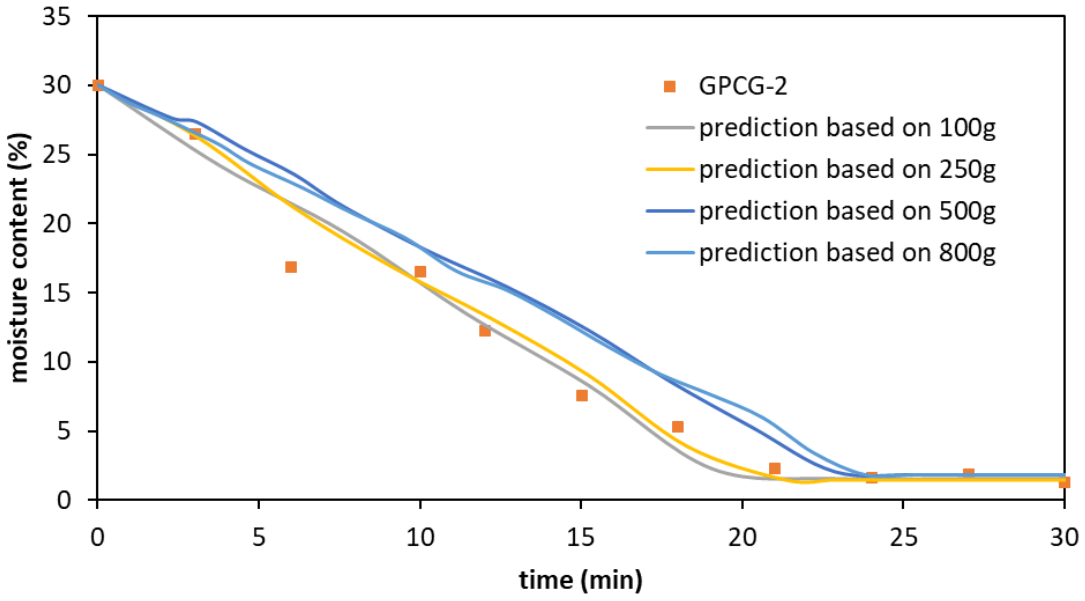

Figure 3-13: Prediction of GPCG-2 (T = 80 °C, air flow rate= 90 m^3/h, loading = 3 kg, initial moisture content 30%) based on MiniGlatt (T = 80 °C, air flow rate= 18 m^3/h, initial moisture content 20%) with different initial loadings.

3.7 Tables for Chapter 3

Table 3-1: MiniGlatt experimental design

Loading (kg)	Initial Moisture Content (%)	Heating Temperature (°C)	Flow Rate (m^3/h)
0.50	20	60	14
0.50	20	80	14
0.25	40	60	18
0.25	40	60	14
0.10	40	60	14
0.50	40	60	14
0.80	40	60	14

Table 3-2: GPCG-1 experimental design

Loading (kg)	Initial Moisture (%)	Heating Temperature (°C)	Flow Rate (m^3/h)
3.0	20	80	40
3.0	20	100	40
3.0	20	80	54
4.0	20	80	40
2.0	20	80	40

Chapter 4 : Continuous Fluidized Bed Drying – Moisture Content

4.1. Introduction

In this chapter, experiments were set up to study the effect of the critical process parameters on the residence time distribution of a continuous fluidized bed dryer. The effluent moisture content will be predicted based on the drying kinetics and the hydrodynamics of the material during the fluidized bed drying process. This chapter aims to present a method of characterizing a continuous fluid bed drying process that, hopefully, can be migrated to other continuous pharmaceutical drug product processes development.

4.2. Materials and Method

4.2.1 Materials

The material used for the study is Fujicalin – a dibasic calcium phosphate anhydrous (DCPA) purchased from Fuji Chemical Industries (USA). DCPA is a common excipient in pharmaceutical manufacturing. The particle size distribution was characterized using laser diffraction (model LS 13 320, Beckham Coulter). The DCPA used in this study has a unimodal distribution size. The average diameter of DCPA is 120 micron. The flowability of the DCPA powder was measured by running shear tests at 3 kPa using the FT4 powder rheometer (Freeman Technology, USA). Nigrosin water-soluble dye was purchased from Sigma-Aldrich (Darmstadt, Germany) to prepare the colored tracer powder.

4.2.2 Description of the Glatt GPCG-2 system

Drying experiments were performed on a Glatt GPCG-2 system (Glatt Air Techniques Inc., Ramsey, NJ, USA). The continuous line includes a loss-in-weight feeder (model KT20 from Coperion GmbH) (see Figure 4-1), two rotary valves (see Figure 4-2), and a Glatt GPCG-2 fluidized bed dryer (see Figure 4-3). The units are connected vertically as shown in Figure 4-4. The GPCG-2 fluidized bed dryer has an inlet port and an outlet port on the product chamber to allow continuous operation. Figure 4-5. shows a top view (Figure 4-5a)

and side view (Figure 4-5b) of the product chamber. The product chamber is divided into four segments as shown in Figure 4-6. The inlet port is on the wall of segment I, and the exit port is on the wall of segment IV. Small gaps are left between the bottom of the segments II and III to allow particle movement from one segment to another.

Before the process started, the product chamber was prefilled with a certain amount of materials (initial loading). The system was thus first to run as a batch process. The materials were then fed using the KT20 feeder. Upon reaching steady state, the powders were pushed forward in a counter clock-wise motion at a constant mass flow rate (Figure 4-6a top view) from segment I to II to III to IV. The rotary valves helped to seal the fluidized bed system and ensure the material flow was steady. Samples were taken from the effluent stream to measure the moisture content and the tracer concentration. Taking the samples disturbed the mass flow measurement, which in turn disturbed the control of the mass flow rate. Therefore, with the time scale of most our experiments around 60 min (three mean residence times), samples were taken every 3 min to ensure enough data points without large fluctuations in the mass flow rate.

4.2.3 Method

The ultimate goal of this study is to develop a method to predict the moisture content of the continuous fluidized bed – one of the CQAs. The GPCG-2 continuous fluidized bed has been characterized by RTD models and drying kinetic models which have been combined to predict the effluent moisture content as shown in Figure 4-7.

The drying process in the continuous fluidized bed has been treated as a chemical reaction process. The flowing and mixing of the solid particles has been characterized using the RTD data and the RTD model.

4.2.3.1 Drying Kinetics

Drying of porous solid particles usually contains three periods: the pre-heating period, the unhindered or constant rate period, and hindered or falling rate period. During the pre-heating period, the heat absorbed by the particles is mainly used to heat up the particles and the surrounding environment. The fluidized bed was warmed up prior to all experiments by flushing in heating gas into the empty product chamber to reduce the pre-heating period and thus decrease the time for the bed to reach steady state. During the unhindered period is reached, the amount of heat transferred to the solid is equal to the amount of liquid vaporized multiplied by the latent heat of vaporization. During the unhindered period, the wet particles keep supplying liquid to the surface, and the drying front recedes towards the center. Finally, in the hindered period, the supply of liquid to the surface is insufficient to maintain a sufficiently wetted surface, and thus the drying rate starts to fall [138-140].

The following assumption is made: the continuous fluidized bed drying process has the same drying kinetics for a single particle as in a batch fluidized bed when the loading, air temperature, and airflow are the same. For simplicity, the drying curves obtained from the batch drying experiments were fitted with an empirical model proposed by Midilli et al. [74]:

$$C_A = a\ exp(-kt^n) + bt$$

Eq. 4-1

where C_A is the moisture concentration of the particles, t is the time, and a, k, n, and b are coefficients used to fit the model.

4.2.3.2 Residence Time Distribution

4.2.3.2.1 Basics of RTD

The RTD reflects the time each portion of material spends in the reactor/process. It can be obtained for a unit operation with a tracer response experiment [141]. Traditionally, either a pulse or a step change of tracer is added to the inlet of the unit operation, and the response of the tracer concentration profile is measured at the exit. Pulse tests were conducted in this study. During a pulse test, an amount of the tracer (N_0) was suddenly introduced into the inlet. At the exit, the amount of tracer coming out (ΔN) over a small increment of time Δt was measured. The residence time distribution function $E(t)$ has been defined as the rate of the total percentage of tracer leaving the reactor as a function of time:

$$E(t) = \frac{\Delta N/\Delta t}{N_0} = \frac{vC(t)}{N_0}$$

Eq. 4-2

where v is the mass flow of the material and C is the concentration of tracer in the effluent stream. $E(t)$ has units of time^{-1}.

It is desirable to obtain the full concentration profile including the entire tail of the curve in order to achieve an accurate RTD. In practice, where a complete tail may not be achievable, extrapolating the tail by fitting an exponential decay may improve the accuracy.

Integrating the RTD as a function of time gives the cumulative distribution function $F(t)$:

$$F(t) = \int_0^t E(t)\,dt$$

Eq. 4-3

The cumulative distribution function represents the fraction of effluent that has been in the reactor for less than time, *t*.

From the RTD, the average time that all tracers spend in the reactor is:

$$t_m = \frac{\int_0^\infty tE(t)dt}{\int_0^\infty E(t)dt}$$

Eq. 4-4

Instead of comparing the whole curve of several RTDs, variance and skewness are usually compared and are defined in the following equations, respectively:

$$\sigma^2 = \int_0^\infty (t - t_m)^2 E(t)dt$$

Eq. 4-5

$$s^3 = \frac{1}{\sigma^{3/2}} \int_0^\infty (t - t_m)^2 E(t)\, dt$$

Eq. 4-6

A dimensionless number, the Peclet number (Pe), is used to characterize the continuous fluidized bed behavior. Pe is defined as:

$$Pe = \frac{\text{Rate of transport by convection}}{\text{Rate of transport by dispersion}} = \frac{UL}{D}$$

Eq. 4-7

where U is the superficial velocity of the particles, L is the characteristic length of the fluidized bed, and D is the dispersion coefficient. Pe can be measured experimentally from the following equation:

$$\frac{\sigma^2}{{t_m}^2} = \frac{2}{Pe} - \frac{2}{Pe^2}(1 - e^{-Pe})$$

Eq. 4-8

To investigate the effect of the critical process parameter on the RTD, a 2-level factorial design was adopted in this study as shown in Table 4-1.

4.2.3.2.2 Tracer Preparation

In order to carry out a successful pulse response experiment, the tracer material must be similar to the particles of interest to provide a representative RTD. In this study, the tracer material was prepared by coating nigrosin onto the DCPA via the top spraying technique in a Glatt GPCG-1 batch fluidized bed. The nigrosin water solution was prepared at its maximum water solubility (10 mg/mL). The solution was sprayed into a fluidized DCPA powder bed at room temperature to reach 40 wt% of the dry solids. After the top spraying, the DCPA was dried in the fluidized bed to provide dry tracer powders. Figure 4-8a shows the DCPA particles before and after coating treatment. The tracer particles (DCPA + nigrosin) obtained a black color due to the nigrosin solution. The tracer powder was then mixed with different amounts of the original white DCPA powder (see Figure 4-8b) for calibration curve development.

4.2.3.2.3 Develop a Calibration Model for Tracer Concentration Measurement

The amount of tracer was measured using an X-Rite VeriColor Spectro 450 color spectrometer (X-Rite, Grand Rapids, MI, USA) offline as shown in Figure 4-9, and a Matrix F FT-NIR spectrometer (Bruker Optics, Billerica, MA, USA) online as shown in Figure 4-10.

The colorimeter shines a light on a sample and measures the reflectance as a function of wavelength. A calibration curve was required to correlate the color reflectance and the tracer concentration of the sample. The calibration method we have used in this study was employed by Emady et al. [142]. Tracer concentrations ranging from 0% to 20% (wt. %)

with 1% intervals were prepared. Data taken from a single wavelength (410 nm) were plotted as functions of the concentration of tracer (see Figure 4-11). The wavelength of 410 nm was chosen because it gave the lowest standard deviation across each set of samples. A 4^{th} order polynomial equation was used to fit the calibration curve (see curve labeled "Poly." in Figure 4-11).

The FT-NIR spectrometer was used to collect NIR spectra from the calibration sample offline with the setup shown in Figure 4-12. In this case,tracer concentrations ranging from 0% to 15% with 3% intervals (wt. %) were prepared. The sample powders were fed onto a belt through a funnel by a vibrating feeder. The NIR probe was placed 8cm above the sample. About 36 scans were obtained for each concentration. During the online measurement for the continuous fluidized bed drying process, the setup for the NIR probe is similar to that for the calibration setup (see Figure 4-13). NIR spectra were obtained approximately every 7s. NIR spectral preprocessing, Principal Component Analysis (PCA) and Partial Least Squares (PLS) regression models were developed with The Unscrambler 10.5 (CAMO Software AS., Oslo, Norway).

Figure 4-14 shows the PCA score plot of the NIR spectra for calibration blends using multiplicative scatter correction (MSC) method for spectral preprocessing. MSC is typically used to compensate for additive and/or multiplicative scatter effects in spectral data. The spectra after preprocessing are shown in Figure 4-15. The spectra difference can be observed for different tracer concentration within the 8100-5500 cm^{-1} range. Other preprocessing methods were also tried. Standard normal variate (SNV) gave similar results to the MSC method (data not shown). Taking the derivatives can correct for baseline effects in spectra, but in this case, resulted in non-convergence for PCA. The explained variance

is 87% in the first principal component and 1% in the second principal component. The samples were distributed by the concentration level of tracer along PC-1. The 12% and 15% sample data points have some overlay on the plot showing the risk of inaccurate measurement of tracer concentration in that range. Fortunately, during the RTD pulse experiment, the peak of the tracer concentration is below 12%.

4.3. Results and Discussion

4.3.1 Validation of the Tracer Experiment

In tracer response tests, it was necessary to make sure the tracer had similar properties to the original material. The surface, particle size distribution, and flowability were compared between the tracer material and the original DCPA material. Figure 4-16 shows an SEM image of the DCPA particles before and after nigrosin coating. Both particles appear to have a spherical shape, and the surface appears similar for both particles. The particle size distribution for the material before and after coating was measured and is presented inFigure 4-17. It can be seen that no significant agglomeration or attrition happened during coating. The cohesion was examined by carrying out a shear cell test at 3 kPa. During the shear cell test, vertical stress was applied to the powder bed under different normal stresses, and the yield stress was measured (see Figure 4-18). Extrapolating the curve to the y-axis gives the cohesion, which is the shear strength at zero normal strength. The cohesion of the original DCPA and the tracers are 0.36 kPa and 0.31 kPa, respectively.

Since most of the tracer experiments were carried out for dry materials in this study, it was necessary to investigate whether the dry powders can represent the flowability of our wet powders. Figure 4-19 shows the RTD curves from, otherwise identical, experiments with the exception of the initial moisture content of the powders. The wet material had 20%

moisture content (dry basis weight percent) and the dry material had about 1% moisture content (dry basis weight percent). The RTD curves showed similar peaks and tails indicating that the tracer tests conducted with dry materials can represent the hydrodynamics of the wet materials.

As mentioned in the previous section, two methods using colorimetry and NIR spectrometer were developed to obtain RTD. Figure 4-20 shows the comparison of the RTD obtained from run #4 in the DOE using both methods. Both methods captured the time when the peak of tracer concentration appeared. At time point around 18 – 22 min, a plateau was appeared and was captured by both methods. However, the NIR method gave a slightly higher value of the peak than the colorimetry. This could be due to that NIR data acquisition was finished earlier than the colorimetry method and missed the tail of the curve. The peak was, therefore, higher when the RTD was normalized by the area under the curve. For the rest of the study, colorimetry was used for tracer concentration measurement.

4.3.2 Effect of the Operating Conditions on Residence Time Distribution

In this section, the effect of several process parameters (loading, material flow rate, and the air flow rate) will be discussed. The residence time distribution curves are shown in Figure 4-21 for all operating conditions listed in Table 4-1. At first glance, a single peak followed by an exponential decay was observed for all curves. A short delay (around 1 min) was observed before a peak appeared. Table 4-2 summarizes some important criteria of the RTD curves. For an ideal reactor with fixed volume and material flow rate, the theoretical space time is the ratio of the volume to the material flow rate. Similarly, for the GPCG-2 fluidized bed, the theoretical space time was defined as the ratio of the loading to the material flow rate. It was observed that the experimentally observed mean residence time

was smaller than the theoretical space time. The effective material flow rate was less than the setpoint indicating the material flow was partially trapped in the fluidized bed. For the 4 kg cases, the theoretical space time was almost twice the value of the mean residence time. For the 2 kg cases, the theoretical space time was closer to the mean residence time. The higher initial loading would result in more stagnant flow or dead space.

4.3.2.1 Effect of Initial Loading on Residence Time Distribution

During the process, the materials experienced two motions – the circulation inside each segment due to the fluidization and the forward motion due to the materials being pushed by the inlet stream toward the outlet. Therefore, instead of filling materials into an empty fluidized bed dryer, the GPCG-2 was prefilled with a certain amount of materials and operated as a batch unit at the beginning of the process, and then the inlet stream was introduced to achieve continuous operation. Such an operating procedure allowed the unit to reach a steady state more rapidly during the startup process. As the inlet and outlet streams were kept constant throughout the process, it was expected that once the system reached steady state the resulting operation would be independent of the initial loading and there would thus be one steady state. However, this is not what was observed. Figure 4-22 shows the steady-state RTD curves from experiments, otherwise identical, with different loadings. It can be seen that the system exhibited multiple steady states and the resulting steady-state was a function of the initial loading. This result is not surprising considering the complexity of our fluidized bed system where the initial loading affects the extent of fluidization, which in turn affects the flow of solids through the segments of the fluidized bed. As can be seen in Figure 4-22, higher initial loading usually results in longer residence time. As the initial loading increased from 1 kg (#7) to 2 kg (#6) and to 4 kg (#3), the resulting RTD curve became broader (variance increased from 41.33 min^2 to 116.90 min^2

and 268.50 min^2, respectively), and the peak of the curve became higher than the peak of the lower loading conditions (#7 and #6). As the initial loading increased from 1 kg (#7) to 2 kg (#6) and to 4 kg (#3), the mean residence time increased from 13.13 min to 16.53 and 23.52 min, respectively. Similar results were found for experiments #5 and #1 at a higher level of inlet material flow rate (see Figure 4-21). A higher loading generally results in a more CSTR-like behavior which has a longer tail in the RTD curves (see Figure 4-21 experiments #1, #2 and #3).

4.3.2.2 Effect of Air Flow Rate on Residence Time Distribution

The air flow rate is a critical parameter for fluidized bed drying processes. An enhanced drying rate may be achieved by increasing the air flow rate, thus reducing the drying time. However, since the inlet air blows in from the bottom of the fluidized bed and promotes the movement of the particles, the high air flow rate may cause extra back-mixing which is generally undesirable in continuous drying as this causes wet material to mix with more dry material. The Peclet number, Pe, was used to quantify the mixing of the particles in the fluidized bed. Pe characterizes the ratio of convective transport to the dispersion transport in the reactor. The reactor behaves like a CSTR when $Pe = 0$ where dispersion transport dominates. As the Pe increases, clearer plug flow behavior will be observed for the reactor.

The effect of the air flow rate on the RTD curve is shown in Figure 4-23 at a high solids/material flow rate. For an air flow rate increase of 50% from 60 m^3/h (#4) to 90 m^3/h (#5), only a slight change in the peak height can be observed. The mean residence time was similar for both cases – 10.68 min (#4) as compared with 10.53 min (#5). Both RTD curves also had similar variance – 66.89 min^2 (#4) as compared to 66.57 min^2 (#5). The increase

in air flow rate did not substantially enhance the dispersion transport of the particles, since the Pe remained similar (1.87 and 1.77 for experiments #4 and #5). Similar results were also found for experiments #2 and #3 at low solids flow rate. The above results indicated that for the air flow rate we examined, the air flow rate did not affect the behavior of the fluidized bed dryer significantly.

4.3.2.3 Effect of Material Flow Rate on Residence Time Distribution

The effect of the material flow rate on the RTD curves is shown in Figure 4-24 for a low initial loading (2 kg). As the material flow rate increases from 5 kg/h (#6) to 10 kg/h (#5) and to 15 kg/h (#8), the peak height increased almost proportionally, and the peak width was reduced. The mean residence time reduced from 16.53 min (#6) to 10.53 min (#5), and then to 7.04 min (#8). The variance reduced from 116.90 min^2 (#4) to 66.57 min^2 (#5) and then to 20.30 min^2 (#8). The increase in material flow rate overall slightly enhanced the dispersion transport of the particles as the Pe decreased from 3.31 (#6) to 1.77 (#5) at a lower initial loading and from 2.7 (#3) to 2.14 (#1) at a higher initial loading. Despite the change in Pe, the fluidized bed dryer still operates as a fairly well-mixed system with a large amount of dispersion.

4.3.3 Tank in Series (TIS) Model Fitting

In many chemical processes, the continuous stirred tank reactor (CSTR) model is used to describe an ideal reactor with perfect mixing. However, in reality, not all reactors are CSTRs, and consequently, many RTD models are developed to allow some deviation from the ideal reactor. Since the GPCG-2 fluidized bed system has a four-segment product chamber, a tank-in-series (TIS) model seemed to be a reasonable start for a fitting model to the RTD curves. The TIS model assumes the reactor to be equivalent to several identical CSTRs that run in series. When the number of CSTRs approaches infinity, the reactor

behaves identically to a plug flow reactor (PFR). A generalized TIS model with a lag time term included is shown in Eq. 4-9.

$$E(t) = \frac{(t - t_p)^{n-1}}{(n-1)!\,{\tau_i}^n}\ e^{-\frac{(t-t_p)}{\tau_i}}$$

Eq. 4-9

where t_p is the lag time, n is the number of CSTRs and τ_i is the mean residence time of each CSTR where:

$$\tau_i = \frac{t_m}{n}$$

Eq. 4-10

The RTD experimental data was fitted to the TIS model using the OriginPro 2018 (OriginLab) nonlinear fitting tool. The orthogonal distance regression (ORD) algorithm was used for curve fitting where the algorithm minimizes the orthogonal distance from the data to the fitted curve. Table 4-3 summarizes the TIS model parameters for the fits of the experimental data. A gamma function was used to approximate the factorial term in Eq. 4-9 to allow for non-integer values of n and achieve better fitting. R^2 ranged from 0.935 to 0.994 for the TIS model fittings. The number of CSTRs was less than two for all experiments which also confirms the conclusion that changing the material flow rate did not affect the mixing significantly. A lag time ranging from 0.59 min to 1.94 min was found for all tests except for experiment #7 which had a much higher lag time – we believe this was due to experimental error. The mean residence time from the TIS model fit agreed with the experimentally obtained value. Overall, the TIS model fitting showed a good representation of the RTD curves and it had therefore been used for effluent moisture content prediction.

4.3.4 Micromixing in a Continuous Fluidized Bed

During a continuous drying process, the feed stream is broken up due to fluidization right after entering the fluidized bed. The RTD provides information on how long the particles stay in the fluidized bed; however, the mixing state of the feed stream with the materials within the fluidized bed is unknown. A model describing the micromixing is crucial to understand and to control the continuous fluidized bed drying process. Zwietering et al. [143, 144] distinguished two extreme cases through two models– the segregation model and the maximum mixedness model.

In the segregation model (SM), the powders are broken up into discrete fragments characterized by particles with identical moisture content. Figure 4-25 depicts a schematic of the segregation model [143, 144]. The particle stream flows through a plug flow reactor with outlets following the arrows. The particles will leave the reactor in a manner such that the residence time distribution of the plug flow reactor is identical to the real reactor which, in our case, is the GPCG-2 fluidized bed dryer. The circles in Figure 4-25 represent the particle fragments. Each fragment dries independently in the fluidized bed and does not mix until at the exit of the fluidized bed. Therefore, the moisture of each fragment is directly correlated to the time spent in the fluidized bed dryer. Each fragment has its own moisture content depending on how long it has stayed in the fluidized bed. Because of the distribution of the residence time, a fragment ($E(t)$) of the incoming stream is dried with a conversion of the moisture content of $X(t)$. Therefore, the mean conversion of the drying process in the effluent stream will be an average of the conversions of all particles in the exit stream:

$$\bar{X} = \int_0^\infty E(t)X(t)dt$$

Eq. 4-11

where,

$$X(t) = 1 - \frac{C_A(t)}{C_{A_0}}$$

Eq. 4-12

and $C_A(t)$ can be obtained from drying kinetics as described in Eq.4-1.

The segregation model gives a prediction for general continuous reactors, and Eq. 4-11 gives a prediction of the moisture content after the reaching steady state operation. However, the GPCG-2 fluidized bed dryer was first operated as a batch unit, and then the inlet and outlet streams were "turned on" to allow continuous operation. Therefore, we were also interested in how the system reaches a steady state during the "start-up" phase after switching from batch to continuous operation. To obtain the drying curve before the steady state operation, a mass balance was carried out for the effluent stream.

Upon switching from batch to continuous operation, the effluent stream consisted of two groups of particles. The first group of particles came from the inlet stream. According to Eq. 4-3, $F(t)$ of the inlet stream left the fluidized bed dryer at time t. The second group of particles came from the prefilled particles based on the initial loading of the fluidized bed. The effluent stream flow rate is equivalent to the inlet stream flow rate. Therefore, $[1 - F(t)]$ of the effluent stream was coming from the prefilled particles. In a segregation model, the moisture content of these two groups of particles can be calculated separately, and the effluent moisture content would be an average moisture content of the two groups:

$$X_{effluent}(t) = \frac{F(t)\int_0^t E(t)X(t)dt + [1-F(t)]\,X(t)}{F(t)+[1-F(t)]}$$

Eq. 4-13

While SM gives the least amount of mixing, the maximum mixedness model (MMM) assumes the maximum possible mixing in the reactor. The MMM assumes that the inflowing material is dispersed on the smallest scale possible immediately after being fed into the fluidized bed. MMM can be considered as a plug flow reactor (PFR) with inlet flow entering from side entrance (see Figure 4-26)[143]. For an arbitrary RTD, the inlet stream was fed in such a manner that the RTD of the PFR is identical to the fluidized bed RTD. From the side entrance, let λ (life expectancy) be the time the particles take to leave the fluidized bed. It should be noted that particles with a life expectancy of 0 are at the right end of the reactor, and particles with a life expectancy of infinity are at the left end of the reactor. In MMM, the moisture content of the particles in the fluidized bed is an average of all particles within the fluidized bed. This situation is in contrast to the SM where all the particles have their own moisture content and do not mix until at the exit.

Using this approach, the model is developed based on a mass balance of the moisture contents over the increment between λ and $\lambda + \Delta\lambda$. At λ, the amount of moisture entering the reactor equals to $v_0 C_0 E(\lambda)\Delta\lambda$, where v_0 is the inlet flow rate. The amount of moisture entering at $\lambda + \Delta\lambda$ is $v_0[1 - F(\lambda)]C|_{\lambda+\Delta\lambda}$. The amount of moisture exiting from λ is $v_0[1 - F(\lambda)]C|_{\lambda}$. The moisture removed due to drying is $r_A v_0[1 - F(\lambda)]\Delta\lambda$. Carrying out a mass balance on the moisture content gives:

$$v_0[1 - F(\lambda)]C|_{\lambda+\Delta\lambda} + v_0 C_0 E(\lambda)\Delta\lambda - v_0[1 - F(\lambda)]C|_{\lambda} + r_A v_0[1 - F(\lambda)]\Delta\lambda = 0$$

Eq. 4-14

This equation can then be rearranged to:

$$\frac{dC_A}{d\lambda} = -r_A + \frac{E(\lambda)}{1 - F(\lambda)}(C_A - C_{A_0})$$

Eq. 4-15

Eq. 4-15 has been solved numerically using the Runge-Kutta method.

4.3.5 Predicting the Effluent Moisture Content

As described in the previous section, the continuous drying process can in principle be predicted by combining the drying kinetics, the residence time distribution, and the micromixing model. In this section, the model has been used to try to predict results for the operation of the continuous fluidized bed for 20% initial moisture content, 2 kg initial loading, 90 m^3/h air flow rate, and 80 °C air temperature. The model has been used to predict both a 5 kg/h material flow rate and a 10 kg/h material flow rate.

The drying kinetics were obtained by carrying out a batch experiment using the same operating conditions as in continuous operation. Figure 4-27 shows the drying curve from a batch experiment conducted for 2 kg initial loading with 20 % initial moisture, 80 °C, and 90 m^3/h air flow rate. As discussed previously, the batch drying curve was fitted using the Midilli et al. [74] empirical model (see Figure 4-27 orange line). If one examines the rate of drying (not shown), the drying process remains at a constant drying rate of 1.64 %/min until the moisture content drops to around 4% moisture content.

Using the method discussed in section 4.2.3, the drying curve was predicted and compared with the experimental data from the outlet of the continuous drying process. Figure 4-28 shows a comparison between the segregation model (SM) prediction, the maximum mixedness model (MMM) prediction and the experimental data for two different material

flow rates. The experimental data in Figure 4-28 showed that effluent moisture content from the dryer started off at an initial value close to the feed material (20% moisture content) and decreased non-linearly until steady state moisture was achieved. The steady-state effluent from the dryer was around 5% for 10 kg/h (see Figure 4-28a) and around 1% for 5 kg/h (see Figure 4-28b). The steady-state moisture content was higher for the higher material flow rate due to the smaller residence time of the material at a higher material flow rate. With the higher material flow rate of 10 kg/h (see Figure 4-28a), the segregation model was able to predict the moisture content until around 10 min but overestimated the steady state moisture content by about 2.4%. Similar results were found for the case with the material flow of 5 kg/h (see Figure 4-28b); the segregation model was able to predict the moisture content until around 10 min but overestimated the equilibrium moisture content by about 3.2%. While the SM overestimated the equilibrium moisture content, it is observed that the MMM was able to better capture both the evolution of the moisture content and the steady state moisture content in both cases.

The SM started to overestimate the moisture content after 10 min because the SM assumes that the mixing occurs at the exit of the reactor. Therefore, the drying rate solely depended on the age (time spent in the fluidized bed dryer) of each particle. If one examines the batch drying curve (see Figure 4-27) then one can see that the drying rate reaches the hindered drying rate (falling rate period) after approximately 10 min. Since the SM assumes that mixing occurs at the exit of the reactor, after around 10 min a large number of particles would have reached the hindered drying period, and the drying rate would drop. This situation can be observed in Figure 4-28a and Figure 4-28b where the predicted curves took a sharp turn at 10 min once the drying reached the hindered period (see Figure 4-27

at t = 10 min). On the other hand, the maximum mixedness model assumes that the mixing occurs once the particles enter the reactor. Even though the particles have different ages, the moisture content at a certain point is based on a mixture of the particles and thus is an average of those particles. The overall drying rate would still be unhindered even if, in practice, some of the individual particles had a lower moisture content and fell into the hindered period. The successful prediction of the effluent moisture content from the maximum mixedness model is consistent with the fact that we observed that a TIS model with a n value of around 2 could successfully model the GPCG-2 continuous fluidized bed dryer. This result indicates that the GPCG-2 continuous fluidized bed is close to a well-mixed system and it can be approximated by the maximum mixedness model.

In section 3, a scaling method was proposed to predict the drying kinetics in GPCG-2 using a smaller lab-scale fluidized bed dryer MiniGlatt. The results presented in section 3.3.5 showed the scaling method was successful. Therefore, the scaling method was also tested to validate for application in continuous processing. Figure 4-29 shows the prediction of the drying curve for GPCG-2 drying DCPA at 80C temperature with 1kg loading and 90m^3/h air flow (shown in the blue dots) based on a MiniGlatt drying process (shown in the orange dots). Using the maximum mixedness model to convolute the drying kinetic data and RTD data, the prediction of the effluent moisture content for continuous drying of DCPA at 80°C temperature with 5 kg/h mass flow rate, 1kg initial loading, and 90m^3/h air flow was obtained as shown in Figure 4-30. The prediction and the experimental data showed good agreement. With the drying kinetic data obtained by scaling from smaller scale fluidized bed drying experiments, the required materials and time for testing was

significantly reduced. The scaling method has proven to be a useful tool to provide drying kinetic data for the continuous fluidized bed drying process development.

4.3.6 Effect of the Operating Conditions on Effluent Moisture Content

The previous section 4.3.5 showed that a combination of using the scaling method introduced in section 3 and the maximum mixed model had successfully predicted the effluent moisture content of a continuous fluidized bed drying process. Using such method, the drying curves under different operating conditions were obtained. A $2^{(4-1)}$ factorial design was carried out to investigate the effect of initial loading, airflow, air temperature and material flow rate on the effluent moisture content.Table 4-4 lists the effluent moisture content predictions.

The effect of initial loading (1kg, 2kg, and 4kg) was presented in Figure 4-31. The effluent moisture content eventually reached a similar steady state for all of the three conditions. For a batch drying process, a higher loading will in general results in a lower drying rate (see section 2). In the GPCG-2 continuous fluidized bed drying system, we discovered a similar trend. The 1 kg case reached steady state much faster than the higher mass holdup cases (2 kg and 4 kg) because a lower initial loading resulted in a shorter mean residence time of the materials.

The effect of air flow (60 m^3/h and 90 m^3/h) was presented in Figure 4-32. The effluent moisture content eventually reached steady state at the same time as the residence time distribution was not affected by the air flow. For a batch drying process, a higher airflow will in general results in a higher drying rate (see section 2). In the GPCG-2 continuous fluidized bed drying system we discovered a similar trend. The 90m^3/h case dried faster than the 60 m^3/h cases. Furthermore, the 60 m^3/h case wasn't able to reach the endpoint of

drying and equilibrate at about 7% moisture content. This was because the drying rate of the 60m^3/h case was slower than the rate of moisture increase due to wet materials flowing into the fluidized bed.

The effect of air temperature (60 and 80 °C) was presented in Figure 4-33. The effluent moisture content eventually reached steady state at the same time as the residence time distribution was not affected by the air flow. For a batch drying process, the higher air temperature will in general results in a higher drying rate (see section 2). In the GPCG-2 continuous fluidized bed drying system, we discovered a similar trend. The 80°C case dried faster than the 60°C case. Furthermore, the 60°C case reached a steady state at a higher moisture content than the 80°C case.

The effect of material flow rate (5 kg/h and 10 kg/h) was presented in Figure 4-34. The 10 kg/h case reached steady state sooner than the 5 kg/h case since higher material flow rate would result in a shorter mean residence time. The 10 kg/h case reached a steady state at a higher moisture content than the 5 kg/h case because the rate of moisture increase due to the wet materials flowing in was higher, and the drying rate cannot compete with the moisture increase.

By carrying our a Pareto analysis, the significance of the operating parameters were quantified. Figure 4-35 presents the Pareto chart of the effects. It was found that all of the four operating parameters have significant effect on the effluent moisture content. The effect of interactions between operating parameters were not important. Figure 4-36 shows the contour plots of the effects. The drying process in a continous fluidized bed is a competition between the rate of drying and the rate of moisture increase due to the wet

material flowing in. Unlike in a batch fluidized bed dryer where the materials will eventually be dried to the endpoint, materials in a continuous fluidized bed dryer may never be completely dried due to lack of driving force of drying or short residence time. A large initial loading, low airflow and low air temperature will results in a lack of drying. A large initial loading and a high material mass flow will results in a short material residence time. As was discussed in Chapter 1, the drug products are typically desired to have an appropiate moisture content level that is suitable for tablet compaction, as well as not causing the API phase change. It is therefore important to design the continous drying process based on the required product moisture content. Using the method provided in this chapter, one should be able to choose an RTD as short as possible to be just enough to reduce the product moisture content to the required level.

4.4 Conclusion

In this section, the GPCG-2 continuous fluidized bed dryer was characterized by studying the effect of several critical process parameters on the residence time distribution. The residence time distribution was measured by a tracer response experiment. The increase of initial loading could reduce the peak height and increase the peak width of the RTD curve. The air flow rate has an insignificant effect on the RTD curve. The material flow rate increases the peak height and reduces the peak width of the RTD curve. Despite the effect of the aforementioned critical process parameters, the Pe number was low for all the cases studied, indicating a high degree of dispersion transport in the continuous fluidized bed.

The effluent moisture content was predicted by combining the drying kinetics from a batch experiment, the TIS model by fitting the RTD data, and the micromixing models. Two

micromixing models were examined – the segregation model and maximum mixedness model. The segregation model overestimated the steady state moisture content in the effluent stream because the drying rate dropped significantly after a certain amount of particles fell into the hindered drying period. The maximum mixedness model gave a good prediction of the effluent moisture content for the dryer that we examined, and the conditions that we studied. An investigation on the effect of the operating parameters on the effluent moisture content showed that low initial loading, low material flow rate, high airflow and high air temperature will result in a low effluent moisture content.

The suggested work flow for a continuous fluidized bed dryer:

1. Obtain RTD under different operating conditions by tracer experiments.
2. Obtain the drying kinetic by batch drying experiments or the scaling method introduced in Chapter 3.
3. Calculate the product effluent moisture content using the maximum mixedness model.
4. Identify the design space baced on the required product moisture level.
5. Extrapolate the design space if the required product moisture level is out of the boundary by changing the drying parameters (loading, air temperature and airflow). The new drying kinetics can be obtained through the scaling method.

4.5 Figures for Chapter 4

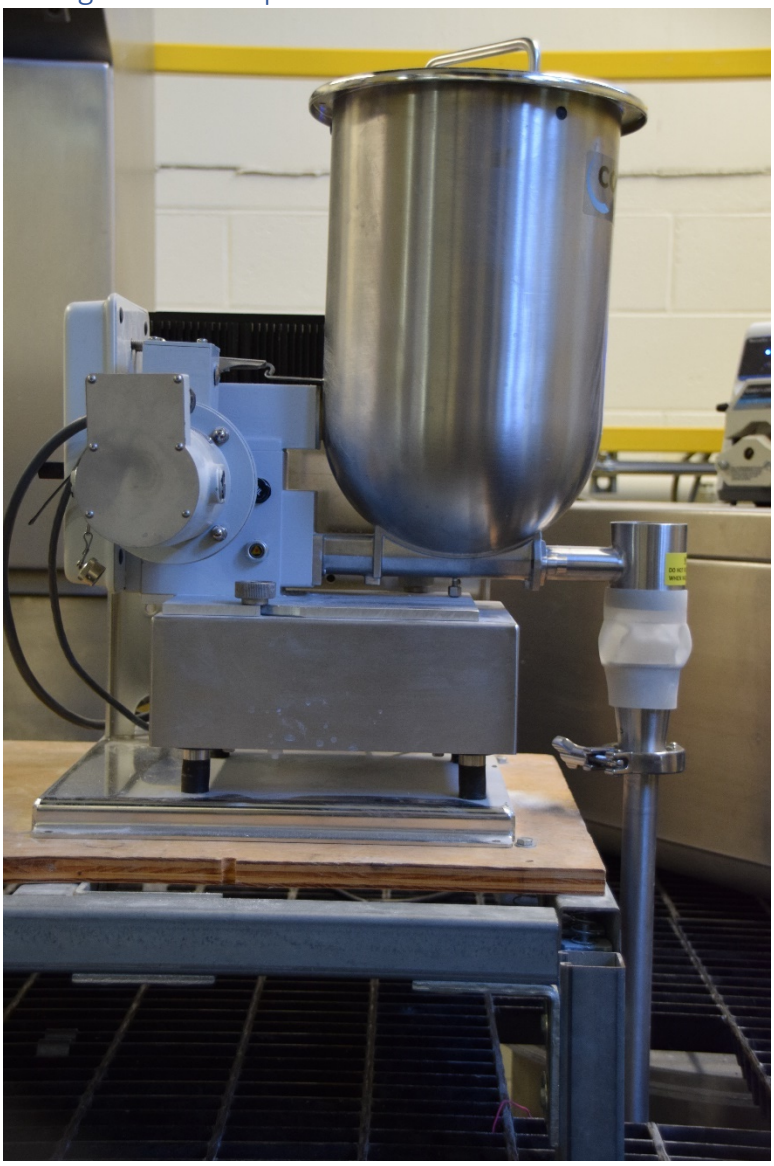

Figure 4-1: KT20 loss-in-weight feeder

Figure 4-2: Rotary valve external view (left) and internal structure (right).

Figure 4-3: GPCG-2 fluidized bed system.

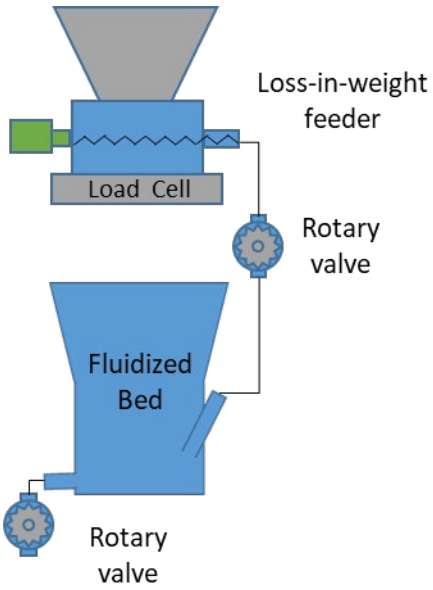

Figure 4-4: Experimental setup of the continuous fluidized bed drying line.

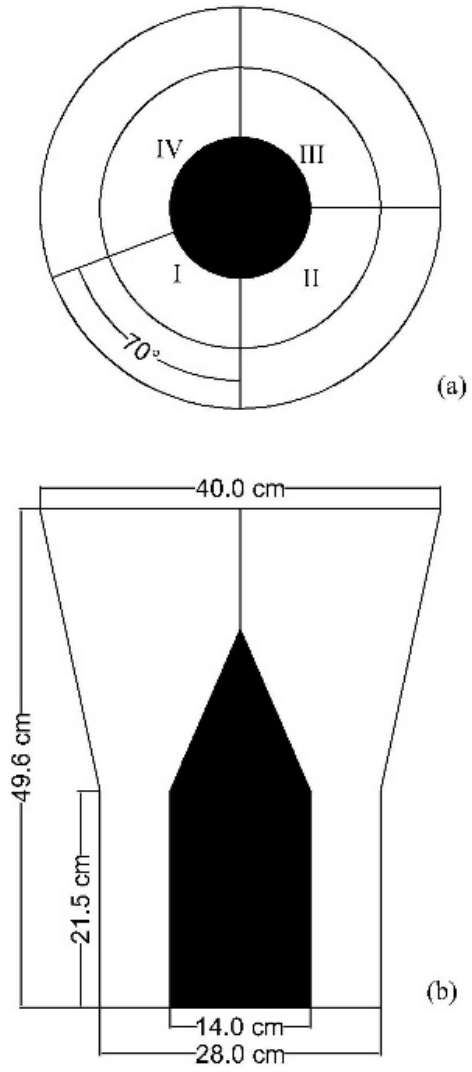

Figure 4-5: Top view (a) and side view (b) of Glatt GPCG-2 continuous fluidized bed system.

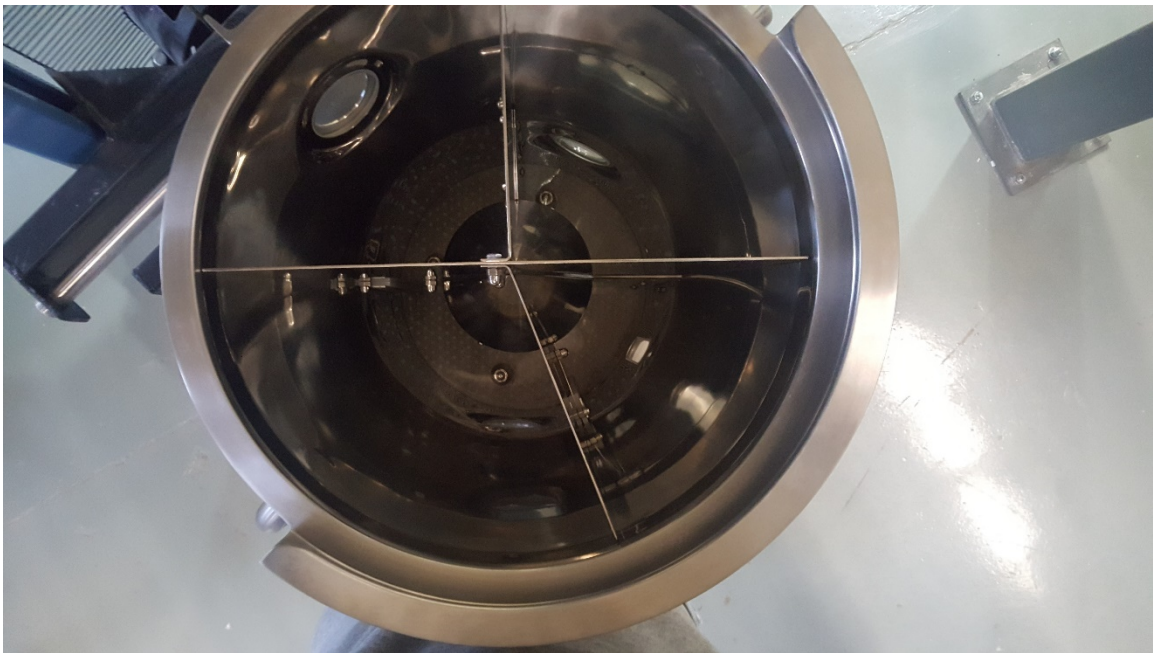

Figure 4-6: Top view of the GPCG-2 chamber.

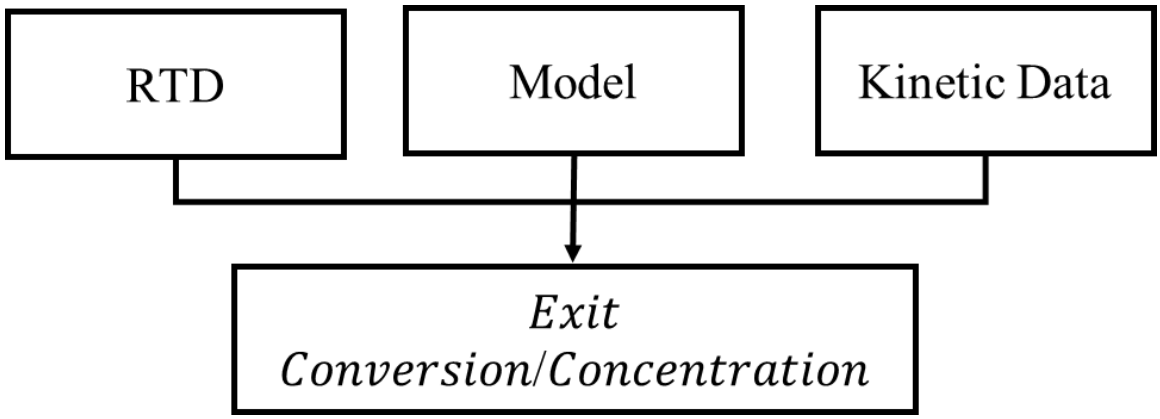

Figure 4-7: Method of obtaining exit conversion for a continuous fluidized bed dryer.

Figure 4-8: Tracer powder. (a) DCPA tracer (left) vs. DCPA powder (right) and (b) DCPA powder mixed with different concentrations of the tracer.

Figure 4-9: Color spectrometer.

Figure 4-10: NIR spectrometer

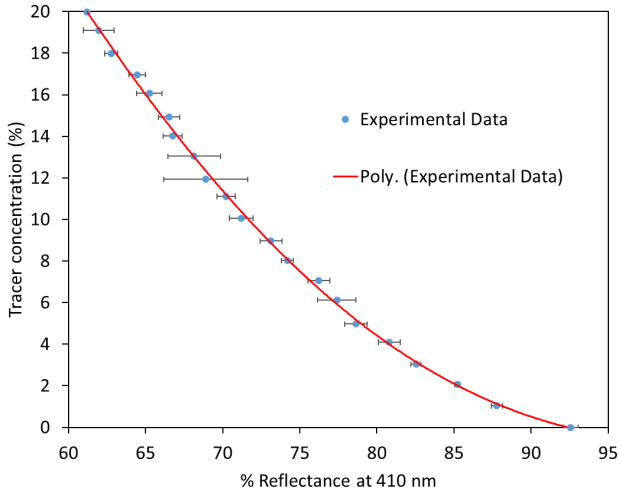

Figure 4-11: Calibration for the tracer.

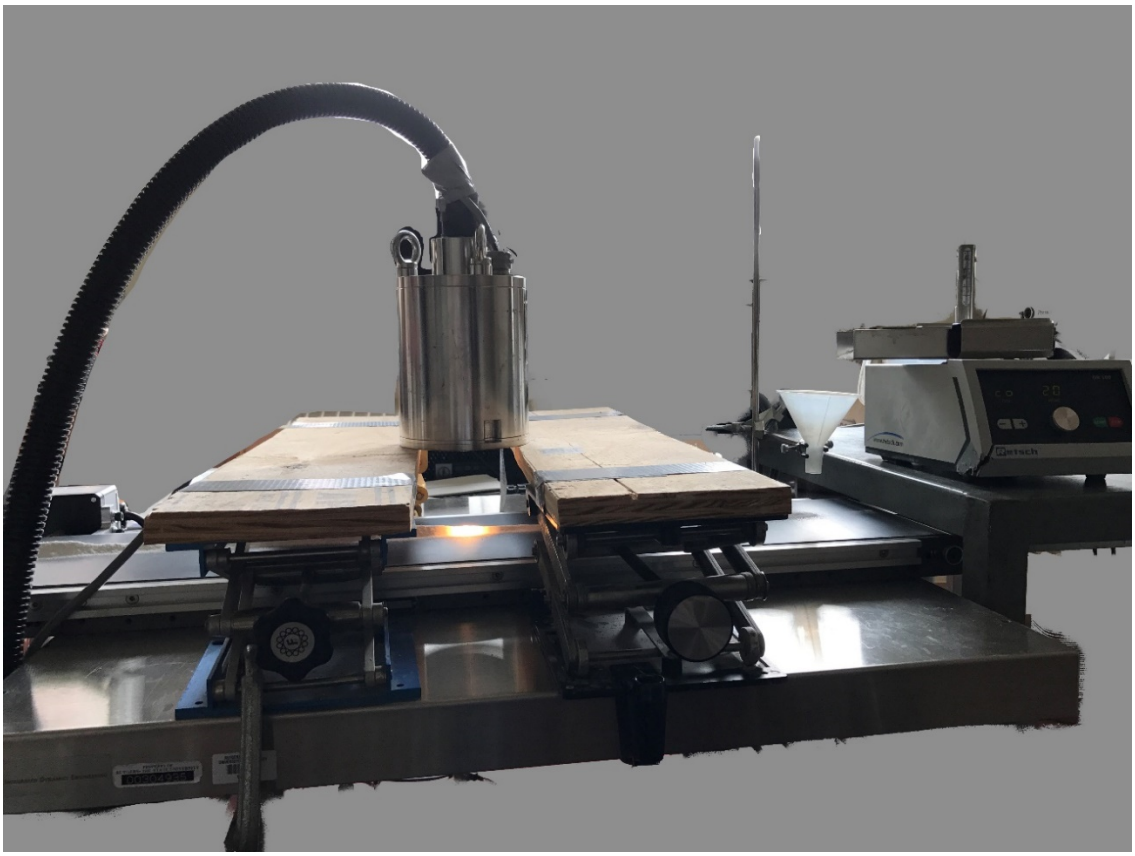

Figure 4-12: Setup for calibration sample measurement.

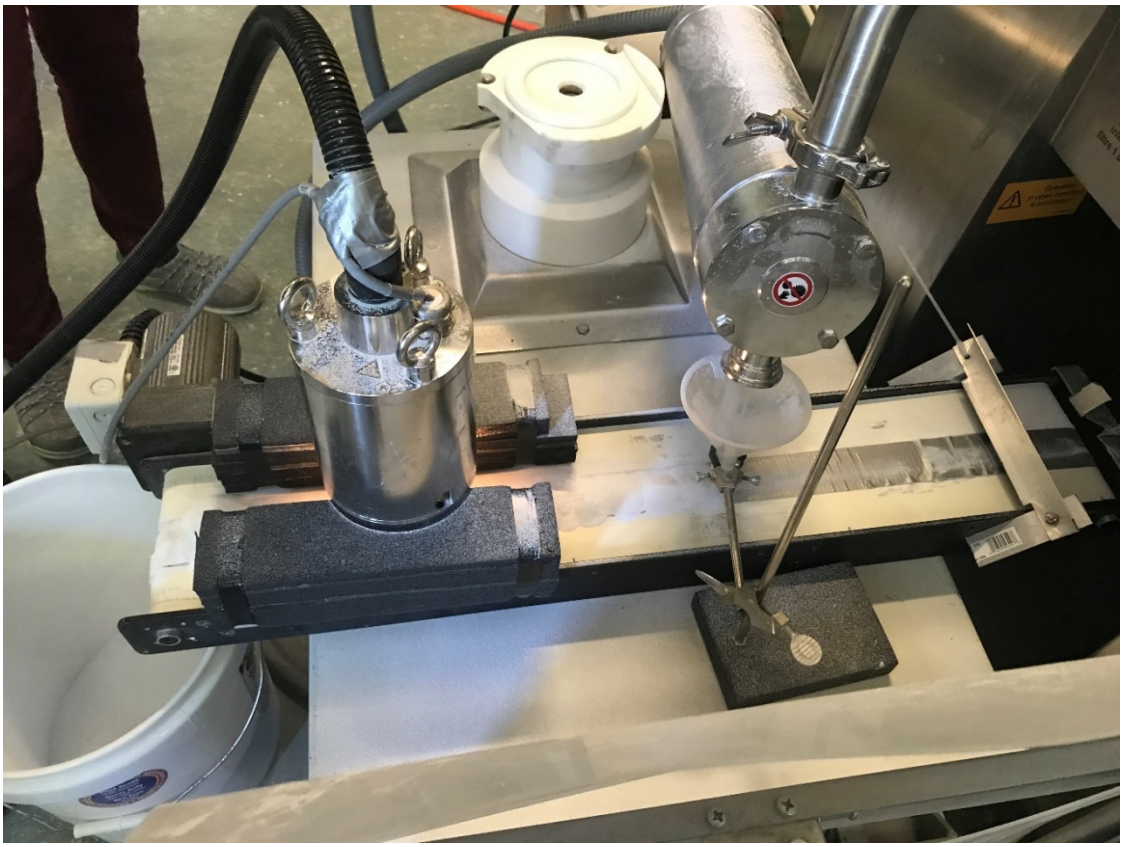

Figure 4-13: NIR probe setup during the continuous fluidized bed process.

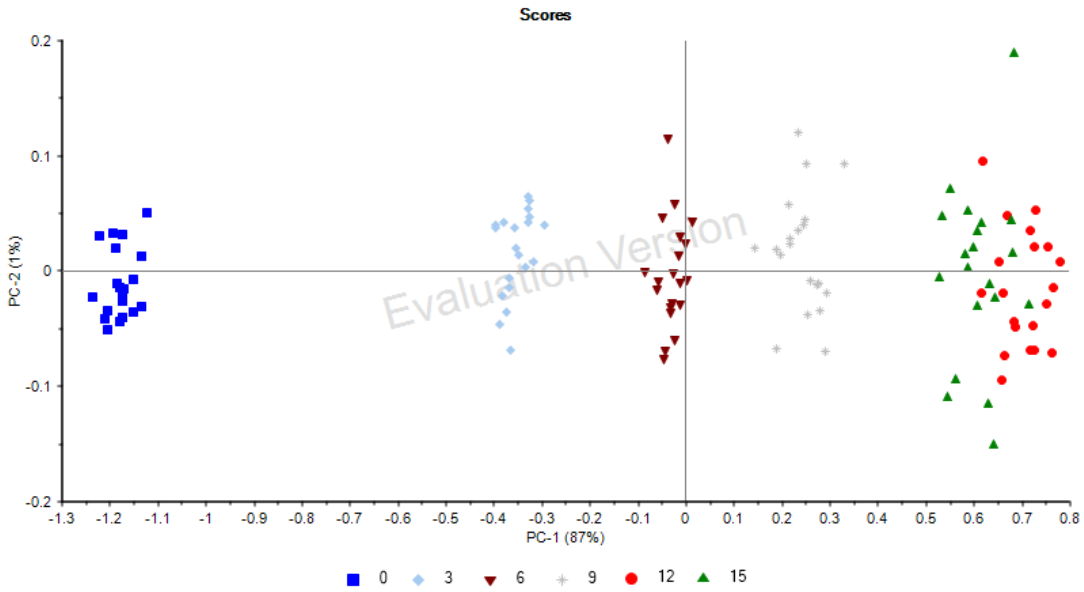

Figure 4-14:PCA score plots of the NIR spectra for calibration blends with 0, 3, 6, 9, 12, 15 (wt. %) using MSC spectral preprocessing.

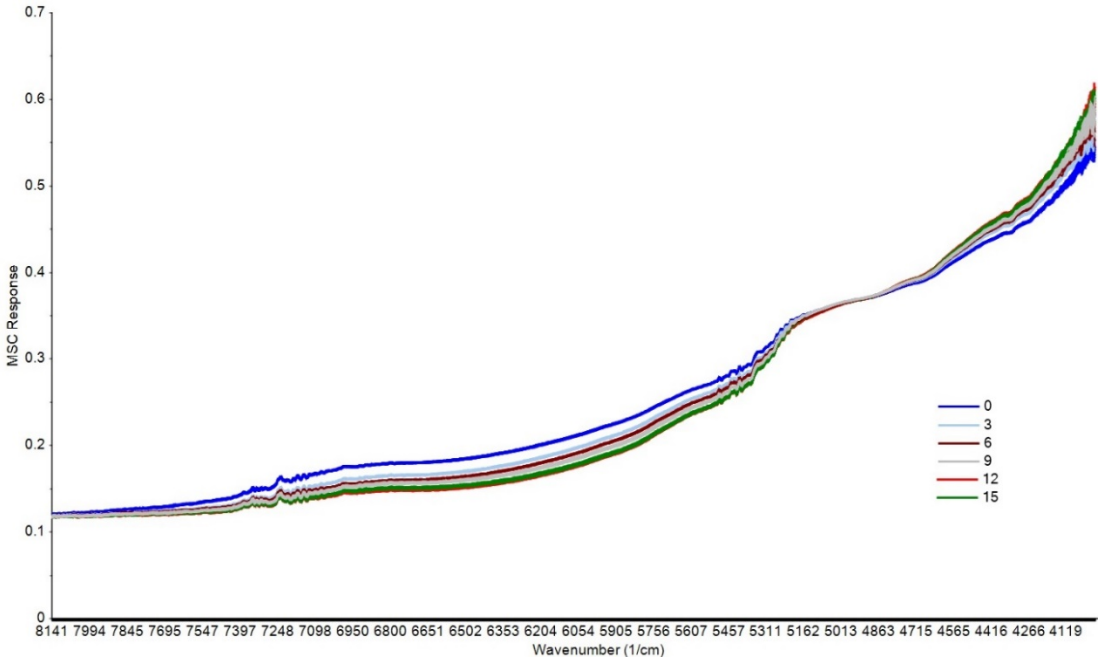

Figure 4-15: MSC NIR spectra calibration blends.

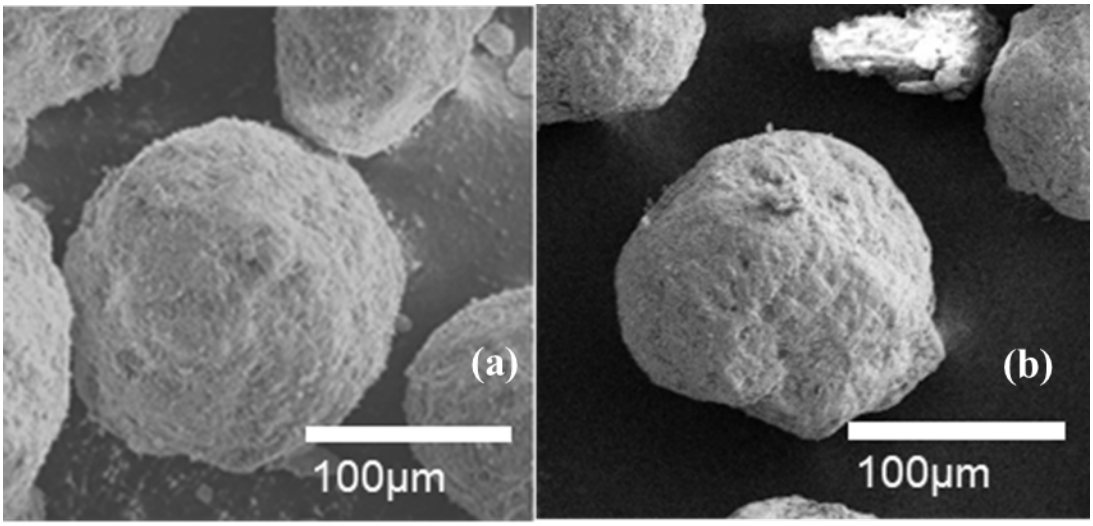

Figure 4-16: SEM image of DCPA particle before coating (a) and after coating (b).

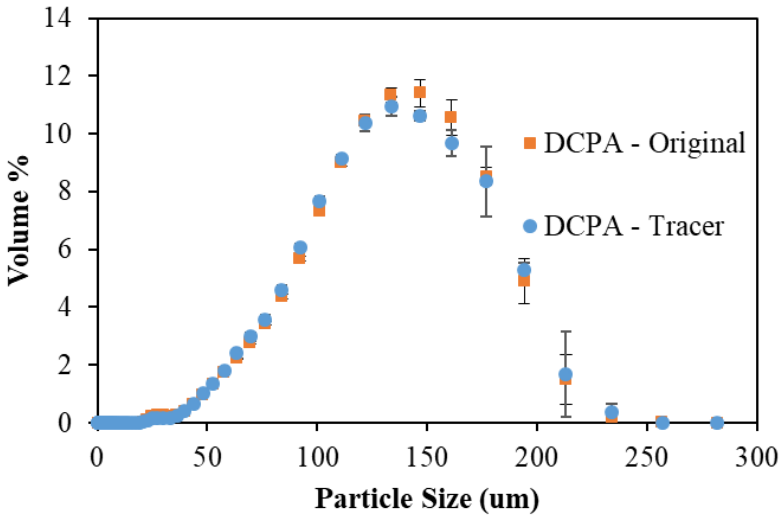

Figure 4-17: Particle size distribution of DCPA before and after coating.

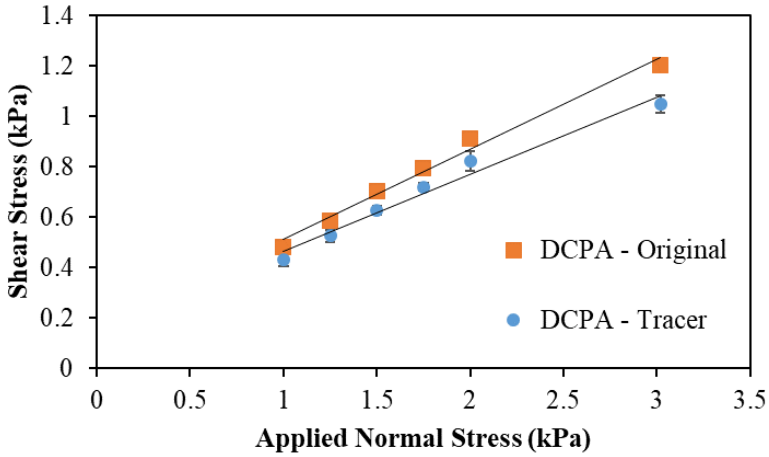

Figure 4-18: Shear cell test at 3kPa before and after coating.

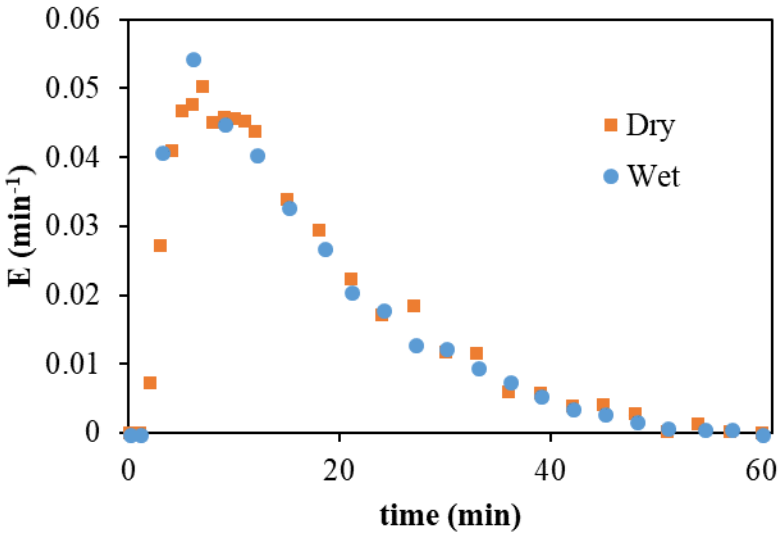

Figure 4-19: Residence time distribution of dry and wet materials in GPCG-2 with 2 kg initial loading, air flow rate of 90 m^3/h, and material flow rate of 5 kg/h.

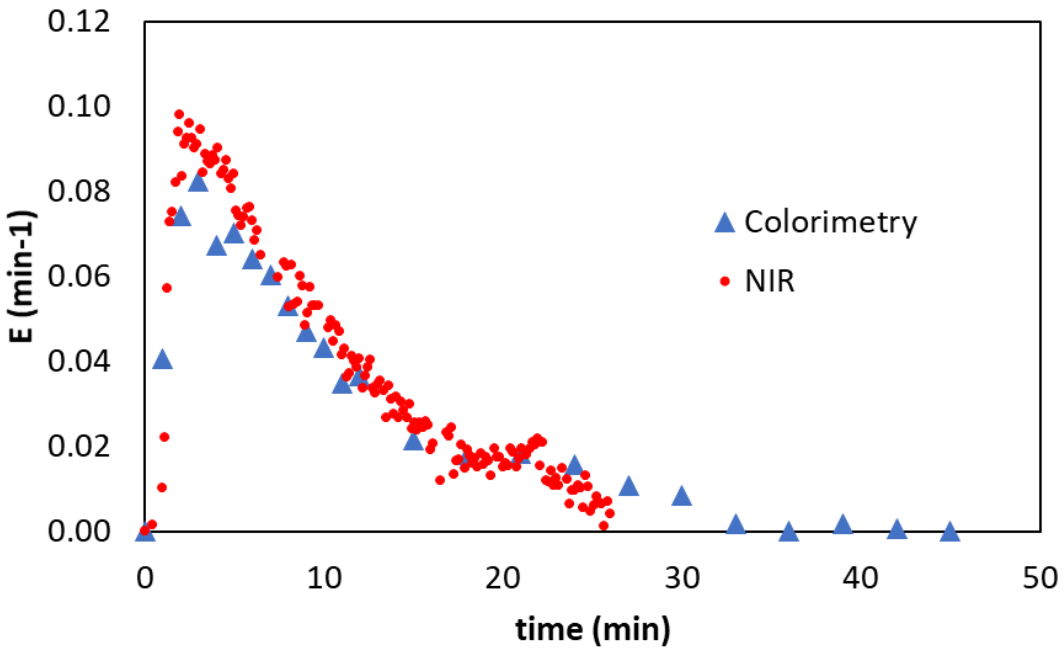

Figure 4-20: RTD data obtained from colorimetry and NIR.

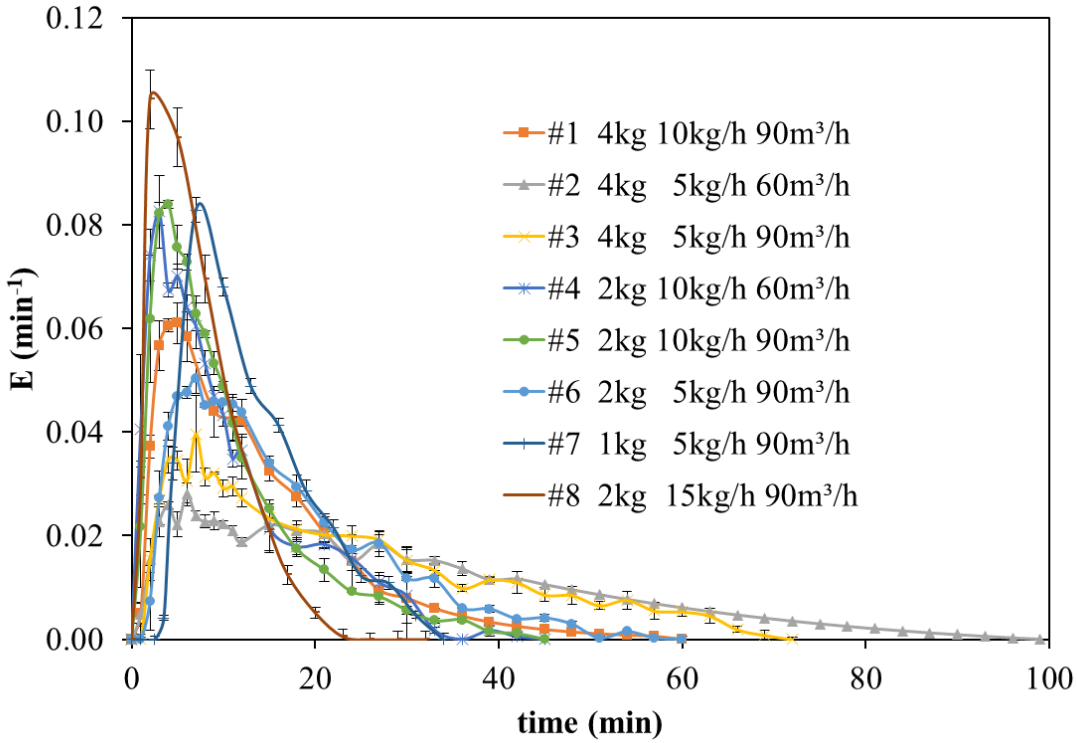

Figure 4-21: Residence time distribution of all experiments. The results correspond to 1kg, 2kg and 4kg initial loadings (first column of legend); 5kg/h, 10kg/h and 15kg/h material flowrates (second column of legend); and 60m^3/h and 90 m^3/h air flowrates (third column of the legend).

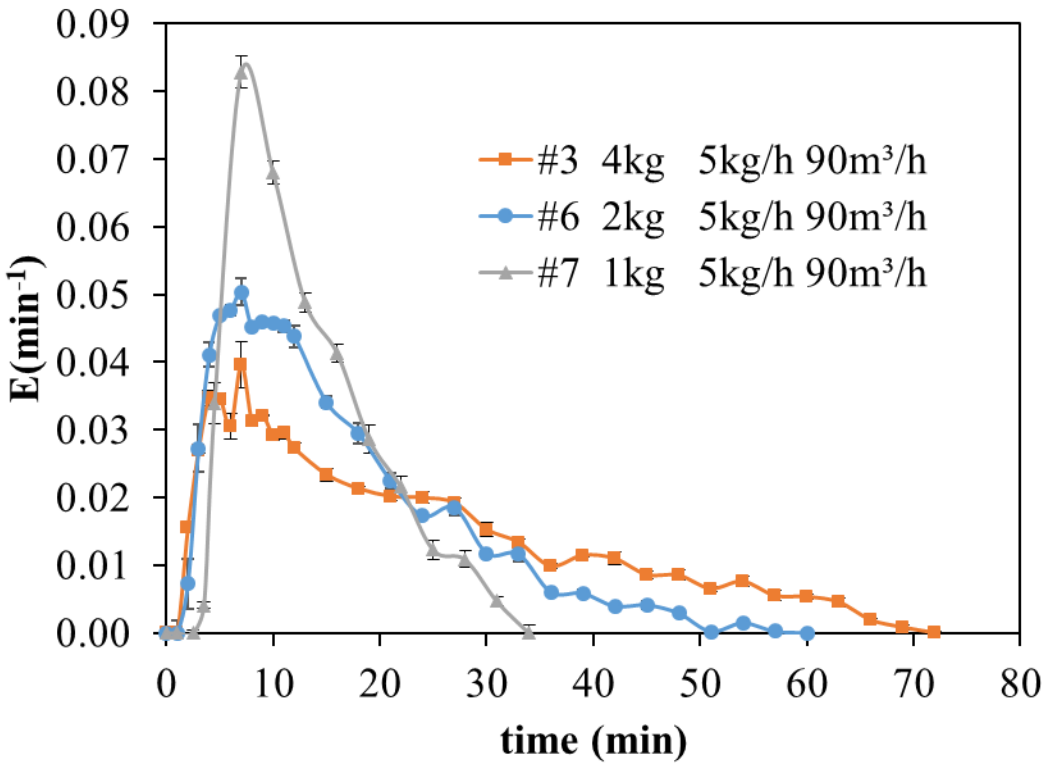

Figure 4-22: Comparison of RTD curve at different initial loadings.

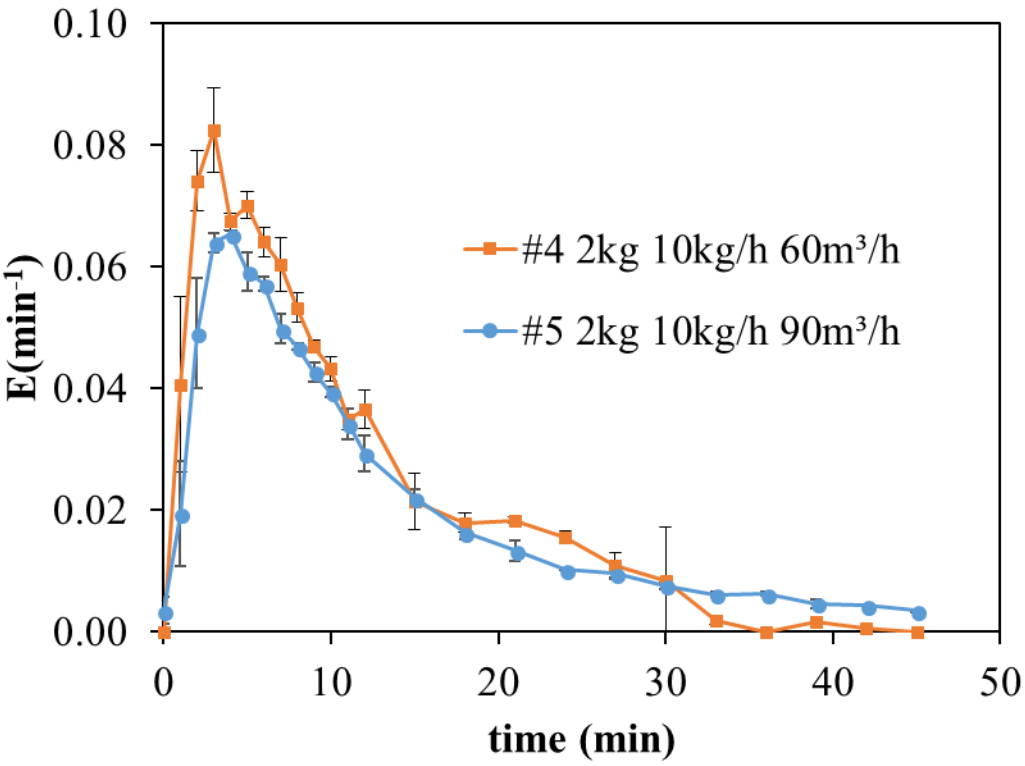

Figure 4-23: Comparison of RTD curves for different air flow rates.

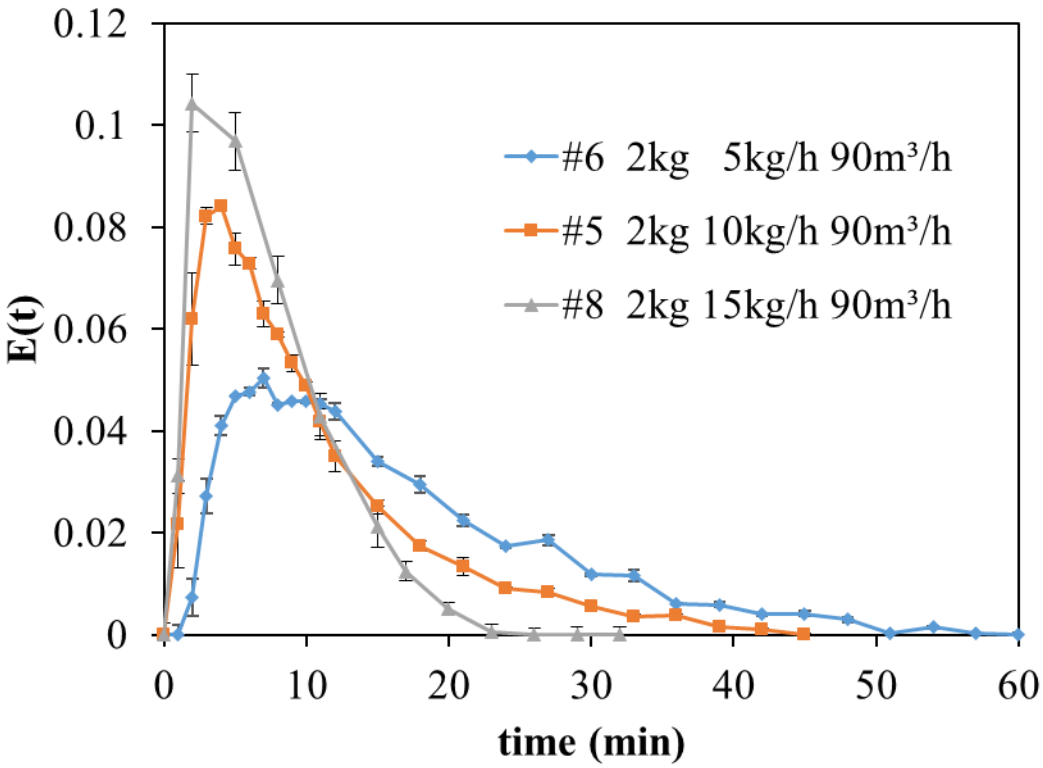

Figure 4-24: Comparison of RTD curves for different material flow rates.

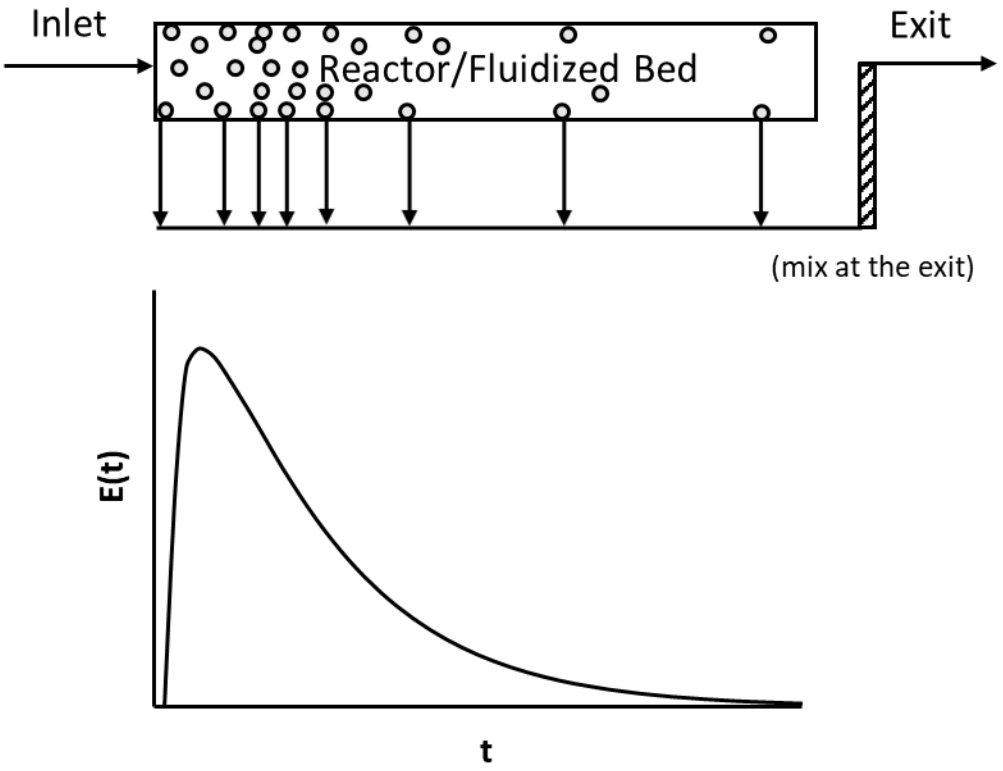

Figure 4-25: Conceptual basis for segregation model. Schematic of the segregation model (top) and resulting residence time distribution (bottom).

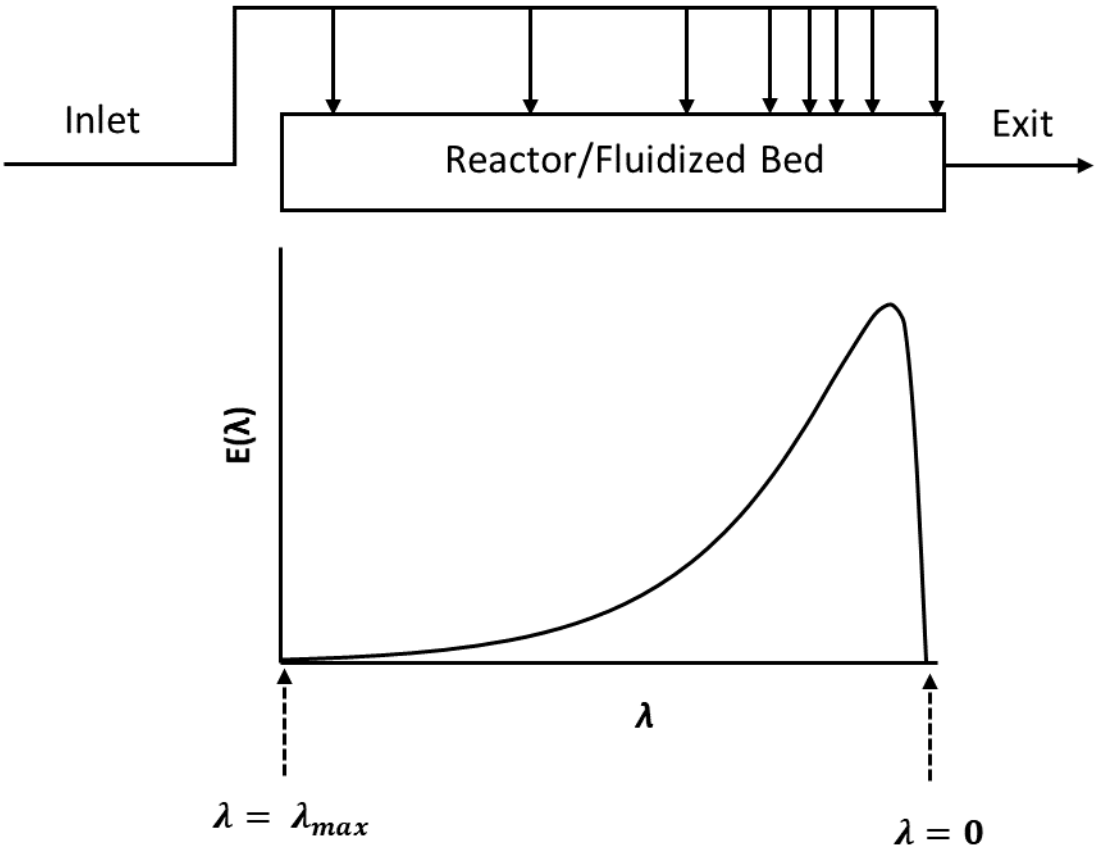

Figure 4-26: Conceptual basis for maximum mixedness model. Schematic of the maximum mixedness model (top) and resulting residence time distribution (bottom).

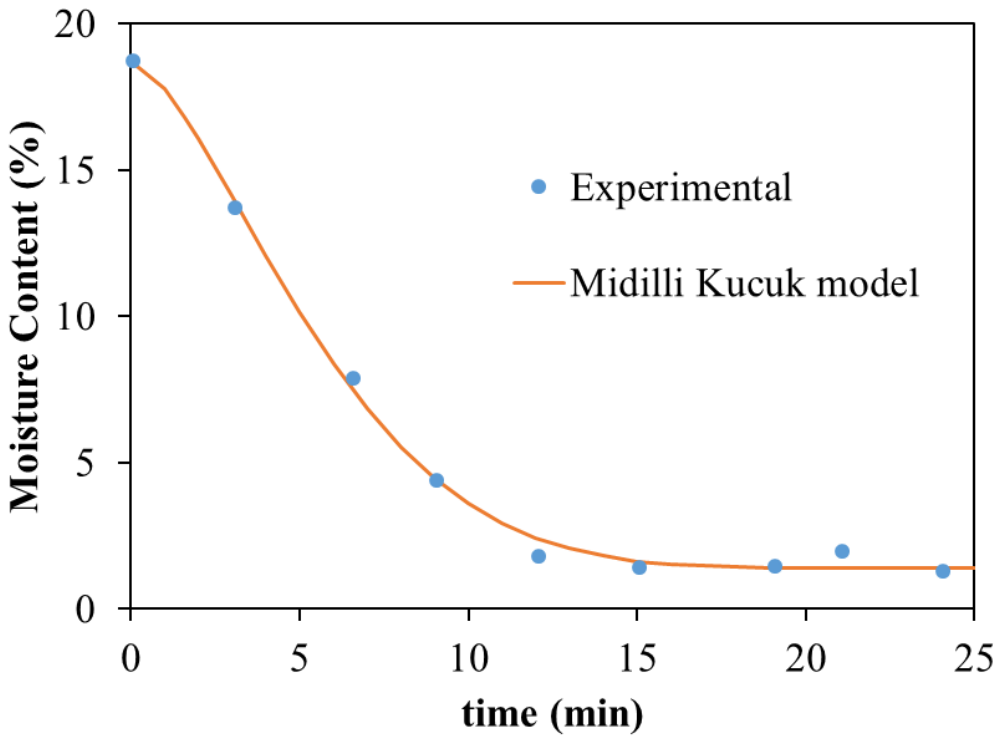

Figure 4-27: Drying curve obtained from a batch experiment conducted at 2 kg initial loading with 20 % initial moisture, 80 °C, and 90 m^3/h air flow rate.

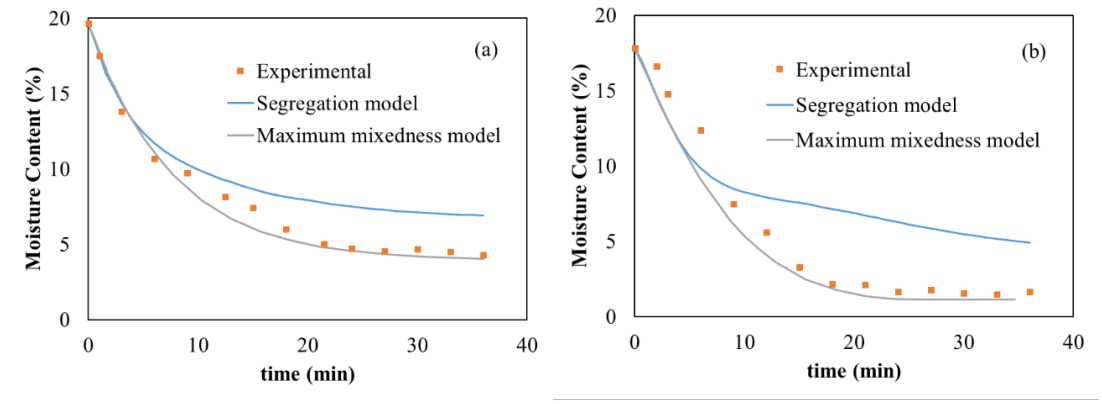

Figure 4-28: Comparison of SM and MMM prediction of drying at 2 kg initial loading with 20 % initial moisture, 80 °C, and 90 m^3/h air flow rate with a material flow of (a) 10 kg/h and (b) 5 kg/h.

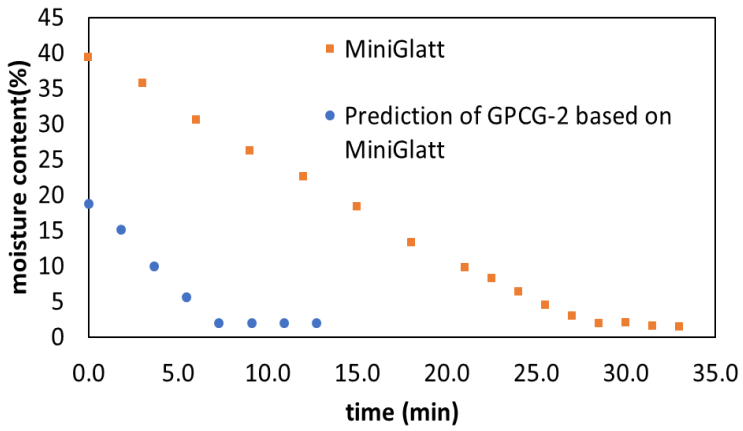

Figure 4-29: Prediction of GPCG-2 batch drying based on MiniGlatt drying process.

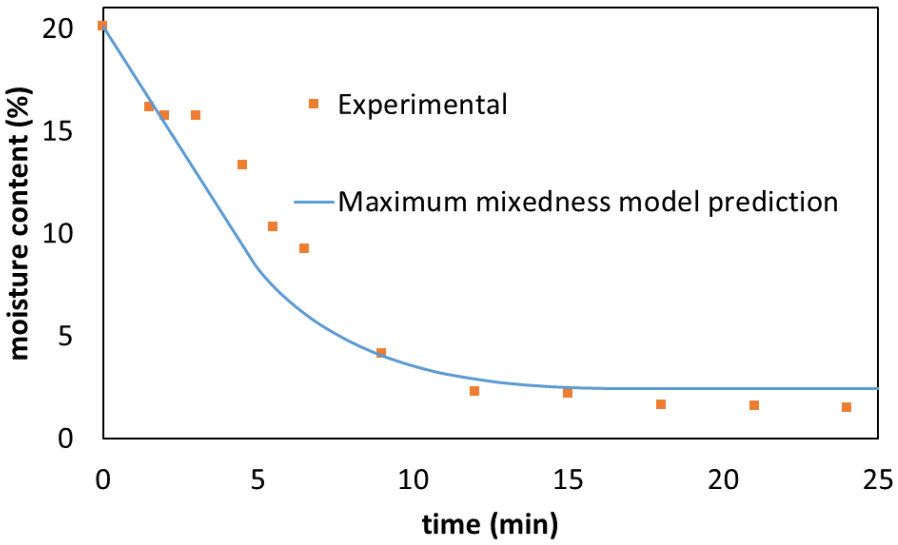

Figure 4-30: GPCG-2 effluent moisture content prediction using the maximum mixedness model based on the drying kinetic data scaled up from the MiniGlatt.

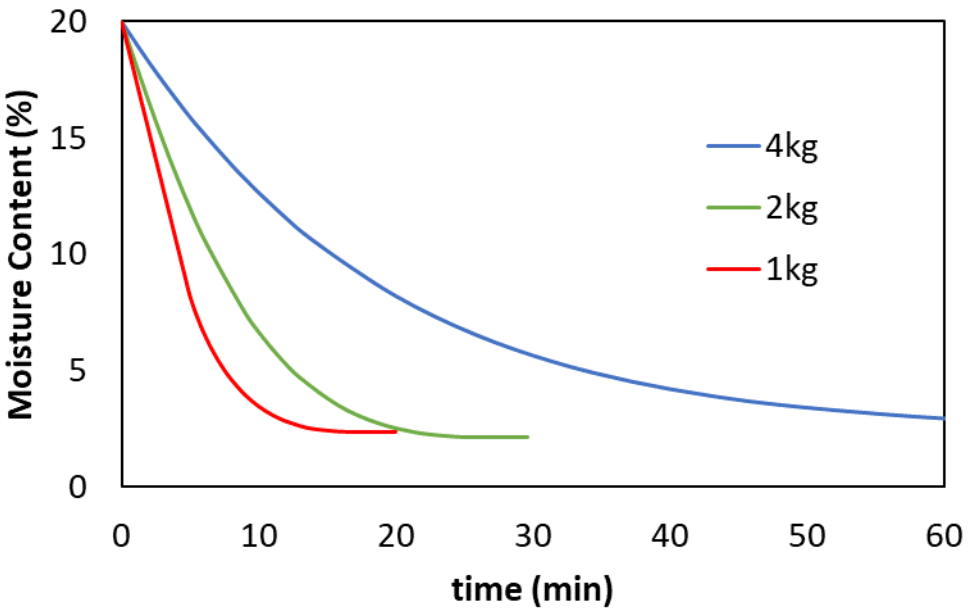

Figure 4-31: Effluent moisture content of GPCG-2 drying under different initial loading (Air temperature 80°C, air flow 90 m^3/h air flow, and 5kg/h material flow rate).

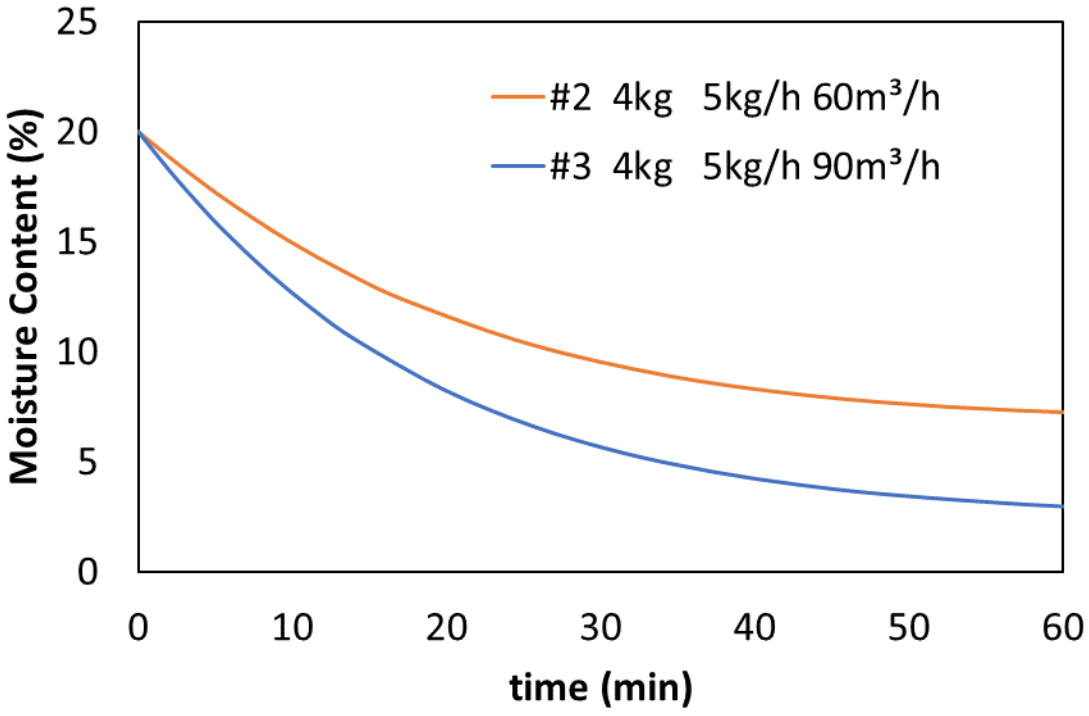

Figure 4-32: Effluent moisture content of GPCG-2 drying under different air flow (Air temperature 80°C, 4 kg initial loading, and 5kg/h material flow rate).

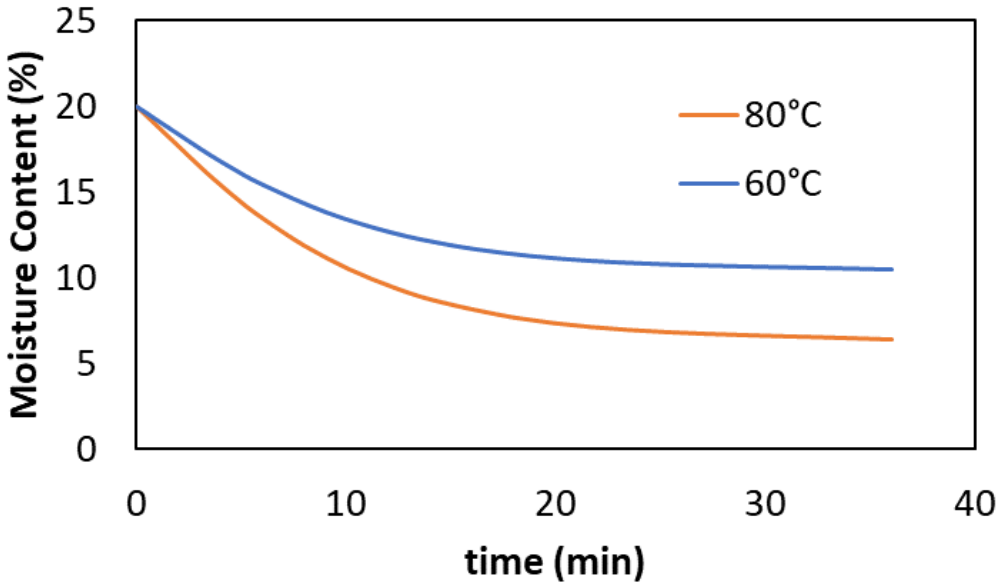

Figure 4-33: Effluent moisture content of GPCG-2 drying under different air temperature (2 kg initial loading, 60 m^3/h air flow and 5kg/h material flow rate).

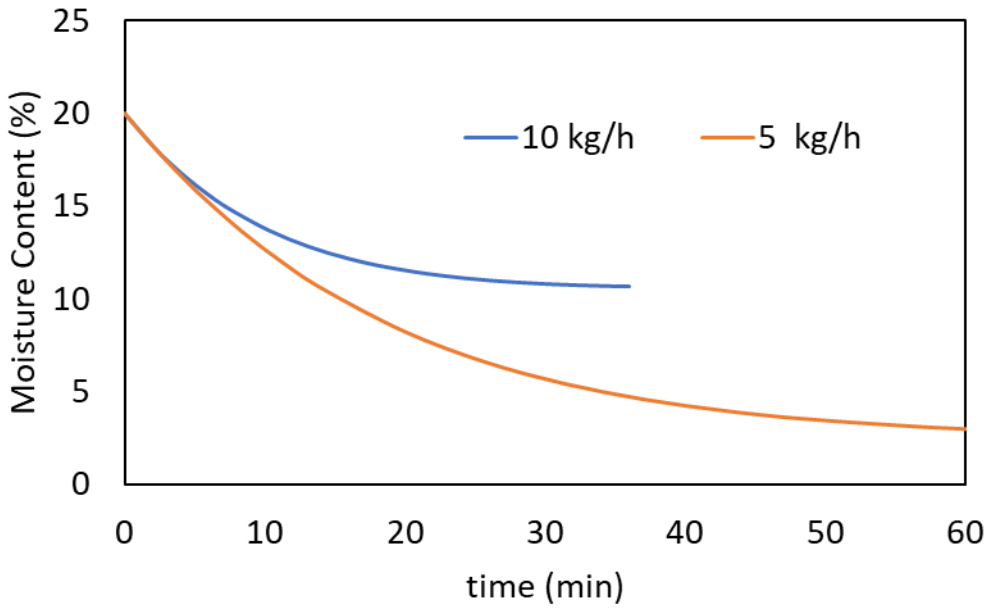

Figure 4-34: Effluent moisture content of GPCG-2 drying under different material flow rate (Air temperature 80°C, 4 kg initial loading, and 90 m^3/h air flow).

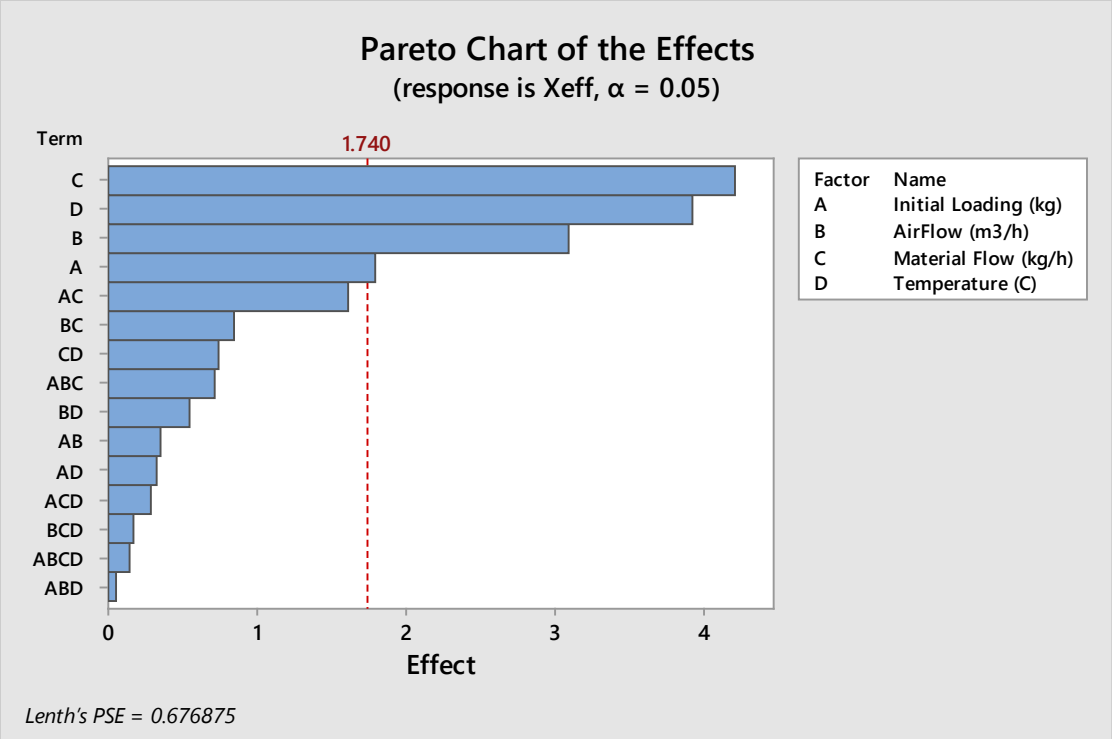

Figure 4-35: Pareto chart of the effects.

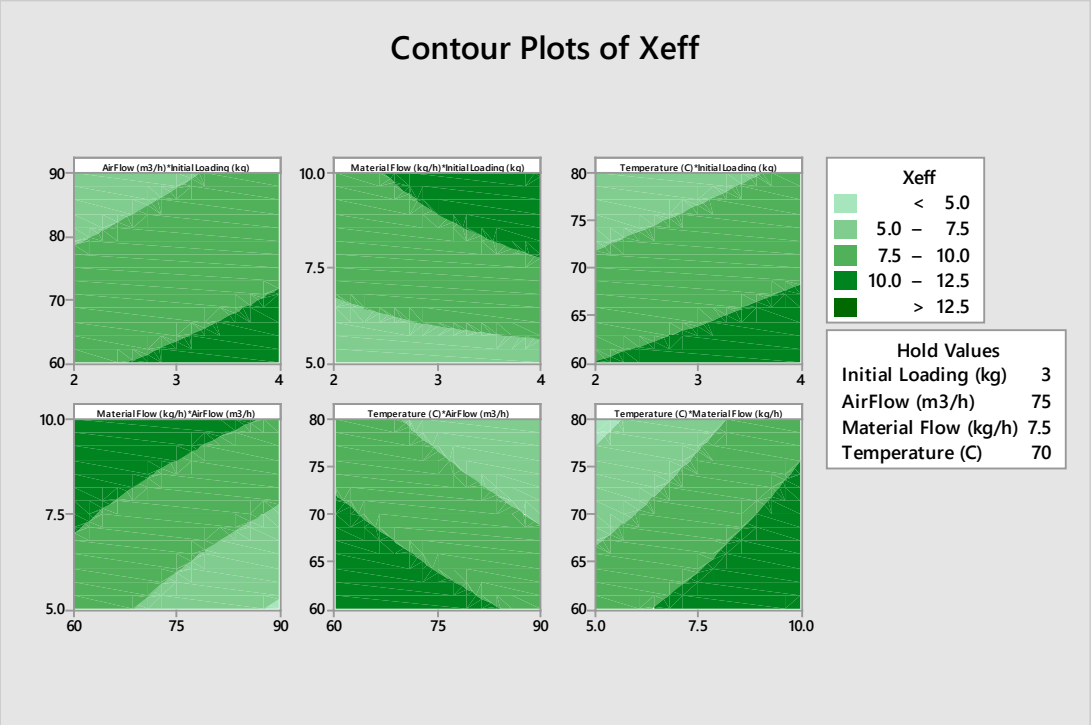

Figure 4-36: Contour plots of effluent moisture content.

4.6 Tables for Chapter 4

Table 4-1: Design of experiment

Experiment #	Initial Loading (kg)	Air Flow Rate (m^3/h)	Material Flow Rate (kg/h)
1	4	90	10
2	4	60	5
3	4	90	5
4	2	60	10
5	2	90	10
6	2	90	5
7	1	90	5
8	2	90	15

Table 4-2: RTD results

Experiment #	t_{space} (min)	t_m (min)	σ^2 (min^2)	s^3 (min^3)	Pe
1	24	13.62	101.80	1.36	2.14
2	48	28.34	426.70	1.19	2.29
3	48	23.52	268.50	0.742	2.70
4	12	10.68	66.89	1.05	1.87
5	12	10.53	66.57	1.39	1.77
6	24	16.53	116.90	1.03	3.31
7	12	13.13	41.33	0.804	7.18
8	8	7.04	20.30	0.835	3.55

Table 4-3: Results of TIS model fitting

Experiment #	n	t_m(min)	t_p(min)	R^2
1	1.23	8.39	1.93	0.994
2	1.14	33.15	1.94	0.935
3	1.25	23.08	1.53	0.952
4	1.15	10.27	0.99	0.987
5	1.16	9.32	1.60	0.960
6	1.89	15.21	0.59	0.991
7	1.40	8.91	4.89	0.987
8	1.48	6.48	0.95	0.997

Table 4-4: Simulation of the drying curve in GPCG-2 under various operating conditions.

Simulation	Loading (kg)	Air Flow (m3/h)	Material Flow (kg/h)	Temperature (C)	Xeff
1	2	60	5	60	10.44
2	4	60	10	80	12.00
3	4	90	10	80	10.63
4	4	60	5	80	7.02
5	2	90	5	80	2.15
6	2	90	10	80	5.35
7	2	60	10	80	9.25
8	2	90	5	60	7.50
9	4	90	10	60	13.40
10	2	90	10	60	9.74
11	2	60	10	60	12.47
12	2	60	5	80	6.35
13	4	90	5	60	7.35
14	4	60	10	60	14.40
15	4	60	5	60	10.84
16	4	90	5	80	1.92

Chapter 5 Conclusion and Future Work

5.1 Conclusion

This dissertation aims to push forward fluidized bed drying technology application in pharmaceutical manufacturing of oral solids and to contribute to the progression of the development of continuous manufacturing. To establish a model for a continuous fluidized bed system, one must obtain the reaction kinetics as well as the hydrodynamics of the material in the system. In the context of the fluidized bed drying process, the reaction kinetics are a function of several operating parameters for a given material. Therefore, this work starts with studying the effects of operating conditions on the drying time in two batch fluidized bed systems in Chapter 2.

In Chapter 2, the drying of a porous pharmaceutical excipient, DCPA, was investigated in two sizes of batch fluidized beds. It was found that DCPA powders experienced zero-order kinetics during drying in the fluidized bed. By carrying out a Pareto analysis, it was found that the initial moisture content, the inlet heating air temperature, the inlet heating air mass flow rate and the material loading in the dryer have independent effects on the required drying time. The interaction effects of the above operating parameters are negligible.

Comparing the drying kinetics of DCPA in an oven dryer and the fluidized bed dryer, it was discovered that both drying process consists of unhindered drying period and hindered drying period. The oven drying had much larger effective diffusivity than the fluidized bed. This could be due to that heat conduction between particles and air in a fluidized bed is smaller than the heat conduction between particles and aluminum weighing plate in an oven dryer. The drying process in a fluidized bed dryer is therefore limited by the rate of heat supply from the gas phase.

Another important finding from Chapter 2 was that the particle size does not affect the drying rate significantly in a fluidized bed dryer. As most of the single particle drying models suggest that smaller particles should dry faster as they have larger surface-area-to-volume ratio than larger particles, it was contradicting to the observation from Figure 2-23 where no significant difference in drying rate was found. The drying process in a fluidized bed dryer is limited by the heat transfer, and the area of heat transfer in a fluidized bed is slightly above the air distributor. Therefore, the drying rate is similar for different size of particles because the heat transfer for the entire particle bed only depends on the air distributor size.

The energy efficiency of the drying in the fluidized bed was examined based a heat and mass balance at the surface of the particles. An efficiency coefficient, h/k, was defined. The results showed that h/k reached highest at the unhindered stage of drying. It was not a surprise that h/k was higher when the material has more initial moisture content because a longer unhindered stage of drying was achieved. It was also found that the energy efficiency was higher when lower inlet air temperatures and higher inlet heating air mass flow rates were adopted.

In the pharmaceutical industry, the unit operation is usually carried out in small lab scale equipment during the process development stage. Therefore, being able to scale from lab scale or pilot scale fluidized bed dryer to industrial scale is crucial. In addition, validating the process in larger scales requires a tremendous amount of material. Since the synthetic APIs are usually expensive, it becomes important to minimize the runs of trials in larger scales.

Chapter 3 sought to address the aforementioned issue. A scaling method was developed based on a mass balance between the solid phase and gas phase to predict the drying curve under different operating conditions based on the existing experimental data from one set of operating conditions. A dimensionless factor, Z, was defined. All of the four operating parameters from Chapter 2 were examined. The initial moisture content was found not to affect the drying rate and was therefore excluded from the scaling model. The scaling model performed well in predicting drying curves for different inlet heating air temperature and inlet heating air mass flow rate. For MiniGlatt, since the lower part of the body is conical and the upper part of the body is cylindrical, the model did not give an accurate prediction for a high loading (upper body region) from a low loading (lower body region) case. Nevertheless, the model still worked for predicting low loadings from a low loading case or predicting high loadings from a high loading case. It was worth mentioning that the area of the air distributor should be used during the calculation in the scaling equation as Kemp [94] stated that the majority of drying occurs in the space a few inches above the air distributor. The scaling model also aimed to predict the drying curve for different scales of fluidized bed dryer with similar geometric design. Overall, the scaling model showed good agreement up until Z reached a value of 3.

Based on the conclusions from the batch fluidized bed system, we wanted to utilize the knowledge of drying kinetics to develop a model for a continuous fluidized bed system. Chapter 4 started with studying the hydrodynamic behavior of a specific material in the continuous fluidized bed system. The effect of several operating parameters on the residence time distribution was investigated. The continuous fluidized bed showed the behavior of two CSTRs in series no matter how the operating condition changed.

Increasing the loading (mass holdup) will reduce the peak height and increase the peak width of the RTD curve. Increasing the mass flow of the material will significantly reduce residence time. As a result, the peak of the RTD curve appeared earlier. In addition, the peak height increased and the peak width reduced. The changing of inlet air flow rate had negligible effects on the RTD as it was not enhancing or prohibiting materials from moving forward.

Both the drying kinetics and the hydrodynamics were achieved. Eventually, a mixing model was used to combine the two models to predict the drying curve of the effluent materials from the continuous fluidized bed dryer system. In Chapter 4, the segregation model and the maximum mixedness model were compared. The previous model assumes each particle dries at its own pace. The latter assumes all of the particles are well mixed and have the same drying rate. The results showed that the SM overestimated the number of particles that fell into the hindered drying stage and overpredicted the final moisture content in the effluent stream. The MMM gave an excellent prediction of the drying curve at the effluent.

5.2 Future Work

The work of the dissertation studied the drying of an excipient (DCPA) in three sizes of batch and continuous fluidized bed dryers. Further work is needed to validate the conclusions for different materials. DCPA is a porous material with a spherical shape. The powder has relatively low density and flows extremely well. In the pharmaceutical industry, ingredients are usually mixed and granulated before drying, which results in non-spherical, solid and high-density granules. The drying curve of the DCPA powder appeared to have an unhindered stage that dominated its drying behavior due to its small internal resistance of mass transfer. Meanwhile, some studies [145-148] have reported materials where the hindered stage cannot be neglected. During the hindered stage, the effect of operating parameters on drying time would be different from the unhindered stage because the drying process switches from heat transfer limitation to mass transfer limitation. For granulated materials, it is possible that the internal structure change will cause the material to dry at a hindered stage. Because the granulated particles consist of several components, the level of water uptake could varied within the granules. Current drying model assumed uniform moisture level within the material which may need to include another degree of freedom in the model if applying to the granulated materials.

For the scaling method, the current method has only been validated for three fluidized bed dryers – miniGlatt, GPCG-1, and GPCG-2 for DCPA. The geometry of the three fluidized beds are similar in terms of all of them had a conical shape. The circulation of the particles during the fluidization was similar. For scaling up to commercial size, the wall effect will be less significant, and the bed expansion will be less [132]. Further work is needed for examining the scaling method to different geometry designs and larger scales.

The continuous fluidized bed dryer model developed in this thesis was based on Glatt GPCG-2 which uses a static baffle in a conical chamber to realize continuous processing. Other designs such as a rotating baffle or rectangle chamber in series design might result in a different mechanism of particle movement and mixing. Further study is needed to validate the model for other continuous fluidized bed systems. Furthermore, the current study was based on a feeder – fluidized bed system which only investigates the fluidized bed. However, in a continuous process, the fluidized bed is connected to a wet granulation unit and therefore cannot be studied as a stand-alone unit. For process development purposes, the design space of the fluidized bed dryer and the wet granulation unit needs to be aligned. This can be realized by establishing a process flowsheet model based on experimental research from both units.

Further work could also be done to implement other chemical or physical transfer models to the drying such as fluidized bed coating, impregnation, granulation and crystallization of amorphous components. For example, the fluidized bed granulation process consists of several stages – spraying, wetting, consolidating, layer-wise coating and drying [149]. It is possible to model the previous processes and implement them into our model.

References

[1] S. Meziane, Drying kinetics of olive pomace in a fluidized bed dryer, Energy Conversion and Management, 52 (2011) 1644-1649.
[2] M.S.H. Sarker, M.N. Ibrahim, N.A. Aziz, M.S. Punan, Drying Kinetics, Energy Consumption, and Quality of Paddy (MAR-219) during Drying by the Industrial Inclined Bed Dryer with or without the Fluidized Bed Dryer, Drying Technology, 31 (2013) 286-294.
[3] M. Zielinska, M. Markowski, Drying Behavior of Carrots Dried in a Spout–Fluidized Bed Dryer, Drying Technology, 25 (2007) 261-270.
[4] R.B. Keey, Introduction to industrial drying operations, Pergamon, Oxford ; New York, 1978.
[5] A. Mujumdar, Drying, Kirk‐Othmer Encyclopedia of Chemical Technology2011.
[6] C.E. Sloan, Drying systems and equipment, Chemical Engineering, 19 (1967) 167.
[7] P.Y. McCormick, Chemical Engineering Handbook, 5th ed., McGraw-Hill, New York, 1973.
[8] R.B. Keey, Drying: Principles and Practice, Pergamon Press, Oxford, 1972.
[9] A.S. Mujumdar, Handbook of Industrial Drying, 3rd ed., CRC Press Boca Raton, 2006.
[10] G. Musielak, D. Mierzwa, J. Kroehnke, Food drying enhancement by ultrasound – A review, Trends in Food Science & Technology, 56 (2016) 126-141.
[11] X.D. Chen, S.X.Q. Lin, Air drying of milk droplet under constant and time-dependent conditions, AIChE Journal, 51 (2005) 1790-1799.
[12] S. VijayaVenkataRaman, S. Iniyan, R. Goic, A review of solar drying technologies, Renewable and Sustainable Energy Reviews, 16 (2012) 2652-2670.
[13] P. Čermák, M. Trcala, Influence of uncertainty in diffusion coefficients on moisture field during wood drying, International Journal of Heat and Mass Transfer, 55 (2012) 7709-7717.
[14] V. Zadin, H. Kasemägi, V. Valdna, S. Vigonski, M. Veske, A. Aabloo, Application of multiphysics and multiscale simulations to optimize industrial wood drying kilns, Applied Mathematics and Computation, 267 (2015) 465-475.
[15] S.L. Truscott, I.W. Turner, A heterogeneous three-dimensional computational model for wood drying, Applied Mathematical Modelling, 29 (2005) 381-410.
[16] M. Hasan, T.A.G. Langrish, Numerical Simulation of a Solar Kiln Design for Drying Timber with Different Geographical and Climatic Conditions in Australia, Drying Technology, 32 (2014) 1632-1639.
[17] S.N. Moejes, A.J.B. van Boxtel, Energy saving potential of emerging technologies in milk powder production, Trends in Food Science & Technology, 60 (2017) 31-42.
[18] E. Sánchez, J. García-Ten, V. Sanz, A. Moreno, Porcelain tile: Almost 30 years of steady scientific-technological evolution, Ceramics International, 36 (2010) 831-845.
[19] A. Mezquita, E. Monfort, S. Ferrer, D. Gabaldón-Estevan, How to reduce energy and water consumption in the preparation of raw materials for ceramic tile manufacturing: Dry versus wet route, Journal of Cleaner Production, 168 (2017) 1566-1570.
[20] A. Lekhal, K.P. Girard, M.A. Brown, S. Kiang, B.J. Glasser, J.G. Khinast, Impact of agitated drying on crystal morphology: KCl–water system, Powder Technology, 132 (2003) 119-130.
[21] M.J. Maltesen, M. van de Weert, Drying methods for protein pharmaceuticals, Drug Discovery Today: Technologies, 5 (2008) e81-e88.
[22] N. Jovanović, A. Bouchard, G.W. Hofland, G.-J. Witkamp, D.J.A. Crommelin, W. Jiskoot, Stabilization of Proteins in Dry Powder Formulations Using Supercritical Fluid Technology, Pharmaceutical Research, 21 (2004) 1955-1969.
[23] N. Jovanović, A. Bouchard, M. Sutter, M. Van Speybroeck, G.W. Hofland, G.-J. Witkamp, D.J.A. Crommelin, W. Jiskoot, Stable sugar-based protein formulations by supercritical fluid drying, International Journal of Pharmaceutics, 346 (2008) 102-108.

[24] N. Jovanović, A. Bouchard, G.W. Hofland, G.-J. Witkamp, D.J.A. Crommelin, W. Jiskoot, Stabilization of IgG by supercritical fluid drying: Optimization of formulation and process parameters, European Journal of Pharmaceutics and Biopharmaceutics, 68 (2008) 183-190.
[25] S.P. Cape, J.A. Villa, E.T.S. Huang, T.-H. Yang, J.F. Carpenter, R.E. Sievers, Preparation of Active Proteins, Vaccines and Pharmaceuticals as Fine Powders using Supercritical or Near-Critical Fluids, Pharmaceutical Research, 25 (2008) 1967-1990.
[26] I.C. Kemp, Drying of pharmaceuticals in theory and practice, Drying Technology, 35 (2017) 918-924.
[27] A. Lekhal, K.P. Girard, M.A. Brown, S. Kiang, J.G. Khinast, B.J. Glasser, The effect of agitated drying on the morphology of l-threonine (needle-like) crystals, International Journal of Pharmaceutics, 270 (2004) 263-277.
[28] S. Airaksinen, M. Karjalainen, A. Shevchenko, S. Westermarck, E. Leppänen, J. Rantanen, J. Yliruusi, Role of water in the physical stability of solid dosage formulations, Journal of Pharmaceutical Sciences, 94 (2005) 2147-2165.
[29] A.H. Gerhardt, Moisture effects on solid dosage forms formulation, processing and stability, Journal of GXP Compliance, 13 (2009) 58-66.
[30] G.S. Pande, R.F. Shangraw, Characterization of β-cyclodextrin for direct compression tableting: II. The role of moisture in the compactibility of β-cyclodextrin, International Journal of Pharmaceutics, 124 (1995) 231-239.
[31] J.J. Fitzpatrick, S.A. Barringer, T. Iqbal, Flow property measurement of food powders and sensitivity of Jenike's hopper design methodology to the measured values, Journal of Food Engineering, 61 (2004) 399-405.
[32] E. Emery, J. Oliver, T. Pugsley, J. Sharma, J. Zhou, Flowability of moist pharmaceutical powders, Powder Technology, 189 (2009) 409-415.
[33] K. Kogermann, J. Aaltonen, C.J. Strachan, K. Pöllänen, J. Heinämäki, J. Yliruusi, J. Rantanen, Establishing quantitative in-line analysis of multiple solid-state transformations during dehydration, Journal of Pharmaceutical Sciences, 97 (2008) 4983-4999.
[34] N. Heigl, D.M. Koller, B.J. Glasser, F.J. Muzzio, J.G. Khinast, Quantitative on-line vs. off-line NIR analysis of fluidized bed drying with consideration of the spectral background, European Journal of Pharmaceutics and Biopharmaceutics, 85 (2013) 1064-1074.
[35] Y. Tatemoto, R. Mizukoshi, W. Ehara, E. Ishikawa, Drying characteristics of food materials injected with organic solvents in a fluidized bed of inert particles under reduced pressure, Journal of Food Engineering, 158 (2015) 80-85.
[36] G. Srinivas, Y. Pydi Setty, Drying behavior of uniform and binary mixture of solids in a batch fluidized bed dryer, Powder Technology, 241 (2013) 181-187.
[37] J. Rantanen, J. Khinast, The Future of Pharmaceutical Manufacturing Sciences, Journal of Pharmaceutical Sciences, 104 (2015) 3612-3638.
[38] S. Palzer, Drying of wet agglomerates in a continuous fluid bed: Influence of residence time, air temperature and air-flow rate on the drying kinetics and the amount of oversize particles, Chemical Engineering Science, 62 (2007) 463-470.
[39] S. Hematian, F. Hormozi, Drying kinetics of coated sodium percarbonate particles in a conical fluidized bed dryer, Powder Technology, 269 (2015) 30-37.
[40] H.D. Emrah Özahi, Drying performance analysis of a batch type fluidized bed drying process for corn and unshelled pistachio nut regarding to energetic and exergetic efficiencies, Measurment, 60 (2015) 85-96.
[41] M. Türker, A. Kanarya, U. Yüzgeç, H. Kapucu, Z. Şenalp, Drying of baker's yeast in batch fluidized bed, Chemical Engineering and Processing: Process Intensification, 45 (2006) 1019-1028.

[42] M.S.H. Sarker, M.N. Ibrahim, N. Abdul Aziz, M.S. Punan, Energy and exergy analysis of industrial fluidized bed drying of paddy, Energy, 84 (2015) 131-138.
[43] W.R. Wan Daud, Fluidized Bed Dryers — Recent Advances, Advanced Powder Technology, 19 (2008) 403-418.
[44] M.R. Assari, H. Basirat Tabrizi, E. Najafpour, Energy and exergy analysis of fluidized bed dryer based on two-fluid modeling, International Journal of Thermal Sciences, 64 (2013) 213-219.
[45] R. Ramachandran, J.M.H. Poon, C.F.W. Sanders, T. Glaser, C.D. Immanuel, F.J. Doyle Iii, J.D. Litster, F. Stepanek, F.-Y. Wang, I.T. Cameron, Experimental studies on distributions of granule size, binder content and porosity in batch drum granulation: Inferences on process modelling requirements and process sensitivities, Powder Technology, 188 (2008) 89-101.
[46] L. Briens, M. Bojarra, Monitoring fluidized bed drying of pharmaceutical granules, AAPS PharmSciTech, 11 (2010) 1612-1618.
[47] Á. Hegedűs, K. Pintye-Hódi, Comparison of the effects of different drying techniques on properties of granules and tablets made on a production scale, International Journal of Pharmaceutics, 330 (2007) 99-104.
[48] A. Ebrahimi, M. Saffari, T. Langrish, Developing a new production process for high-porosity lactose particles with high degrees of crystallinity, Powder Technology, 272 (2015) 45-53.
[49] N. Yazdanpanah, T.A.G. Langrish, Egg-shell like structure in dried milk powders, Food Research International, 44 (2011) 39-45.
[50] L. Briens, M. Bojarra, Monitoring fluidized bed drying of pharmaceutical granules, AAPS PharmSciTech, 11 (2010) 1612-1618.
[51] D. Geldart, Types of gas fluidization, Powder Technology, 7 (1973) 285-292.
[52] Y. Chen, J. Yang, R.N. Dave, R. Pfeffer, Fluidization of coated group C powders, AIChE Journal, 54 (2008) 104-121.
[53] M. Mezhericher, A. Levy, I. Borde, Modelling of particle breakage during drying, Chemical Engineering and Processing: Process Intensification, 47 (2008) 1404-1411.
[54] M. Mezhericher, A. Levy, I. Borde, Theoretical Drying Model of Single Droplets Containing Insoluble or Dissolved Solids, Drying Technology, 25 (2007) 1025-1032.
[55] A. Lekhal, B.J. Glasser, J.G. Khinast, Impact of drying on the catalyst profile in supported impregnation catalysts, Chemical Engineering Science, 56 (2001) 4473-4487.
[56] X. Liu, J.G. Khinast, B.J. Glasser, A parametric investigation of impregnation and drying of supported catalysts, Chemical Engineering Science, 63 (2008) 4517-4530.
[57] T.A.G. Langrish, T.K. Kockel, The assessment of a characteristic drying curve for milk powder for use in computational fluid dynamics modelling, Chemical Engineering Journal, 84 (2001) 69-74.
[58] A.S.M. Chung Lim Law, Fluidized Bed Dryers, in: A.S. Mujumdar (Ed.) Handbook of industrial drying, CRC Press, Boca Raton, Florida, 2015, pp. 165.
[59] A.H. Zahed, N. Epstein, Batch and continuous spouted bed drying of cereal grains: The thermal equilibrium model, The Canadian Journal of Chemical Engineering, 70 (1992) 945-953.
[60] C. Martinez-Vera, M. Vizearra-Mendoza, O. Galin-Domingo, R. Ruiz-Martinez, Experimental Validation of a Mathematical Model for the Batch Drying of Corn Grains, Drying Technology, 13 (1995) 333-350.
[61] D. Chen, Y. Zheng, X. Zhu, Determination of effective moisture diffusivity and drying kinetics for poplar sawdust by thermogravimetric analysis under isothermal condition, Bioresource Technology, 107 (2012) 451-455.

[62] M. Taghavivand, K. Choi, L. Zhang, Investigation on drying kinetics and tribocharging behaviour of pharmaceutical granules in a fluidized bed dryer, Powder Technology, 316 (2017) 171-180.
[63] S.T.F.C. Mortier, T. De Beer, K.V. Gernaey, J.P. Remon, C. Vervaet, I. Nopens, Mechanistic modelling of fluidized bed drying processes of wet porous granules: A review, European Journal of Pharmaceutics and Biopharmaceutics, 79 (2011) 205-225.
[64] D.-H. Lee, S.-D. Kim, Mathematical Model for Batch Drying in an Inert Medium Fluidized Bed, Chemical Engineering & Technology, 22 (1999) 443-450.
[65] C.D. Immanuel, F.J. Doyle Iii, Solution technique for a multi-dimensional population balance model describing granulation processes, Powder Technology, 156 (2005) 213-225.
[66] M.J. Hounslow, J.M.K. Pearson, T. Instone, Tracer studies of high-shear granulation: II. Population balance modeling, AIChE Journal, 47 (2001) 1984-1999.
[67] J.M.K. Pearson, M.J. Hounslow, T. Instone, Tracer studies of high-shear granulation: I. Experimental results, AIChE Journal, 47 (2001) 1978-1983.
[68] M. Peglow, J. Kumar, S. Heinrich, G. Warnecke, E. Tsotsas, L. Mörl, B. Wolf, A generic population balance model for simultaneous agglomeration and drying in fluidized beds, Chemical Engineering Science, 62 (2007) 513-532.
[69] M. Peglow, U. Cunäus, E. Tsotsas, An analytical solution of population balance equations for continuous fluidized bed drying, Chemical Engineering Science, 66 (2011) 1916-1922.
[70] R. Bahu, Energy consumption in dryer design, Drying, 91 (1991) 553-557.
[71] E. Özahi, H. Demir, A model for the thermodynamic analysis in a batch type fluidized bed dryer, Energy, 59 (2013) 617-624.
[72] I.D. S. Syahrul, F. Hamdullahpur, Thermodynamic modeling of fluidized bed drying of moist particles, International Journal of Thermal Sciences, 42 (2003) 691-701.
[73] P. Zhao, Y. Zhao, Z. Luo, Z. Chen, C. Duan, S. Song, Effect of operating conditions on drying of Chinese lignite in a vibration fluidized bed, Fuel Processing Technology, 128 (2014) 257-264.
[74] A. Midilli, H. Kucuk, Z. Yapar, A new model for single-layer drying, Drying Technology, 20 (2002) 1503-1513.
[75] X. Liu, F.J. Muzzio, B.J. Glasser, J.G. Khinast, Fluidized bed drying of pharmaceutical materials: Moisture measurement and effects of particle size, American Pharmaceutical Review, 16 (2013).
[76] H. Altzibar, G. Lopez, S. Alvarez, M.J.S. José, A. Barona, M. Olazar, A Draft-Tube Conical Spouted Bed for Drying Fine Particles, Drying Technology, 26 (2008) 308-314.
[77] R.v.O. Michael Wormsbecker, John Nijenhuis, Helen Tanfara, Todd Pugsley, The influence of vessel geometry on fluidized bed dryer hydrodynamics, Powder Technology, 194 (2009) 115-125.
[78] P. Eliaers, J. De Wilde, Drying of Biomass Particles: Experimental Study and Comparison of the Performance of a Conventional Fluidized Bed and a Rotating Fluidized Bed in a Static Geometry, Drying Technology, 31 (2013) 236-245.
[79] M.M. Nasr, M. Krumme, Y. Matsuda, B.L. Trout, C. Badman, S. Mascia, C.L. Cooney, K.D. Jensen, A. Florence, C. Johnston, K. Konstantinov, S.L. Lee, Regulatory perspectives on continuous pharmaceutical manufacturing: Moving from theory to practice, Journal of Pharmaceutical Sciences, (2017).
[80] F.X. McConville, Pilot Plants, Kirk‐Othmer Encyclopedia of Chemical Technology2005.
[81] J.H. de-Groot, Scaling up of gas-fluidized bed reactors, Proceedings of the International symposium on fluidization, Amsterdam : Netherlands University Press, Eindhoven, 1967.
[82] J.M. Matsen, Scale-up of fluidized bed processes: Principle and practice, Powder Technology, 88 (1996) 237-244.

[83] L.R. Glicksman, Scaling relationships for fluidized beds, Chemical Engineering Science, 39 (1984) 1373-1379.
[84] L.R. Glicksman, M. Hyre, K. Woloshun, Simplified scaling relationships for fluidized beds, Powder Technology, 77 (1993) 177-199.
[85] J.R. van Ommen, M. Teuling, J. Nijenhuis, B.G.M. van Wachem, Computational validation of the scaling rules for fluidized beds, Powder Technology, 163 (2006) 32-40.
[86] T.M. Knowlton, S.B.R. Karri, A. Issangya, Scale-up of fluidized-bed hydrodynamics, Powder Technology, 150 (2005) 72-77.
[87] B. Rambali, L. Baert, D.L. Massart, Scaling up of the fluidized bed granulation process, International Journal of Pharmaceutics, 252 (2003) 197-206.
[88] E.W. Conder, A.S. Cosbie, J. Gaertner, W. Hicks, S. Huggins, C.S. MacLeod, B. Remy, B.-S. Yang, J.D. Engstrom, D.J. Lamberto, C.D. Papageorgiou, The pharmaceutical drying unit operation: An industry perspective on advancing the science and development approach for scale-up and technology transfer, Organic Process Research & Development, 21 (2017) 420-429.
[89] A.M. Keech, R.B. Keey, Q.J. Zhang, T.A.G. Langrish, I.C. Kemp, H.S. Pasley, An experimental test of the concept of the characteristic drying curve using the thin-layer method, Drying Technology, 13 (1995) 1133-1152.
[90] T.A.G. Langrish, Characteristic drying curves for cellulosic fibres, Chemical Engineering Journal, 137 (2008) 677-680.
[91] T.A.G. Langrish, R.E. Bahu, D. Reay, Drying kinetics of particles from thin layer drying experiments, Chemical Engineering Research and Design, 69 (1991) 417-424.
[92] D. Reay, R. Allen, The effect of bed temperature on fluid bed batch drying curves, J. Separ. Proc. Technol, 3 (1982) 11-13.
[93] R.E. Bahu, Fluidised bed dryer scale-up, Drying Technology, 12 (1994) 329-339.
[94] I.C. Kemp, D.E. Oakley, Modelling of particulate drying in theory and practice, Drying Technology, 20 (2002) 1699-1750.
[95] J.S. Srai, C. Badman, M. Krumme, M. Futran, C. Johnston, Future Supply Chains Enabled by Continuous Processing-Opportunities and Challenges May 20-21, 2014 Continuous Manufacturing Symposium, Journal of Pharmaceutical Sciences, 104 (2015) 840-849.
[96] U.S.F.a.D. Administration, Paving the way for personalized medicine: FDA's role in a new era of medical product development, 2013.
[97] S.D. Schaber, D.I. Gerogiorgis, R. Ramachandran, J.M.B. Evans, P.I. Barton, B.L. Trout, Economic Analysis of Integrated Continuous and Batch Pharmaceutical Manufacturing: A Case Study, Industrial & Engineering Chemistry Research, 50 (2011) 10083-10092.
[98] P.D.J. M. C. Gohel, A review of co-processed directly compressible excipients, Journal of pharmacy and pharmaceutical sciences, 8 (2005) 76-93.
[99] B. Van Snick, J. Holman, V. Vanhoorne, A. Kumar, T. De Beer, J.P. Remon, C. Vervaet, Development of a continuous direct compression platform for low-dose drug products, International Journal of Pharmaceutics, 529 (2017) 329-346.
[100] S. Patel, A.M. Kaushal, A.K. Bansal, Compression physics in the formulation development of tablets, Critical Reviews in Therapeutic Drug Carrier Systems, 23 (2006) 1-65.
[101] H.A. Garekani, J.L. Ford, M.H. Rubinstein, A.R. Rajabi-Siahboomi, Formation and compression characteristics of prismatic polyhedral and thin plate-like crystals of paracetamol, International Journal of Pharmaceutics, 187 (1999) 77-89.
[102] A.P. Pawar, A.R. Paradkar, S.S. Kadam, K.R. Mahadik, Crystallo-co-agglomeration: A novel technique to obtain ibuprofen-paracetamol agglomerates, AAPS PharmSciTech, 5 (2004) 57-64.
[103] A. Adam, L. Schrimpl, P.C. Schmidt, Factors Influencing Capping and Cracking of Mefenamic Acid Tablets, Drug Development and Industrial Pharmacy, 26 (2000) 489-497.

[104] P. Di Martino, M. Scoppa, E. Joiris, G.F. Palmieri, C. Andres, Y. Pourcelot, S. Martelli, The spray drying of acetazolamide as method to modify crystal properties and to improve compression behaviour, International Journal of Pharmaceutics, 213 (2001) 209-221.
[105] M.C. Gohel, P.D. Jogani, Exploration of Melt Granulation Technique for the Development of Coprocessed Directly Compressible Adjuvant Containing Lactose and Microcrystalline Cellulose, Pharmaceutical Development and Technology, 8 (2003) 175-185.
[106] C. Pontier, M. Viana, E. Champion, D. Bernache-Assollant, D. Chulia, About the use of stoichiometric hydroxyapatite in compression – incidence of manufacturing process on compressibility, European Journal of Pharmaceutics and Biopharmaceutics, 51 (2001) 249-257.
[107] M. Bi, C.C. Sun, F. Alvarez, F. Alvarez-Nunez, The Manufacture of Low-Dose Oral Solid Dosage Form to Support Early Clinical Studies Using an Automated Micro-Filing System, AAPS PharmSciTech, 12 (2011) 88-95.
[108] S. Byrn, M. Futran, H. Thomas, E. Jayjock, N. Maron, R.F. Meyer, A.S. Myerson, M.P. Thien, B.L. Trout, Achieving Continuous Manufacturing for Final Dosage Formation: Challenges and How to Meet Them May 20–21 2014 Continuous Manufacturing Symposium, Journal of Pharmaceutical Sciences, 104 (2015) 792-802.
[109] R.M. Dhenge, R.S. Fyles, J.J. Cartwright, D.G. Doughty, M.J. Hounslow, A.D. Salman, Twin screw wet granulation: Granule properties, Chemical Engineering Journal, 164 (2010) 322-329.
[110] M.F. Saleh, R.M. Dhenge, J.J. Cartwright, M.J. Hounslow, A.D. Salman, Twin screw wet granulation: Binder delivery, International Journal of Pharmaceutics, 487 (2015) 124-134.
[111] C. Vervaet, J.P. Remon, Continuous granulation in the pharmaceutical industry, Chemical Engineering Science, 60 (2005) 3949-3957.
[112] M. Fonteyne, J. Vercruysse, D.C. Díaz, D. Gildemyn, C. Vervaet, J.P. Remon, T.D. Beer, Real-time assessment of critical quality attributes of a continuous granulation process, Pharmaceutical Development and Technology, 18 (2013) 85-97.
[113] W. Meng, L. Kotamarthy, S. Panikar, M. Sen, S. Pradhan, M. Marc, J.D. Litster, F.J. Muzzio, R. Ramachandran, Statistical analysis and comparison of a continuous high shear granulator with a twin screw granulator: Effect of process parameters on critical granule attributes and granulation mechanisms, International Journal of Pharmaceutics, 513 (2016) 357-375.
[114] U.S.F.a.D. Administration, Guidance for Industry PAT - A Framework for Innovative Pharmaceutical Development, Manufacturing, and Quality Assurance, in: U.S.D.o.H.a.H.S.F.a.D. Administration (Ed.)http://www.gmp-compliance.org/guidemgr/files/PAT-FDA-6419FNL.PDF, 2004.
[115] K. Pramod, M. Tahir, N. Charoo, S. Ansari, J. Ali, Pharmaceutical product development: A quality by design approach, International Journal of Pharmaceutical Investigation, 6 (2016) 129-138.
[116] F. De Leersnyder, V. Vanhoorne, H. Bekaert, J. Vercruysse, M. Ghijs, N. Bostijn, M. Verstraeten, P. Cappuyns, I. Van Assche, Y. Vander Heyden, E. Ziemons, J.P. Remon, I. Nopens, C. Vervaet, T. De Beer, Breakage and drying behaviour of granules in a continuous fluid bed dryer: Influence of process parameters and wet granule transfer, European Journal of Pharmaceutical Sciences, 115 (2018) 223-232.
[117] H. Chen, X. Liu, C. Bishop, B.J. Glasser, Fluidized bed drying of a pharmaceutical powder: A parametric investigation of drying of dibasic calcium phosphate, Drying Technology, 35 (2016) 1602-1618.
[118] D.A. Reay, R.W.K., Predicting the Performance of a Continuous Well-mixed Fluid Bed Dryer from Batch Tests, in: J.C. (Ed.) Drying Symp., Drying Research Ltd., Birmingham, 1982, pp. 130-140.

[119] K.A.B. McKenzie, R.E., Material Model for Fluidised Bed Drying, in: A.S. Mujumdar, et a (Ed.) 7th Int. Drying Symp., Elsevier, Prague, Czechoslovakia, 1991.
[120] W. Engisch, F. Muzzio, Using Residence Time Distributions (RTDs) to Address the Traceability of Raw Materials in Continuous Pharmaceutical Manufacturing, Journal of Pharmaceutical Innovation, 11 (2016) 64-81.
[121] J.R. O'Callaghan, D.J. Menzies, P.H. Bailey, Digital simulation of agricultural drier performance, Journal of Agricultural Engineering Research, 16 (1971) 223-244.
[122] A. Ayensu, Dehydration of food crops using a solar dryer with convective heat flow, Solar Energy, 59 (1997) 121-126.
[123] Q. Liu, F.W. Bakker-Arkema, Stochastic Modelling of Grain Drying: Part 2. Model Development, Journal of Agricultural Engineering Research, 66 (1997) 275-280.
[124] G. Page, FACTORS INFLUENCING THE MAXIMUM RATES OF AIR DRYING SHELLED CORN IN THIN LAYERS, ProQuest Dissertations Publishing, 1949.
[125] Q. Zhang, J.B. Litchfield, AN OPTIMIZATION OF INTERMITTENT CORN DRYING IN A LABORATORY SCALE THIN LAYER DRYER, Drying Technology, 9 (1991) 383-395.
[126] M.S. Rahman, C.O. Perera, C. Thebaud, Desorption isotherm and heat pump drying kinetics of peas, Food Research International, 30 (1997) 485-491.
[127] E.K. Akpinar, Y. Bicer, C. Yildiz, Thin layer drying of red pepper, Journal of Food Engineering, 59 (2003) 99-104.
[128] L. R. Verma, R. A. Bucklin, J. B. Endan, F. T. Wratten, Effects of Drying Air Parameters on Rice Drying Models, Transactions of the ASAE, 28 (1985) 296-0301.
[129] D.C. Montgomery, Design and Analysis of Experiments, 8 ed., Wiley2012.
[130] Y.A. Çengel, and Michael A. Boles, Thermodynamics: An Engineering Approach. , 7th ed. ed., McGraw-Hill, Boston, 2011.
[131] H. Tanfara, T. Pugsley, C. Winters, EFFECT OF PARTICLE SIZE DISTRIBUTION ON LOCAL VOIDAGE IN A BENCH-SCALE CONICAL FLUIDIZED BED DRYER, Drying Technology, 20 (2002) 1273.
[132] M. Rüdisüli, T.J. Schildhauer, S.M.A. Biollaz, J.R. van Ommen, Scale-up of bubbling fluidized bed reactors — A review, Powder Technology, 217 (2012) 21-38.
[133] P. Bareschino, A. Marzocchella, P. Salatino, Fluidised bed drying of powdered materials: Effects of operating conditions, Powder Technology, 308 (2017) 158-164.
[134] K.R. Morris, U.J. Griesser, C.J. Eckhardt, J.G. Stowell, Theoretical approaches to physical transformations of active pharmaceutical ingredients during manufacturing processes, Advanced Drug Delivery Reviews, 48 (2001) 91-114.
[135] G.G.Z. Zhang, D. Law, E.A. Schmitt, Y. Qiu, Phase transformation considerations during process development and manufacture of solid oral dosage forms, Advanced Drug Delivery Reviews, 56 (2004) 371-390.
[136] S.H. Cypes, R.M. Wenslow, S.M. Thomas, A.M. Chen, J.G. Dorwart, J.R. Corte, M. Kaba, Drying an organic monohydrate: Crystal form instabilities and a factory-scale drying scheme to ensure monohydrate preservation, Organic Process Research & Development, 8 (2004) 576-582.
[137] C. Fyhr, I.C. Kemp, Mathematical modelling of batch and continuous well-mixed fluidised bed dryers, Chemical Engineering and Processing: Process Intensification, 38 (1999) 11-18.
[138] E.U. Schlünder, Drying of Porous Material During the Constant and the Falling Rate Period: A Critical Review of Existing Hypotheses, Drying Technology, 22 (2004) 1517-1532.
[139] H.G. Wang, W.Q. Yang, P. Senior, R.S. Raghavan, S.R. Duncan, Investigation of batch fluidized-bed drying by mathematical modeling, CFD simulation and ECT measurement, AIChE Journal, 54 (2008) 427-444.

[140] Z. Hui Wang, G. Chen, Heat and mass transfer in batch fluidized-bed drying of porous particles, Chemical Engineering Science, 55 (2000) 1857-1869.
[141] H.S. Fogler, Distributions of Residence Times for Chemical Reactors, Essentials of Chemical Reaction Engineering, Prentice-Hall, the University of Michigan, 1986.
[142] H.N. Emady, M. Wittman, S. Koynov, W.G. Borghard, F.J. Muzzio, B.J. Glasser, A.M. Cuitino, A simple color concentration measurement technique for powders, Powder Technology, 286 (2015) 392-400.
[143] T.N. Zwietering, The degree of mixing in continuous flow systems, Chemical Engineering Science, 11 (1959) 1-15.
[144] T.N. Zwietering, A backmixing model describing micromixing in single-phase continuous-flow systems, Chemical Engineering Science, 39 (1984) 1765-1778.
[145] A. Aubin, R. Ansart, M. Hemati, T. Lasuye, M. Branly, Modeling and simulation of drying operations in PVC powder production line: Experimental and theoretical study of drying kinetics on particle scale, Powder Technology, 255 (2014) 120-133.
[146] R. Baini, T.A.G. Langrish, An assessment of the mechanisms for diffusion in the drying of bananas, Journal of Food Engineering, 85 (2008) 201-214.
[147] L.J. Pordage, T.A.G. Langrish, SIMULATION OF THE EFFECT OF AIR VELOCITY IN THE DRYING OF HARDWOOD TIMBER, Drying Technology, 17 (1999) 237-255.
[148] S. Soponronnarit, A. Pongtornkulpanich, S. Prachayawarakorn, Drying Characteristics of Corn in Fluidized Bed Dryer, Drying Technology, 15 (1997) 1603-1615.
[149] T. Hoffmann, C. Rieck, A. Bück, M. Peglow, E. Tsotsas, Influence of Granule Porosity during Fluidized Bed Spray Granulation, Procedia Engineering, 102 (2015) 458-467.